UNIVERSITA' DEGLI STUDI DI PADOVA

DIPARTIMENTO DI INGEGNERIA DELL'INFORMAZIONE

**CORSO DI LAUREA IN BIOINGEGNERIA**

Tesi di Laurea Magistrale

# SEGMENTATION OF NEEDLE ARTIFACTS IN REAL TIME 2D MR IMAGES

**19 Aprile 2011**

**RELATORE:**

**Prof. Alfredo Ruggeri**

**CORRELATORI:**

**Ing. Eva Rothgang**

**Prof. Joachim Hornegger**

**LAUREANDO:**

**Jessica Magaraggia**

**A. A. 2010/2011**

“ *There are in fact, two things: science and opinion;*
*the former begets knowledge, the latter ignorance*

HIPPOCRATES

“ *Man muss die Welt nicht verstehen,*
*man muss sich nur darin zurechtfinden*

ALBERT EINSTEIN

# Contents

# 1 Introduzione

Una delle nuove frontiere della chirurgia è rappresentata dagli interventi chirurgici minimamente invasivi condotti per via percutanea. La procedura prevede l'inserimento di un ago in corrispondenza della zona che rappresenta l'obiettivo dell'intervento, permettendo un trattamento locale del paziente senza bisogno di ricorrere ad operazioni chirurgiche a cielo aperto. Crescente è l'impiego di metodologie di ablazione termica per via percutanea per il trattamento di formazioni neoplastiche. Tutte le fasi dell'intervento sono supportate da tecniche di imaging, dalla fase diagnostica al monitoraggio della terapia durante l'ablazione. L'efficacia del trattamento ablativo è strettamente legata al corretto posizionamento dell'ago all'interno della massa neoplastica. In particolare dunque, il monitoraggio tramite immagini consente al chirurgo di avere una maggiore consapevolezza della posizione dello strumento.

Il monitoraggio può essere svolto tramite Risonanza Magnetica (RM) in tempo reale. L'*imaging* multiplanare e l'elevata capacità di discriminazione dei tessuti sono solo alcune delle caratteristiche, che rendono l'impiego della risonanza magnetica preferibile rispetto ad altre tecniche di *imaging* come la Tomografia Computerizzata (TC). Inoltre, nè il paziente nè il chirurgo sono esposti a radiazioni. La risonanza magnetica è in grado di misurare i cambiamenti di temperatura nel corpo. Quest'ultima rappresenta una proprietà fondamentale in caso di interventi di ablazione termica in quanto consente il monitoraggio del *thermal damage* indotto. L'acquisizione di immagini lungo la direzione dell'ago incrementa la visibilità dello strumento. Il riallineamento dei piani di scansione deve essere continuamente garantito in modo da compensare i movimenti dell'ago nel corso del posizionamento. In caso di riallineamento effettuato manualmente da parte dell'operatore, numerosi tentativi possono essere necessari prima che il piano di scansione risulti correttamente allineato. Durante il tempo in cui l'ago non risulta visibile, il rischio di collisione e danneggiamento di importanti strutture anatomiche circostanti aumenta. In alcuni casi il chirurgo può essere costretto ad arrestarsi ed attendere un nuovo corretto piano di scansione. Se fosse possibile segmentare l'ago in almeno una delle *slice* impiegate per il monitoraggio, la sua posizione potrebbe essere sfruttata per un riallineamento automatico e in tempo reale dei rimanenti piani di scansione. Questo contribuirebbe a ridurre i tempi dell'intervento e ad aumentare l'accuratezza del posizionamento dello strumento.

L'obiettivo dello studio svolto durante il lavoro di tesi è quello di sviluppare algoritmi in grado di segmentare l'ago nelle immagini impiegate per il monitoraggio durante il suo inserimento, in maniera automatica e in tempo reale. La determinazione della posizione dello strumento consentirebbe non solo il riallineamento automatico dei piani di scansione, ma contribuirebbe anche a fornire al chirurgo feedback riguardo la posizione corrente dell'ago [Dis]. Il lavoro di tesi è stato svolto presso il Pattern Recognition Lab presso la Friedrich-Alexander University of Erlangen-Nürnberg, Germania, in stretta collaborazione con il progetto di ricerca

di Eva Rothgang[1]. Gli algoritmi sviluppati mirano ad essere integrati nel *treatment workflow* proposto da Rothgang et al. [RDW+11]. Tale *workflow* prevede l'impiego della risonanza magnetica nel monitoraggio di tutte le fasi dell'intervento, dalla pianificazione al trattamento.

Durante il lavoro di tesi è stata compiuta anche un'analisi inerente l'aspetto caratteristico assunto dall'ago chirurgico in immagini di risonanza magnetica. Lo strumento, che deve essere compatibile per la risonanza magnetica, è responsabile della produzione di un *signal void* all'interno dell'immagine, in corrispondenza della sua posizione. Ciò significa che l'ago può essere identificato nelle immagini come una regione a bassa intensità di segnale e di estensione maggiore rispetto alle effettive dimensioni dello strumento a cui ci si riferisce con il termine *needle artifact*. Le tecniche di monitoraggio sono classificate in tre categorie ossia *active*, *semi-active* e *passive* [FMBM07] a seconda della quantità di strumentazione che deve essere impiegata per garantire l'identificazione della posizione.

Per il presente lavoro di tesi è stato adottato un approccio di tipo passivo. Le informazioni raccolte durante lo studio inerente il *signal void* prodotto dallo strumento sono state incorporate come informazioni a priori nell'implementazione degli algoritmi. Forte enfasi è stata posta nell'impiego dell'informazione a priori riguardante la traiettoria di inserimento pianificata.

## Sommario

Il Capitolo 3 offre un'introduzione ai principi base della risonanza magnetica, descrivendo la generazione del segnale e la sua codifica.

Il tema inerente l'impiego di interventi chirurgici minimamente invasivi condotti per via percutanea viene affrontato nel Capitolo 4. Nel corso del capitolo particolare attenzione viene posta sui vantaggi derivanti dal monitoraggio tramite risonanza magnetica. L'ultimo paragrafo fornisce una descrizione dei trattamenti eseguiti tramite ablazione con radiofrequenza e crio-ablazione.

Lo studio compiuto riguardante il caratteristico artefatto prodotto dall'ago chirurgico viene presentato nel Capitolo 5. Una breve sezione è dedicata alla descrizione dei principi fisici alla base della suscettibilità magnetica. Il capitolo prosegue passando in rassegna i vari fattori che possono influenzare l'aspetto dell'artefatto e presentando alcune delle tecniche presenti in letteratura per il monitoraggio della posizione dello strumento.

Un'analisi dei vantaggi derivanti dalla localizzazione automatica dello strumento

[1]Center for Applied Medical Imaging, Siemens Corporate Research, Baltimore (MD), USA.

durante il suo posizionamento viene presentata nel Capitolo 6. Il capitolo mira ad illustrare le motivazioni che sono alla base del lavoro di tesi. L'analisi viene svolta in particolare in relazione al framework (l'Interactive Front End, IFE [LKZ+05]) su cui si basa la realizzazione del treatment workflow in cui gli algoritmi sviluppati mirano ad essere integrati. Una breve sezione è dedicata alla descrizione dell'ambiente di sviluppo utilizzato: l'eXtensibile Imaging Platform, XIP. L'ultima sezione del capitolo è dedicata alla sequenza di eccitazione utilizzata per il monitoraggio nel corso della fase di posizionamento.

Dettagli relativi all'implementazione dei due algoritmi sviluppati vengono forniti nel Capitolo 7 con riferimento ai moduli sviluppati in C++ e utilizzati per estendere le funzionalità dell'ambiente XIP standard. Il primo degli algoritmi si basa sulla trasformata di Hough. Il secondo presenta un approccio più euristico e sfrutta le caratteristiche del più piccolo autovalore e algoritmi di *edge linking*. Entrambi gli algoritmi mirano alla determinazione dell'asse centrale dello strumento in modo da fornire indicazioni di offset in termini di orientazione e traslazione che possano essere utilizzate come linea guida dal chirurgo durante l'inserimento dell'ago e impiegati per il riallineamento automatico e in tempo reale dei piani di scansione delle immagini. Nei capitoli 8 e 9 viene condotta un'analisi critica dei risultati ottenuti durante la fase di test degli algoritmi.

# 2 Introduction

Percutaneous minimally invasive procedures represent a new frontier in surgical intervention. During the procedure a needle is used for percutaneous access to the region to be treated without need for an open surgery, drastically reducing the invasiveness. Remarkable is the increasing use of percutaneous thermal ablation to treat neoplastic formation. The effectiveness of such procedures is highly dependent on the correct placement of the needle inside the region to be treated. Imaging monitoring provides the physician with the possibility to inspect the location of the device.

The procedure can be performed under real time Magnetic Resonance Imaging guidance (MRI). In comparison to other imaging modalities, such as Computed Tomography (CT), magnetic resonance imaging is often preferred due to its multiplanar image capabilities and high soft tissue contrast. Moreover, neither the physician nor the patient are exposed to radiation. In addition, magnetic resonance imaging offers the possibility to measure temperature changes over the time. The latter represents a key advantage in thermal ablation treatment, since it allows to monitor the thermal damage. Slice acquisitions along the needle direction enhance the visibility of the device. A correct scan alignment needs to be continuously guaranteed and can require several updates during the insertion, in order to account for movements of the needle. However, alignment performed manually by the operator can be challenging and several trials may be required before a new correct scan plane is defined. When the needle is not visible the risk of injury of important surrounding structure increases and the physician is forced to stop until the scan plane is correctly realigned. If the needle could be automatically detected in at least one of the images acquired during the monitoring, automatic slice realignment could be performed on the fly. It is anticipated that automatic slice realignment would contribute to speed up the procedure and would increase the accuracy of the device positioning.

The goal of this work is to develop algorithms for automatic needle detection in real time MR images. The detection could allow not only automation of the slice realignment but also provide feedback to the physician concerning the current position of the device [Dis]. The present work was developed at the Pattern Recognition Lab at the Friedrich-Alexander University of Erlangen-Nürnberg, Germany, in close cooperation with the research project of Eva Rothgang[2]. The algorithms developed aim to be integrated into the treatment workflow as proposed by Rothgang et al. [RDW+11], that provides magnetic resonance imaging guidance through all the steps of the procedure.

[2]Center for Applied Medical Imaging, Siemens Corporate Research, Baltimore (MD), USA.

The appearance of the needle in magnetic resonance images is also investigated. The device, that needs to be MR-compatible, produces a characteristic susceptibility artifact and is responsible for a signal void in the MR images acquired. The management of the needle artifact can be addressed in an *active*, a *semi-active* or a *passive* approach [FMBM07], depending on the amount of further instrumentation employed in order to track the position of the needle.

In this work a passive approach is adopted. The information collected concerning the needle appearance is incorporated as prior in the algorithm implementation. In addition, strong emphasis is put on exploiting prior information concerning the insertion trajectory.

## Thesis Outlook

An introduction to the fundamentals of the magnetic resonance imaging is provided in Section 3, from the generation of the magnetic resonance signal to its transformation into images.

An insight into the usage of percutaneous minimally invasive procedures is given in Section 4. Advantages of procedure monitoring by means of magnetic resonance imaging are also described. The last paragraph focuses on thermal therapy by radiofrequency ablation and cryoablation, since the data sets used for the testing of the algorithms were acquired during real time guidance of such procedures.

In Section 5 the appearance of the needle in magnetic resonance images is investigated. Basic knowledge of the susceptibility properties of the material is provided and factors influencing the appearance of the needle artifact are reviewed. The last paragraph is dedicated to the techniques proposed in literature for device tracking.

Motivation for real-time automatic needle detection is discussed in Section 6.1. The analysis is performed with reference in particular to the framework, the Interactive Front End (IFE) [LKZ+05] within which the cited treatment workflow is implemented. A short paragraph is dedicated to introduce the eXtensible Imaging Platform (XIP), the development environment used. Details about the acquisition sequence used to monitor the positioning step are also provided.

Implementation details of the needle detection application are provided in Section 7 with reference also to the modules developed in C++ extending the functionalities provided by the standard XIP environment. The first algorithm is based on the Hough transform. The second presents a more heuristic approach, exploiting the characteristics of the small eigenvalue and algorithms for edge linking. Both the proposed methods aim to determine the needle centerline in order to provide position information in terms of translation and orientation offset that could be exploited for automatic slice realignment. Further, position feedback could be also given to the physician. Algorithms evaluation and critical discussion are presented

respectively in Section 8 and 9. In the latter, further development and impact of the implemented algorithms are considered.

# 3 Magnetic Resonance Imaging Fundamentals

Magnetic resonance imaging is an imaging technique which exploits the interaction betweeen a magnetic field and nuclei. In clinical applications the nucleus under investigation is hydrogen $^1H$. MRI represents an extraordinary tool that can provide a superb anatomical and functional insight into the human body. A conscious usage of such a technology can not be achieved without grasping its very first fundamentals. In the following, a short introduction into the basic concepts of MR signal origin and generation is presented. The major references for this sections are found in *Totally Accessible MRI: A User's Guide to Principles, Technology, and Applications* [Lip08] and *MRI: Basic Principles and Applications* [BS03]. The mathematical formulation refers mainly to *MRI from Picture to Proton* [MMG03].

## 3.1 Nuclear Spin and Macroscopic Magnetization

The MR signal has its fundamentals in a phenomenon called *nuclear magnetic resonance* (NMR). NMR involves some elements like hydrogen, that present a nonzero magnetic moment. Just elements, which have either an odd number of protons or of neutrons, are characterized by a spin angular momentum **I**. It is worth noticing that at least one isotope of every element, except argon and cerium, presents this feature [Lip08].

The spin angular momentum is related to the rotation experienced by the nucleus of an atom about an axis. The rotation occurs at a constant velocity rate. The values which can be assumed by **I** are quantized. However, the value itself is not relevant, but has to be different from zero, since just elements with spin other than zero can interact with an external magnetic field and thus being exploited in the signal generation.

In the following just the *protium* $^1H$, the hydrogen isotope consisting of only one single proton, is considered. The human body is for the most part made of water. Thus, protium represents the ideal element to be investigated within an MR procedure.

Another important aspect to be taken into consideration is the magnetic moment associated with each protium atom, that is due to its positive charged nucleus. This local magnetic field is oriented parallel to the axis of rotation.

The former described properties are usually incorporated in a vectorized representation of the atom: an atom of $^1H$ is represented as a vector, with a specific orientation and magnitude, directed parallel to the axis of rotation.

The microscopical organization of the nuclear spins in a generic volume of tissue is illustrated in Fig. 3.1a. The spins are randomly distributed within the volume. The result of the sum of all the single spins/nuclear vectors is a quantity called

*net magnetization vector.*

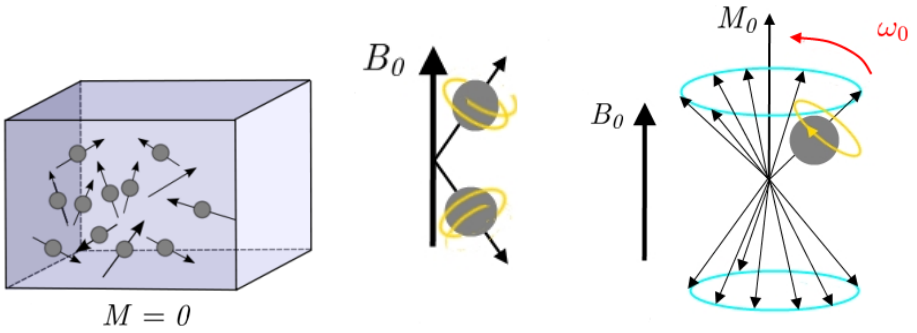


Fig. 3.1: Spin Precession. (a) The microscopic distribution of spin angular momentums in absence of an external magnetic field is shown. (b). In the presence of an external magnetic field the spins align along the direction of $B_0$. The majority of them will be in the low energy configuration. The protons still conserve the randomness of their phase distribution. This guarantees the presence of a macroscopical nonzero magnetization vector parallel to $B_0$ as depicted in (c). Figure adapted from [HBL04] Fig. 3-3.

The net magnetization is zero in a rest state, as a consequence of the random distribution of the spins. When an external homogeneous magnetic field $\mathbf{B_0}$ is applied, the spins align now parallel or anti parallel to the magnetic field, loosing their original random orientation, with a slight majority of spins aligned along the parallel direction. In terms of energy this implies a redistribution of the spins through the two energy states allowed. The ratio between the number of spins distributed between the two energy levels is reported in Eq. 3.1 and is expressed through the Boltzmann distribution:

$$\frac{N_{up}}{N_{down}} = e^{-\frac{\Delta E}{kT}} \tag{3.1}$$

$$\Delta E = E_{up} - E_{down} = \hbar\omega_0 = \hbar\gamma B_0, \tag{3.2}$$

where

$\Delta E$ : *energy difference between the two energy states allowed for* $^1H$
$h$ : *Planck constant* $6.626 \cdot 10^{-34}$ *Js*,
$\hbar = h(2\pi)^{-1}$ : *reduced Planck constant* $1.055 \cdot 10^{-34}$ *Js*,
$k$ : *Boltzmann constant* $1.381 \cdot 10^{-23}$ $JK^{-1}$,
$T$ : *absolute temperature in Kelvin.*

Another consequence of the interaction between $\mathbf{B_0}$ and the $^1H$ nuclei is the *precession* of the spins vectors about the external field pursuing a conical trajectory. The phase remains random (see Fig. 3.1c). This ensures the formation of a macroscopical net magnetization vector $\mathbf{M_0}$, that is parallel to $\mathbf{B_0}$ and different from zero. The frequency at which the spins precess depends on the applied external magnetic field. The relation is expressed by the *Larmor equation*:

$$\omega_0 = \gamma B_0 \tag{3.3}$$

where

$$\begin{aligned} \omega_0 &: \textit{frequency of precession} \\ \gamma &: \textit{gyromagnetic ratio given in } MHzT^{-1} \\ B_0 &: \textit{external homogeneous magnetic field given in Tesla} \end{aligned}$$

The sum of all the spins yields to a nonzero net magnetization, having the same orientation of the external field. The net magnetization vector is commonly thought as composed of a longitudinal component $\mathbf{M_l}$ parallel to $\mathbf{B_0}$ and a transversal component $\mathbf{M_t}$ orthogonal to the latter. If a right-handed Cartesian coordinate system is introduced, with the $z$ axis parallel to the external magnetic field, the following correspondences are usually established in literature:

$$\begin{aligned} \mathbf{M_l} &= \mathbf{M_z}; \\ \mathbf{M_t} &= \mathbf{M_{xy}}; \end{aligned}$$

## 3.2 MR Signal Generation

In the previous section it was shown how a magnetic field can interact with the $^1H$ atoms present in a sample, like the human body in a clinical application. To benefit from the magnetic resonance phenomenon, a signal has to be measured. The measurement exploits what stated by the law of Faraday, according to which a magnetic field varying in space and time can produce an electric field in a conductor.

The first requirement is a variant magnetic field: the net magnetization is therefore flipped in the transversal plane. Direct measurements of $M_0$ would also be difficult, since $M_0$ is negligible compared to the magnitude of the external field $B_0$ [Lip08].

In the presence of $B_0$, a second magnetic field $B_1$ perpendicular to the static field and at $\omega = \omega_0$ is applied. $B_1$ is transmitted in the form of a radiofrequency pulse,

RF pulse. The frequency correspondence permits to transfer energy to the system of spins under investigation. The energy transmitted induces a redistribution of the spins within the energy levels, leading to a higher energy configuration state, where the higher energy level predominates. The spins tend to align to the new magnetic field: the phase coherence of the group of spins increases and causes the $M_0$ to flip to the $xy$ plane. In this state $M_{xy}$ is present, while $M_z$ disappears.

In the $xy$ plane the signal can be recorded by a receiver coil. After the RF pulse ends, the system returns spontaneously to the original configuration, since the latter is characterized by a lower energy state. The dephasing occurring causes diminishing of the signal. This phenomenon is called relaxation and is in particular due to two contributions. The first is the *spin-lattice* relaxation and involves the energy dispersion by means of transfers between the nucleus and the surrounding lattice structure. This is responsible for the recovery of $M_z$. The second is the *spin-spin* relaxation, that causes loss of phase coherence due to spin-spin interaction (see Fig. 3.2). The latter is responsible for the $M_{xy}$ disappearance.

The disappearance of $M_{xy}$ provides the so desired variant magnetic field. The signal resulting is called Free Induction Decay (FID). The FID has a time course described by Eq. 3.4 and illustrated in Fig. 3.3.

$$M_{xy} \propto e^{-\frac{1}{T_2}} \tag{3.4}$$

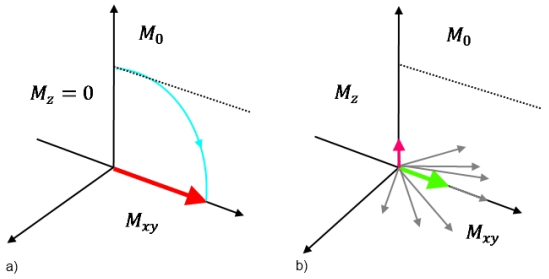


Fig. 3.2: Spin-Lattice and Spin-Spin Relaxation. When the RF pulse is turned off the energy acquired by the spins is lost as a consequence of Spin-Lattice and Spin-Spin Relaxation processes. The spin-spin relaxation involves the energy transfer between the single spins and determine the decline of $M_{xy}$. The spin-lattice relaxation refers to the energy transfer from the protons to the lattice. The latter is responsible for the recovery of $M_z$. Figure adapted from [BS03] Fig. 3-4.

The spin-lattice relaxation is characterized by the time constant T1, whereas T2 refers to the time constant of the spin-spin relaxation. It is worth noticing that the two relaxation processes are independent from each other, and hence also their time constant. Relaxation depends on the histological properties of the tissue under examinations. Different tissues induce different signal decays and are therefore associated with individual time constants. Also other several parameters, like proton density, can be investigated, inducing the signal acquired to be more sensitive to a parameter than to others.

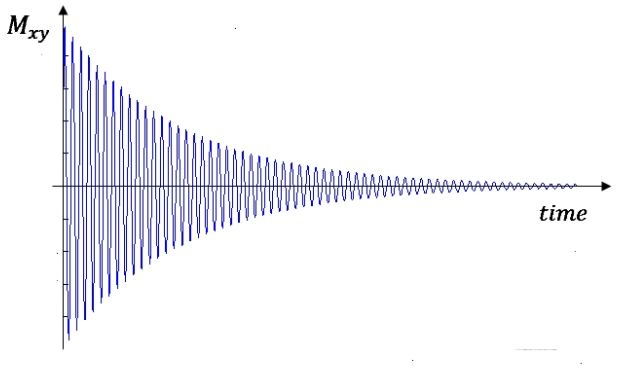


Fig. 3.3: Free Induction Decay. Signal deriving from the decay of the transverse magnetization. The time constant $T_2$ determines the diminishing rate of the exponential term

## 3.3 Spatial Encoding

The MR signal is the result of the contribution of all the protons, which undergo the resonance phenomenon. If no further processing is applied, the whole body of a patient could be involved in the signal generation, thus providing rather meaningless information. In order to take advantage of the MR, it is necessary to be able to localize the spatial location of the source of this signal. To identify a point in 3D space, the usual $x, y$, and $z$ coordinates need to be provided. The solution to the problem resides in a simple but powerful concept: *frequency is location* [Lip08].

The key of the encoding of an MR signal is the exploitment of the Larmor equation, that states the dependence between the precession frequency and the magnet field experienced by the spins. According to the Larmor equation, it is possible to manipulate the rate of precession selectively, applying various magnetic gradients. The resulting $\omega$ is expressed by the so called *expanded Larmor equation*:

$$\boldsymbol{\omega_i} = \gamma(\mathbf{B_0} + \mathbf{G}\mathbf{r_i}), \tag{3.5}$$

where

$\boldsymbol{\omega_i}$ :*precession rate at position* $\mathbf{r_i}$,
$\mathbf{r_i}$ :*position of the spin*,
$\mathbf{G}$ :*additive magnetic field experience at position* $\mathbf{r_i}$;

### 3.3.1 Slice Selection

Keeping in mind the relation between the precession frequency of the spin and the external magnetic field, it is possible to proceed with the MR signal acquisition. The first step is the selection of the slice of interest. The process consists of

a selective spatial discrimination of the protons which contribute to the signal generation and is carried out by applying a gradient magnetic field $G_{SS}$ and a radiofrequency pulse. The gradient ensures that the protons precess at a different $\omega$ depending on their location along the direction of the gradient, for example $z$. $G_{SS}$ is referred in this case as $G_z$ The RF pulse transmitted by switching on $B_1$, characterized by a frequency $\omega_1$, guarantees that just the protons precessing at $\omega = \omega_1$ undergo the resonance phenomenon.

Due to the hardware limitations, a whole bandwidth of frequencies $\Delta\omega$ is transmitted. All the protons that resonate with any of the frequencies in the interval $|\omega_1 - \frac{\Delta\omega}{2}|$ are excited, thus resulting in a finite slice thickness $\Delta z$.

The frequency bandwidth is not the only factor influencing the thickness of the slice. Also the gradient strength contributes, reducing or augmenting it in a proportional manner. As illustrated in Fig. 3.4, the steeper the magnet gradient, the thinner the slice thickness.

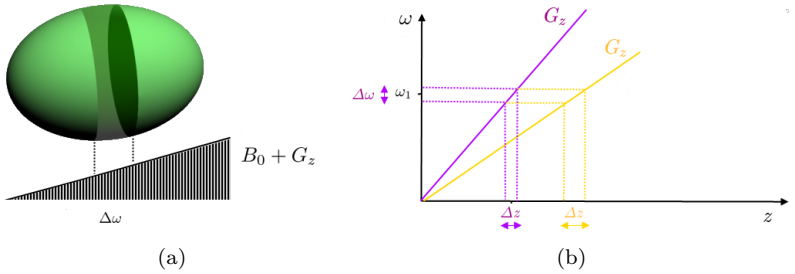


Fig. 3.4: Slice Selection. Transmission of a radiofrequency pulse rotating at $\omega_1$ excites all the proton precessing at equal frequency. (a) The actual transmission of a bandwidth $\Delta\omega$ results in the excitation also of the protons right close to the central frequency $\omega_1$. (b) A steeper gradient provides a narrowed frequency range, thus diminishing the slice thickness. Figure adapted from [HBL04] Fig. 10-12.

### 3.3.2 Frequency Encoding

After the desired slice is selected, locations within the slice itself need to be discriminated. Due to the excitation induced by $G_{SS}$, all the protons precess at the same speed, for example $\omega_0$, and in phase. A first step involves the application of a second linear gradient $G_{FE}$, applied for example along the $x$ direction. According to the Larmor equation, protons precess at different frequencies depending on the overall magnetic field experienced. The latter depends on the $x$ position at which the single protons are located:

$$\omega(x) = \omega_0 + \gamma G_x x, \tag{3.6}$$

where

$$\begin{aligned} \omega(x) &: \textit{precession frequency at location } x, \\ \omega_0 &: \textit{initial precession frequency within the slice}, \\ G_x &: \textit{gradient applied along the } x \textit{ direction}. \end{aligned}$$

The gradient strength is usually zero at the isocenter and increases towards the periphery of the Field of View (FOV). In the schematic representation depicted in Fig. 3.5, the signal produced by each voxel is approximated by a sinusoidal wave. The different colors and amplitudes of the signals aim to represent the different signal intensities. Before the application of $G_{SS}$, all spins are characterized by the same frequency. The individual voxel contribution to the overall signal would therefore differ just in terms of intensities. However, after the gradient application, all voxels within the same column add a characteristic frequency component. During the signal read-out, the signal received is modulated by all the frequency components, since the entire slice contributes to its generation.

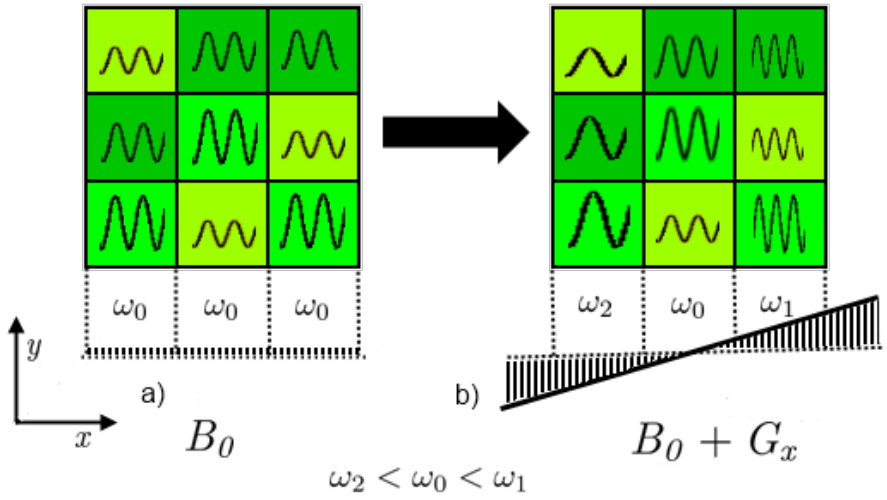


Fig. 3.5: Frequency Encoding. a) The spins are still excited after the application of the $G_z$ gradient and precess therefore at the same frequency. b) The application of a second gradient along the orthogonal $x$ direction induces the spins to change their precession frequency according to the $G_x$ experienced at the specific $x$ location. Figure adapted from [HBL04] Fig. 11-4.

### 3.3.3 Phase Encoding

The last step in spatial localization is *phase encoding*. It is the only one involving a time-varying gradient $G_{PE}$. $G_{PE}$ is perpendicular both to $G_{SS}$ and $G_{FE}$.

In Fig. 3.6 the concept of phase encoding is illustrated. At the beginning all the protons precess at the same frequency and in phase, as illustrated in the Fig. 3.6a. When $G_{PE}$ is switched on, according to the Larmor equation, protons at different positions precess at different frequencies, depending on the gradient experienced.

In other words the $^1H$ elements precess all at different velocities. As a consequence, when the gradient stops, they have a different phase compared to the starting one. The amount of dephasing gained varies in relation to the location of the single proton, as illustrated in Fig. 3.6b. The effect of the application of the gradient along the $y$ direction on the precession frequency is described by the following equation:

$$\omega(y) = \omega_0 + \gamma G_y y, \tag{3.7}$$

$$\omega(y) : \textit{precession frequency at location } y,$$
$$G_y : \textit{gradient applied along the } y \textit{ direction.}$$

If the gradient is applied for a time interval $t_y$ the resulting induced phase shift is:

$$\phi_y = \gamma(\int_0^{t_y} G_y(\tau)d\tau)y \tag{3.8}$$

The result of the dephasing is a diminishing of the overall protons coherence, which manifests macroscopically as a reduction of the net magnetization and hence as an attenuation of the signal.

The outcome of the whole space encoding process is summarized in box Fig. 3.6c. After the application of all the gradients, $G_{SS}$, $G_{PE}$ and $G_{FE}$, each location in space differs from the other in its frequency and phase components. At each read-out the signal acquisition is performed with a different strength of $G_{PE}$.

### 3.3.4 K-Space

The outcome of the spatial encoding step is the acquisition of the so called raw data matrix, referred to as *k-space*. The origin of the name will become clearer in the following paragraph. As mentioned in the previous section, each read-out is performed using a different strength of the phase gradient. The signal acquired results from contributions coming from the entire slice. The samples of each signal, derived from the discretization process exploited by the receivers, fill a line in the data matrix. The central row refers to the read-out accomplished when no $G_{PE}$ was active. A further position from the central vertical row relates to a greater phase gradient applied and hence a greater dephasing experienced by the protons.

Due to the increasing dephasing, the intensity of the received signal diminishes as shown in Fig. 3.7. The vector distributions depicted in the small boxes aim to illustrate how the samples at the extreme locations in the data space correspond to the greatest dephasing.

Each row of the data space is filled within a repetition time (TR) of the applied sequence. TR refers to the time interval between two subsequent applications of

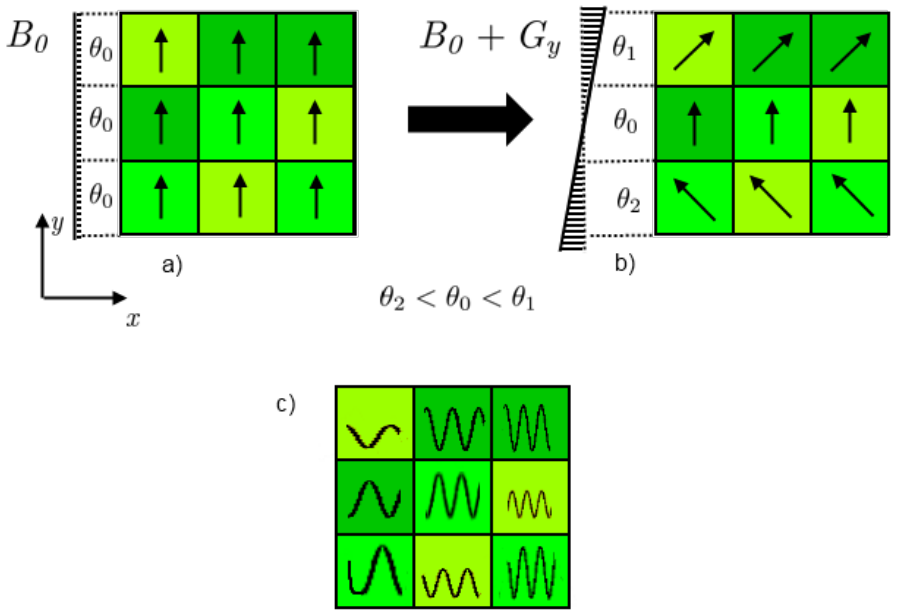


Fig. 3.6: Phase Enconding. a) Before the gradient is turned on, the protons present no difference neither in frequency or in phase. b) After $G_{PE}$ application, a permanent phase shift is present between protons located within different rows. c) The overall effect induced by the application of $G_{SS}$, $G_{PE}$ and $G_{FE}$ is shown. The signal contribution of a single voxel differs in frequency and phase from all the others. Figure adapted from [HBL04] Fig. 11-10.

the acquisition sequence. In order to fill a matrix of size $N$x$M$, excitation has to be applied $N$ times and for each signal acquired, $M$ sample need to be collected. Thus, it appears clear that, in order to have all the matrix filled, a time equal to $N \cdot TR$ is required.

### 3.3.5 From the K-Space to the MR Image

Before an image can be displayed, the information encoded in frequency and phase terms needs to be taken back to the physical space, in order to assign to each voxel location the corresponding intensity. Let us consider a small element in the slice. Its contribution to the signal formation can be expressed as follows:

$$s(t) = I(t,x,y)\underbrace{e^{(j\gamma x G_{FE} t)} e^{(j\gamma x G_{PE} \tau)}}_{M(G_{FE},G_{PE})} dxdy, \tag{3.9}$$

where

$$I(t,x,y) = \int_{z-\frac{\Delta z}{2}}^{z+\frac{\Delta z}{2}} I(t,x,y,z)dz$$

$\Delta z$ : *slice thickness*

$t$ : *time at which the FID is sampled*

$\tau$ : *duration of the phase encoding gradient*

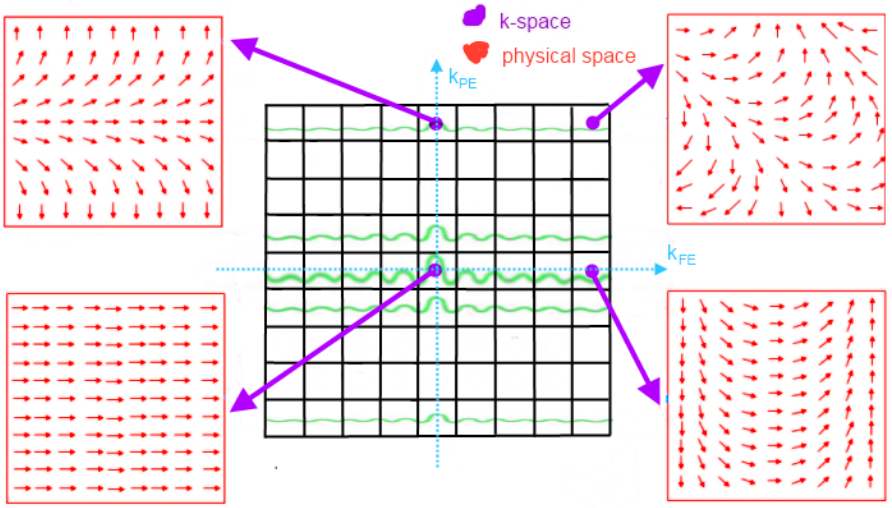


Fig. 3.7: In this figure the schema of the k-space is illustrated. Each point of the k-space corresponds to an amplitude signal measurement containing information coming from the whole slice. Adapted from [Son05] and [HBL04] Fig 13-1.

$I(t,x,y)$ represents the amplitude of the FID signal at the time $t$ induced by all the protons located inside the element $dxdydz$, remembering that a slice has a finite thickness. The amplitude is modulated by the term $M(G_{FE},G_{PE})$. The MR signal received results from the sum of contributions coming from all the elements in the slice.

$$M_{xy}(t,G_{FE},G_{PE}) = \iint_{slice} I(t,x,y)e^{(j\gamma x G_{FE}t)}e^{(j\gamma x G_{PE}\tau)}dxdy \tag{3.10}$$

With reference to Eq. 3.10 and defining the following quantities

$$k_x = \frac{\gamma G_x t}{2\pi} \qquad k_y = \frac{\gamma \int_0^t G_y(\tau)d\tau}{2\pi}$$

it is possible to express the MR signal as a function of $k_x$ and $k_y$

$$M_{xy}(k_x,k_y) = \iint I(t,x,y)e^{j2\pi[k_x x+k_y y]}dxdy \tag{3.11}$$

The signal intensity $I(t,x,y)$ can therefore be obtained through Fourier transform (FT) of the k-space, $I(t,x,y) = FT[M_{xy}(k_x,k_y)]$:

$$I(t,x,y) = \iint M_{xy}(k_x,k_y)e^{-j2\pi[k_x x+k_y y]}dk_x dk_y \tag{3.12}$$

The Fourier transform allows the decomposition of the whole signal in its constituent components, which are the signal intensities of the single voxels, individually characterized by a unique combination of frequency and phase.

The further a point is located from the central vertical line of the k-space, the greater is the frequency encoding gradient that contributed to the signal formation, to which it belongs. The peripheral regions of the data space hold informations about the contours of the image, characterized by higher spatial frequencies. On the other hand, the closer a point to the data space origin, the smaller is the modulation induced on the signal from $G_{FE}$ and $G_{PE}$. This means higher signal amplitude and higher signal to noise ratio (SNR). Therefore, the central regions of the k-space supply contrast to the image. A reconstruction of the image, performed omitting the center of the k-space, preserves mainly just the image contours. Conversely, a reconstruction, which exploits the center of the k-space, leads to an image with high contrast but blurred contours.

# 4 Percutaneous Minimally Invasive Procedures

The category percutaneous minimally invasive procedures refers to surgical interventions where a needle is used to reach the target organ and perform the intervention. They represent a new frontier in the field of medical interventions and their employment spread during the last decades, thanks in particular to the attractive perspective of a surgical intervention, that can be achieved locally and with the minimal invasiveness. Image guidance needs to be provided during the intervention. In the following chapter, the employment of percutaneous minimally invasive procedures, together with image monitoring by means of magnetic resonance imaging is investigated. Since this work is based on MRI acquisitions performed during cryoablation and radiofrequency ablation (RFA) interventions, also a brief description of the mentioned treatment methodologies is provided.

## 4.1 Advantages of Percutaneous Minimally Invasive Procedures

The employment of percutaneous minimally invasive procedures is not a novelty. They represent for example a standard approach in case of biopsy. Biopsy is usually performed in case of suspected neoplastic tissue formations. The procedure consists in extracting tissue samples from a patient, in order whether to diagnose the disease or to determine the extent of the disease. The decision is made after the samples underwent a histopathological analysis [Bed02]. Depending on how the extraction of tissue samples is performed, biopsy can be classified in different categories. Worth remembering is the *fine-needle aspiration biopsy*. In this case, a needle is used to reach the suspicious structure to remove some of its cells, without preserving the histological structure. It can be performed both on superficial and deep organs, such as lung and liver. Fine-needle aspiration biopsy performed on lymph nodes, for example, allows early and targeted identification of affected lymph nodes. The procedure is fast and can avoid the patient to undergo resection surgery [Bed02].

However, the great interest that lately arose in percutaneous minimally invasive procedures concerns the extension of their application to the field of medical interventions. The most peculiar feature, in comparison with standard surgery, is the marked reduction of invasiveness. To this new category belong interventions like thermal ablation, cryoablation and catheter based procedures. This kind of approach offers the appealing perspective to change the common vision associated with surgery, mainly characterized by organs exposure. As with every new technique, advantages and disadvantages need to be considered, always keeping the interest of the patient as the leading term of reference.

During an open surgery, the physician can benefit from a direct insight into the patient. This aspect represents a key advantage for example in case of tumor resection. If the pathology spread during the time between the planning and

the surgery, the physician has the possibility to operate also on the new encountered masses. The same extemporaneous rearrangement of the intervention can be needed also when some cancer formations happened to elude diagnosis. In case of emergency, an open approach is usually the only practicable way. In addition, minimally invasive procedures advocate for planning, that can not be provided in an emergency context.

A patient with a higher body mass index (BMI) is usually affected by hypertension, that is higher blood pressure. Common recognized consequences are developing of heart diseases, malfunctioning of the kidney, damages of blood vessels and elasticity loss of arteries walls. The latters are often responsible for augmenting the risk of stroke [GCC+05]. These factors can cause an aggravation of cardiovascular conditions of the patient during an open surgery. Moreover, a corpulent patient could advocate for a larger incision which causes more bleeding, stitches and pain.

High risks of infection are associated with standard surgery [BH+05]. A smaller incision could reduce the incidence of infection, thus diminishing bacteria access and proliferation [CAC+97]. However, tests on a large number of patients still need to be performed.

An intervention under general anesthesia entails always risks for the patient, risks that worsen in case of geriatric subjects. Elderly people are more prone to respiratory and heart failure, in particular when relevant procedures, like heart surgery, need to be performed [McL97]. A minimally invasive procedure could allow the employment of local anesthesia, as already reported by Dupuy et al. when performing percutaneous radiofrequency ablation on lung malignancies [DZA+00].

Last but not least is the cosmetic implication. An incision results in a visible scar on the skin of the patient. Its cosmetic appearance can be improved when recurring to a minimally invasive procedure and could therefore gather a higher acceptance from the patient. In case of valvular heart disease, for example, some interventions regarding valve repair or replacement are performed by means of complete median sternotomy. During this procedure, access to the heart is achieved through division of the sternum. In case of ministernotomy, minimally invasive valve surgery can be performed through a small incision in the chest wall. Instead, a minimally invasive percutaneous approach exploits access provided by the femoral vasculature [RFB+08].

Advantages and disadvantages reported above aimed to present the controversy that still orbits around the employment of percutaneous minimally invasive procedures. Before these procedures can gain general acceptance among the medical community, careful considerations need to be made, considering impact costs on the society and in particular the safety of the patient. Cost evaluation of a standard surgery involves, beside the mere procedure itself, also the usage of the OP room, anesthesia administration, sterilization protocols and an adequate surgical team. Moreover, the recovery of the patient can last days or weeks, depending on the severity of the intervention. A long-term staying represents an additional cost

for the society and can afflict the mood of the patient, impairing the follow up. However, less invasiveness and cost reduction should not impair the effectiveness of the procedure or the capability to reduce the rate of the pathology progression. If multiple minimally interventions are required to fully handle the disease, their employment needs to be considered carefully [RFB+08].

Rosengart et al. [RFB+08] pointed out also the difficulty encountered when trying to evaluate the effectiveness of the procedures. The group of patients that usually undergo percutaneous minimally invasive procedures, includes mostly geriatric subjects, corpulent people and pediatric patients. Nowadays such interventions are mostly still prescribed just to patients who could not survive to a standard surgery. This profile prevents the formulation of an acceptable comparison with standard procedures.

The development of new techniques is also required in order to respond to the necessities deriving from their employment and still a lot of work has to be done before these interventions can be regarded by the whole medical community as approved alternative in place of standard surgery, that is praised from decades of work. Relevant is anyway the fact that percutaneous minimally invasive procedures provide an alternative for patients otherwise excluded from standard surgery. The patient interest calls for further investigations of the potentiality of the new procedures, where medicine and technology once again need to collaborate together, with the promise of a further step in patient treatment quality.

## 4.2 Rational for MRI Guidance

In the previous section it was mentioned that one of the advantages offered by a traditional open surgery approach is the possibility for the surgeon to "see" inside the patient. In order to improve the quality of a percutaneous minimally invasive procedure, technology should provide in first place an insight into the patient. In an interventional context, such insight needs to be guaranteed continuously, allowing real time monitoring of the procedure. To this purpose, magnetic resonance image can be used.

The advantages provided by MR imaging are known. First of all it provides multiplanar imaging capability. This property refers to the ability of MR to acquire images at any orientation in space. Image generation is based on coils that generate gradients aligned to the three axis $x$, $y$ an $z$. The gradients induce then excitation of protons along the correspondent direction. Simultaneous combination of the three gradients result in gradients directed in every possible direction in space. The excitation of the protons, along the new created direction, provides the desired image plane. Thanks to this characteristic, MR is preferred to other imaging modalities, like Computed Tomography (CT), when the visibility of the region under investigation, along the standard radiologic direction, is impaired. If the tumoral mass is located inside the rib cage, for example, a double-oblique

plane would be desiderable.

In second place, magnetic resonance provides a superb soft tissue contrast, that is particularly appreciated in case of tumoral masses individuation and diagnosis. The first studies proving MR superiority in comparison with CT, date back to few decades ago. The higher performance includes tumor contours delineation, mass extension and contrast provided with respect to the surrounding tissue [AMB+86] [CMD+87].

Moreover there is no patient exposure to harmful radiation. The patient can therefore undergo all the diagnostic and follow-up process without receiving radiation dose, in addition to the one in case already administered during radiotherapy.

Techniques exploiting ultrasounds (US) also offer absence of radiation and can claim high image directionality. However, the visibility offered by US-based techniques can be mined by the presence of air or thick bones [Pro11]. If the region of interest is located in proximity of lungs for example, or concerns the lungs directly, the air can severely interfere with the correct imaging. MRI can be performed in the chest region without incurring in such complications.

The advantages offered by MRI make it one of the most preferred image modalities despite the high cost of the instrumentation and the need of a dedicated room in order to host the scanner and to isolate the magnetic field used. Despite the development of wide bore MRI scanner, magnetic resonance is still not available for obese people, since their body mass impairs their allocation inside the bore of the scanner. Pregnant women are also excluded from MR examination. Although no side effect was encountered since the first MR scanner employment, it is still preferable for the baby not to be exposed to such a magnetic field [Sof11].

In some applications MRI is still considered too slow and prone to be affected by patient movements. However, the last technological improvements promise a good overcome of the issues. Reliable acquisitions can nowadays be provided just in minor amount affected by involuntary movements, such as respiration and heart beat. The development of fast acquisition sequences also allows the employment of magnetic resonance in applications where speed is a key requirement like interventional procedures guidance.

## 4.3 Challenges in MR Interventional Environment

MRI usage in interventional applications does not dispense from safety and feasibility considerations. Significant adjustments are required in order to adapt the MR environment to an adequate surgical scene.

### 4.3.1 Limited Space Availability

An MR scanner is located inside a magnetic-isolated room, where normally the available space is reduced. When the MR scanner is intended to be use to guide an intervention, additional instrumentation is required. The anesthesia machine, for example, has to be compact and easy to move, in order to be transferred in and out from the scanner room. In addition, a monitor is needed to allow image visualization. In case of thermal ablation, space is also requested for the alimentation apparatus. As a consequence, the available area to the physician to manoeuvre is restricted.

### 4.3.2 MR Compatibility and Safety Requirements

Due to the strong magnetic field, access and operability inside the scanner room is regulated by strict rules. Patients carrying any ferromagnetic object such as surgical clips, metal implants and pacemakers, are forbidden to enter the scanner room. The magnetic field could for example interfere with the regular behavior of the pacemaker, altering the programmed functionality. Assistance devices like wheel chairs, standard litters and crutches are also excluded, making hard to transport inside and outside the room a patient with impaired moving capabilities. If an emergency situation occurs, both these aspects could delay the the first-aid assistance. If reanimation has to be performed, it could be necessary to transport the patient to the closest room suitably equipped, where for instance a defibrillator is host. Small ferromagnetic devices casually forgotten and brought inside the room, could turn out in dangerous projectiles when attracted into the bore of the scanner.

What is reported above also highlights the importance of using MR compatible devices. A non compatible instrument could impair the possibility of the physician to drive it in the proximity of the bore. This could also alter the homogeneity of the magnetic field, affecting the quality of the images acquired. Several are the efforts put into the development of MR compatible instruments like needles. Needles are made usually of titanium or titanium-alloys, since it is paramagnetic and has low thermal conductivity, thus reducing the undesired eddy current effect. As counter side needles made from titanium can not be sharpened enough and provide therefore a slight resistance, when penetrating the tissue [MMTZ08]. Alloys like nitinol and inconel are however the preferred materials in the production of MR compatible needles [Med10]. Without the development of MR compatible devices interventions inside the MR environment would not be practicable.

### 4.3.3 Sterilization

The highest possible sterilization level has also to be guaranteed. The physician and clinical assistants are in charge of sterilization procedures, like draping the

patient and sterilizing the instrumentation. However, despite all the precautions that can be adopted, the scanner area is not an operative room, and therefore it does not constantly undergo aseptic maintenance. The exposure of the patient to a higher risk of infection is hence possible.

## 4.4 Thermal Ablation

Another aspect, that can be enumerated among the advantages offered by MR procedure guidance, is the sensitivity of some of its parameters to temperature changes. Already in 1983, Parker et al. proposed a method for temperature measurement based on the time constant T1. The method finds its fundamental in the relation existing between the spin-lattice relaxation and thermal motion, consisting in a dynamic energy exchange that leads, eventually, to an equilibrium state.

Le and al. suggested a temperature mapping based on molecular diffusion of water, whose variations are temperature dependent. Molecular migration induces protons dephasing, thus causing signal attenuation. Once a diffusion reference image is obtained, temperature shifts from a reference temperature $T_0$ can be inferred. Diffusion values of subsequent images are reported to the initial value $D_0$ measured at the reference temperature: the diffusion difference encountered results then related to the temperature variation in a proportional manner [LBDL89].

In 1995, Ishihara et al. published a study, where the dependence existing between temperature and proton chemical shift was exploited. Chemical shifts are also responsible for spins dephasing. Once a proportional relation between amount of dephasing and temperature variation is established, temperature mapping can be derived recurring to phase images [ICW+95]. As described in section 3.3.4, individual voxel intensities $I(x, y)$ can be obtained by means of Fourier transform of the k-space. Given the complex nature of the resulting signal, both magnitude and phase images can be obtained. Phase images are nowadays still largely employed to produce temperature mapping, based on the temperature dependence proposed by Ishihara and his collaborators.

MR thermometry and temperature mapping are essential in thermal ablation procedures. Thermal ablation represents an example of cancer treatment based on *in situ* destruction of the neoplastic mass. It represents therefore an alternative to the standard surgical resection. The procedure can be either heating or freezing based. In such a context, it is therefore of great importance to be able to monitor temperature variations in the treated area and surroundings. This allows to keep the extension of the ablated region under control and to adjust treatment parameters, in order to ensure the effectiveness of the treatment.

### 4.4.1 Cryoablation

Cryoablation is a freezing-based ablation procedure employing low temperature between -40° and -80°, in order to cause destruction of abnormal cells like tumoral ones. It is performed mainly percutaneously inserting a needle inside the target volume and eventually used to "remove" heat from the desired region. Once the treatment starts, freezing and thawing cycles follow, inducing cells death.

Several causes are responsible for cell death during cryoablation. An exhaustive summary can be found in the work of Hoffman and Bishop [HB02]. During the procedure ice crystals form, both in the extra-cellular and intra-cellular space, thus inducing membrane destruction. Inside the cell, this means in first place the disruption of compartmentalization. Different chemical reactions can be performed at the same time inside the cells thanks to the partitioning provided by membranes. Once they are destroyed, the inner cell metabolism is impaired. Ice crystals are also responsible for the reduction of the amount of free water available, essential to the main metabolic reactions.

The water deprival perpetrated, affects also the osmotic equilibrium between the inner and outer cellular space. Ice crystals formation in the interstitial space and temperature cooling induce accumulation of solutes. In order to equilibrate solutes concentration between extra and intra-cellular space, water tends to move to the outside of the cell, further diminishing the inner water concentration and eventually leading to the cell death.

Blood supply is also disrupted due to coagulation phenomenon, that usually follows the thawing phase. Proteins, minerals and nutrient molecules are prevented to reach cells in the ablated region, contributing to the metabolic failure.

During the first weeks after the treatment, apoptosis can be observed at the periphery of the ablated region. The term refers to a gene-based mechanism that induces programmed cell death and that regulates several processes during the life of an individual, like embrion development and tissue homeostasis.

As depicted in Fig. 4.1, the needle is inserted till to reach the target region, located for example in the liver. The coolest temperature can be achieved in the proximity of the needle tip and increases with the distance from the needle. Attention needs to be paid in particular at the periphery, since a warmer temperature could not suffice to cell destruction. Depending on the size of the tumoral lesion, multiple needles can also be employed, in order to guarantee the treatment a complete covering of the malignant volume.

Cooling of the cryoablation probe can be accomplished either by means of pressurized argon or nitrous oxide, or recurring to liquid nitrogen. The latter is usually preferred as it allows faster freezing. A high efficacy of the treatment is based on the ability to induce fast cooling and slow thawing, hence favoring ice crystal formation and the recovery of cells functionality [HB02].

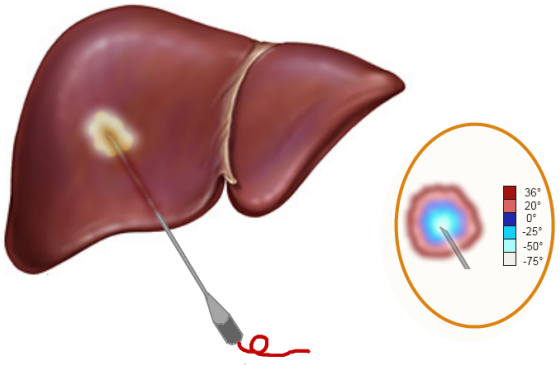


Fig. 4.1: The target volume is reached percutaneously by means of a needle. Once it is in place, the freezing and thawing cycle can start. Lower temperatures are reached near the needle tip, as illustrated in the color legend on the right side. Colors and temperature profile are freely depicted just for illustrating purpose. Figure adapted from [GH11] section *Hepatocellular Carcinoma (Liver Cancer): Therapy*.

### 4.4.2 Radiofrequency Ablation

Radiofrequency ablation consists in the usage of high frequency electrical currents, in order to induce necrosis formations. It is usually performed to treat unresectable tumors, for instance some hepatic malignancies. Neoplastic formations in the liver result often remarkably resistant to more standard treatments like radiotherapy and chemotherapy. RF ablation represents in this case the only practicable way [Cur01]. Pain management is also a field of application of RF ablation treatment. Goets at al. reported for example the efficacy in providing pain relief when RA was applied to bone metastasis [GCC+04]. Radiofrequency ablation is also more and more employed in cardiology in the treatment of atrial fibrillation [PRO+00] [CHT+99].

The apparatus includes a grounding electrode located on the patient skin, a RF generator and insulated wires connected to the electrodes of the needle and to the grounding one. Once the needle is in place, high frequency electrical currents induce heating of the surrounding area. The range of temperatures used varies between 50° and 100° and the ablation session can last 10-30 minutes. The adequate temperature is chosen trying to offer the best compromise between treatment duration and extension of the necrosis achievable [GGSL00].

A nice overview of factors, which can influence the effectiveness of the procedure is provided by Gazelle and colleagues [GGSL00]. Some needles are equipped with retractable electrodes, which can be pushed out to permit a larger volume to be directly affected by the current flow. Fig. 4.2 illustrates a simplified RF ablation apparatus where a multiprobe arrays approach is used.

A reduced vascularization, together with a higher amount of energy applied, contributes to diminish heat dispersion and tissue impedance. Therefore, in some liver interventions, occlusion of some supplying arteries or veins is performed [Cur01]. Conduction can be improved with normal or hypertonic saline solutions. This

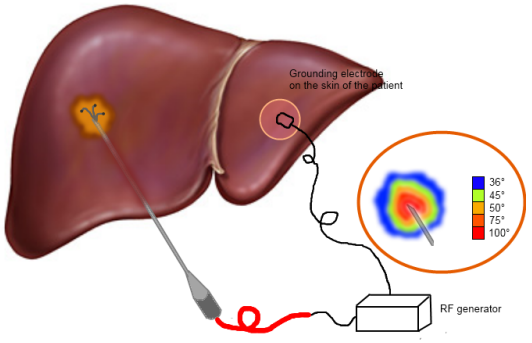


Fig. 4.2: As in cryoablation procedure needle is inserted percutaneously inside the neoplastic mass. In case of multiprobe array, the electrodes are pushed out after the needle reached the predefined target. The temperature decreases as the distance form the tip of the probe increases. Colors and temperature profile are freely depicted just for illustrating purpose. Figure adapted from [GH11] section *Hepatocellular Carcinoma (Liver Cancer): Therapy*.

perfusion allows usually to achieve a bigger lesion, but its usage has to be consider carefully, since the dispersion of the solution through the blood circulation and tissues is not easily predictable.

Addition of cool probes inside the needle can favorably influence heat propagation, avoiding rapid necrotization around the needle tip. If the process is too rapid, the impedance could raise too fast and thus limit heat propagation [GGSL00].

# 5 Management of Needle Artifacts

In the past few years the advent of wide bore MR systems opened the doors to a new challenging field of application for magnetic resonance imaging. The idea is to profit from the high soft tissue contrast and the multiplanar imaging capability in order to provide a feasible monitoring tool during minimally invasive procedures. The usage of surgical instrumentation with metal components represents nevertheless a source of interference with the magnetic fields employed by the MR imaging modality, altering the information depicted in the monitoring images. The effects of these magnetic field alteration are referred to as artifacts. When dealing with percutaneous minimally invasive procedures the major source of artifact is the susceptibility artifact associated with the interventional needle. The following section aims to give an insight into sources of needle artifacts and factors influencing them, in order to provide a better understanding of the problems encountered by physicists and physicians when dealing with intraoperative monitoring. The major reference for the mathematical formulation of the magnetic susceptibility is "Elementi di Fisica - Elettromagnetismo" by Nigro-Voci [MNV05].

## 5.1 Physical Principles of Susceptibility Artifacts

Magnetic susceptibility describes the extent to which material becomes magnetized in response to an applied magnetic field. The magnetic susceptibility $\chi_m$, expressed in dimensionless units, is defined by the following ratio:

$$\chi_m = \frac{\mathbf{M}}{\mathbf{H}}, \tag{5.1}$$

where

$\mathbf{M}$ : *magnetization in ampere per meter*,
$\mathbf{H}$ : *magnetic field strength in ampere per meter.*

The magnetic field strength $\mathbf{H}$ is expressed as the ratio between the magnetic field $\mathbf{B_0}$ and the magnetic constant $\mu_0$:

$$\mathbf{H} = \frac{\mathbf{B_0}}{\mu_0}, \tag{5.2}$$

where

$\mathbf{B_0}$ : *magnetic field expressed in tesla*,
$\mu_\mathbf{0}$ : *magnetic constant* $1.25710^{-6}$ *in henry per meter.*

$\mathbf{B_0}$ can for example be generated by induction as a consequence of the current flow through a homogeneous solenoid. If the solenoid is filled with a homogeneous material, the magnetic field experienced changes. The effect of a homogeneous

material placed in the vacuum is expressed by the magnetization $\mathbf{M}$ defined as follows:

$$\mathbf{M} = \frac{\mathbf{B_m}}{\mu_0} \tag{5.3}$$

where

$$\mathbf{B_m} : \textit{variation of the magnetic field due to the magnetic properties of the material expressed in tesla.}$$

The total magnetic field can therefore be expressed as the sum of two components, the magnetic field $\mathbf{B_0}$ and the magnetic variation induced by the presence of the material $\mathbf{B_m}$:

$$\begin{aligned} \mathbf{B} =& \mathbf{B_0} + \mathbf{B_m} \\ =& \mathbf{B_0} + \mu_0 \mathbf{M} \\ =& \mathbf{B_0} + \mu_0 \chi_m \mathbf{H} \\ =& \mu_0 (1 + \chi_m) \mathbf{H}. \end{aligned} \tag{5.4}$$

Depending on the value of the magnetic susceptibility $\chi_m$, the substances can be classified in diamagnetic, $\chi_m < 0$, paramagnetic, $\chi_m > 0$ and ferromagnetic. In the latter case the value of $\chi_m$ is also depending from the value of the magnetic field. As a consequence the value of the magnetic field varies according to the substance immersed in the field Eq. 5.4. Paramagnetic substances cause an increase of the magnetic field, whereas diamagnetic substances produce a reduction of the magnetic field. Most of biological tissues and molecules, water included, are diamagnetic [RP06].

Susceptibility properties are exploited in some clinical applications. The susceptibility is for example one of the causes of the bold phenomenon used in functional MRI in order to investigate the activity in the brain. Here the combination of the magnetic properties of oxygenated hemoglobin, deoxygenated hemoglobin and blood supply determines the variation of the MR signal recorded. This allows the determination of the brain areas that are more active during a particular task [MB00].

The characterization of the susceptibility differences of some specific tissues in comparison to other tissues and the background is also exploited to recognize subvoxel structures like vessels. In this case, phase images are used in combination with different TE values in order to augment the dephasing caused by the simultaneous presence of more than one tissue, and thus susceptibility differences among tissues inside the same voxel [Haa04].

Apart from some specific and aimed usages of the susceptibility effect, usually the presence of an object with magnetic properties needs to be considered carefully as it entails as side effect dephasing and alteration of the resonance frequency of the protons. Since the resonance frequency depends on the field experienced by the

protons, such an alteration affects the frequency spatial encoding leading to signal loss and geometric distortion. The dephasing is responsible for the acceleration of the transverse relaxation and consequently also for the decay of the signal, as illustrated in Section 3. McRobbie et al. [MMG03] expressed the dephasing as a function of the gradient $G_i$, present for example at the interface between two tissues with different susceptibility, the size of the voxel $\Delta$r and the echo time TE. According to Eq. 5.5 one of the first way to reduce the susceptibility artifact could be to reduce the TE and the voxel size [MMG03].

$$\Delta\phi = \gamma G_i \Delta r TE \tag{5.5}$$

Shifts in precession frequency also contribute to the diminishing of the signal. When slice selection is performed, the mismatch between the frequency planned for the desired slice and the actual precessing frequency owned by the protons causes a missed spin excitation and as a consequence an absence of signal [Hoa09].

However, the major side effect deriving from the alteration of the precession frequency is the modification of the linear frequency variation expected with the application of the gradients during the readout step. Since location encoding is frequency based, the alteration of the expected frequency is translated in erroneous determination of the spatial position, producing the above mentioned geometric distortions.

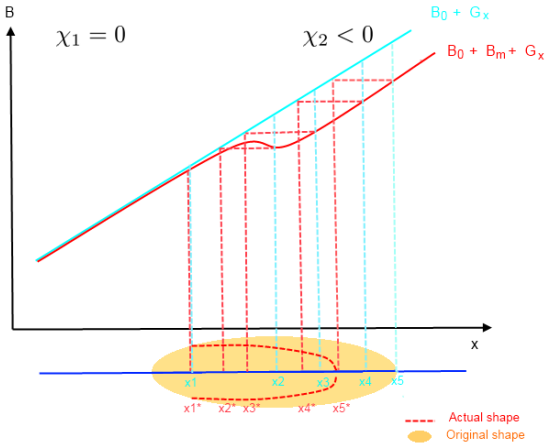


Fig. 5.1: Illustration of the effect of the presence of two adjacent tissues with different $\chi$. Ideally $\chi_1 = 0$ and $\chi_2 < 0$. This difference leads to inhomogeneities in the main magnetic field. Such inhomogeneities are responsible for an erroneous encoding of the spatial location of the body element which generates the signal. Figure adapted from [MMG03].

The above described behavior is shown in Fig. 5.1. Let us assume the presence of two adjacent tissues. The first tissue presents ideally a susceptibility $\chi_1 = 0$, whereas the second tissue is characterized by a negative susceptibility $\chi_2$. According to Eq. 5.4, under exposition of the main magnetic field $\mathbf{B_0}$ of an MR scanner,

the total magnetic field $\mathbf{B}$ experienced in the region occupied by the diamagnetic tissue is smaller than the expected $\mathbf{B_0}$. When a linear gradient is applied, for example $\mathbf{G_x}$ along the $x$ direction, the spatial encoding erroneously determines the location of the source of the signal. The points which should be mapped to $x_2$, $x_3$, $x_4$, $x_5$, expecting a linear variation of the gradient, are translated instead to the spatial location $x_2^*$, $x_3^*$, $x_4^*$, $x_5^*$, deforming the actual shape of the object.

During a percutaneous minimally invasive procedure a needle is used to reach the target organ. The insertion of the needle in the body causes a rearrangement of the tissues that surround the path it follows. The tissue, and as a consequence the constituent water molecules, are pushed apart. The effect is an increased water molecules density in the needle surrounding, translated in signal intensity augment in the image context.

Since the needle does not contain water molecules able to resonate, no signal is generated. This is referred to as signal void. The needle appears therefore as one of the darkest features in the image (see Fig. 5.2). In an MR acquisition the alteration of the information due to the susceptibility properties is particularly present at the boundaries of the device, which represents also the regions of greatest interest during the intraoperative monitoring. In particular, when the intervention concerns really delicate areas like brain and spinal column, the precision gains more and more importance since even millimeters of erroneous displacement of the needle can severely compromise the result of the intervention. In such a context titanium and nitinol are preferred to steel in order to profit from their small magnetic susceptibility [MBGL+04].

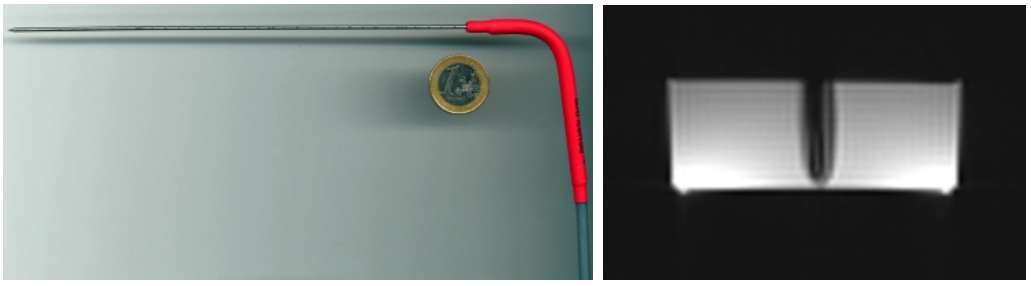

(a) Cryoneedle 17Gauge, GALIL MEDICAL, Yokneam, Israel

(b) Cryoneedle needle appearance in an MR image

Fig. 5.2: Example of image alteration deriving from the susceptibility property of the needle material. The needle manifests as a signal void and the shaft results wider.

## 5.2 Sources of the Needle Artifact

Needle artifacts were widely investigated in literature and several are the factors recognized as affecting its appearance. Butts et al. [BPD+99] reported that the sampling bandwidth (BW) affects the deformation induced by the surgical instru-

ment. The bandwidth expresses the range of frequencies investigated pro pixel. A larger BW means therefore that a smaller amount of shifted protons matches the desired frequency, diminishing the contribution to the signal loss [RP06].

Butts et al. [BPD+99] showed also that the apparent centerline of the needle visible in an image is actually shifted with respect to the real needle shaft location. This misplacement is more pronounced when the needle shaft is oriented perpendicular to the frequency encoding direction, as well as the widening of the needle shaft depicted in the image. In order to reduce the amount of tissue made not visible by the artifact the frequency encoding direction should be chosen is order to be aligned with the shaft of the needle [DSJ09]. The centerline misplacement was explained in [BPD+99] taking into consideration the altered magnetic field distribution that manifests in proximity of the instrument. Spins, spreading along the direction of the static magnetic field and close to the needle, precess at higher frequency, whereas spins spreading perpendicular show a slower precession frequency. Therefore, when a frequency encoding gradient is applied perpendicular to the needle shaft direction, the protons located close to the lowest gradient extremity precess even slower due to the magnetic field distortion. On the contrary, nuclei precessing at higher frequency are shifted in the opposite direction. Due to the interaction between these spins and the ones near to the needle, but laying on the perpendicular direction, the shift results greater on one side and minor on the other, causing also the displacement of the perceived centerline of the needle. The shift is also responsible for the intensity augment at the boundaries of the needle. These considerations confirm what was stated by Ladd et al. [LED+96] when they proposed a numerical model of the needle artifact based on the magnetic field generated by an infinite cylinder.

Lewin et al. [LDJ+96] put in evidence other three major needle artifact dependences: needle shaft orientation with respect to the external magnetic field, external magnetic field and pulse sequence applied. They investigated the artifact size arising from the usage of $\mathbf{B_0}$ at 0.2T and 1.5T. The widening of the needle shape visible in the image results increasing with the external magnetic field strength. The widening results also more pronounced when a gradient echo sequence is applied. The minor artifact was instead encountered when recurring to a spin echo sequence. A greater widening of the needle shape is to be expected when the needle is oriented perpendicular to the main magnetic field.

Mueller-Bierl et al. [MBGL+04] reported that the more the shaft of the instrument aligns with the $\mathbf{B_0}$ direction, the larger is the distance between the actual tip position and the end of the signal void visible in the image. This distance discrepancy decreases as the shaft is oriented perpendicularly to the magnetic field direction. This difference was reported to be less pronounced in case of surgical instruments were the ratio between the length of the needle shaft and the diameter of the tip was small. Their work suggests that attention needs to be paid when estimating the position of the needle tip from MR images during the procedure. Following, adopting the center of the artifact ball arising from the needle tip as an estimation

of the true position can be misleading.

In order to have a better understanding of the several effects induced by the various factors, a series of images were acquired. The acquisitions took place at Siemens MR, Erlangen, Germany, with a MAGNETOM Avanto system, 1.5T. The needle scanned was a cryoneedle 17Gauge, GALIL MEDICAL, Yokneam, Israel, immersed in a gelatin phantom and hold in place by a plexiglass holder designed by Eva Rothgang. All the sequence parameters were chosen in order to allow comparison between series of images where just one of the parameters was supposed to vary. At the end of the experiment two more biopsy needles (MReye$^{TM}$ DispChiba, COOKMedical, Bloomington (IN), USA) were placed inside the phantom and an additional series of images was acquired.

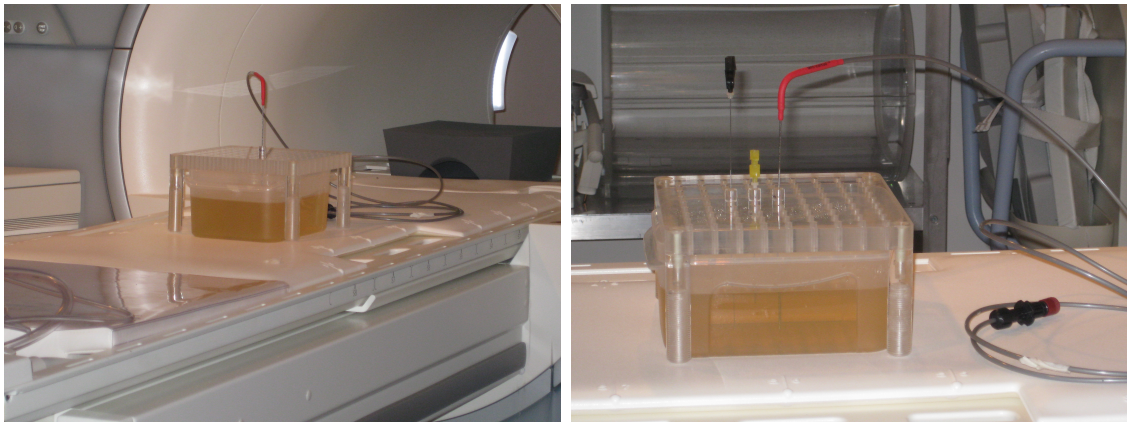

(a) Cryoneedle 17Gauge (b) Cryoneedle 17Gauge and Biopsy Needles

Fig. 5.3: Photographs of the experiment apparatus. All needles were immersed inside a gelatin phantom and hold in place vertically by a plexiglass holder. (a) The needle imaged was a cryoneedle 17Gauge, GALIL MEDICAL, Yokneam, Israel. (b) The additional needles on the left were two biopsy needles respectively 20Gaugex10cm long and 22Gaugex20cm long, MReye$^{TM}$, DispChiba, COOKMedical, Bloomington (IN), USA. Images were acquired during an experiment session of this work at Siemens MR, Erlangen, Germany, with Eva Rothgang.

In Fig. 5.4 the influence of needle shat orientation with respect to the main magnetic field $B_0$ is shown. Angle orientation of 90°, 75°, 45° and 30° were examined. Apparent needle widening becomes smaller the further the needle aligns with the direction of $B_0$. All the images represent a sagittal view of the needle and were acquired at the isocenter. As expected the size of apparent needle widening decreases as the shaft aligns to the direction of the static magnetic field.

The second parameter to be varied was the TE. TE of 5, 10, 15 and 25 ms were used. The result is illustrated in Fig. 5.5. The needle shaft widening is less pronounced with smaller TE and increases as the TE raises. A larger TE means a longer time window during which the protons gather a larger amount of dephasing thus inducing an emphasized marked area affected by signal loss. The effect mentioned explained also why the artifact results more pronounced when gradient echo sequences are used, since they are characterized by the absence of the rephasing pulse.

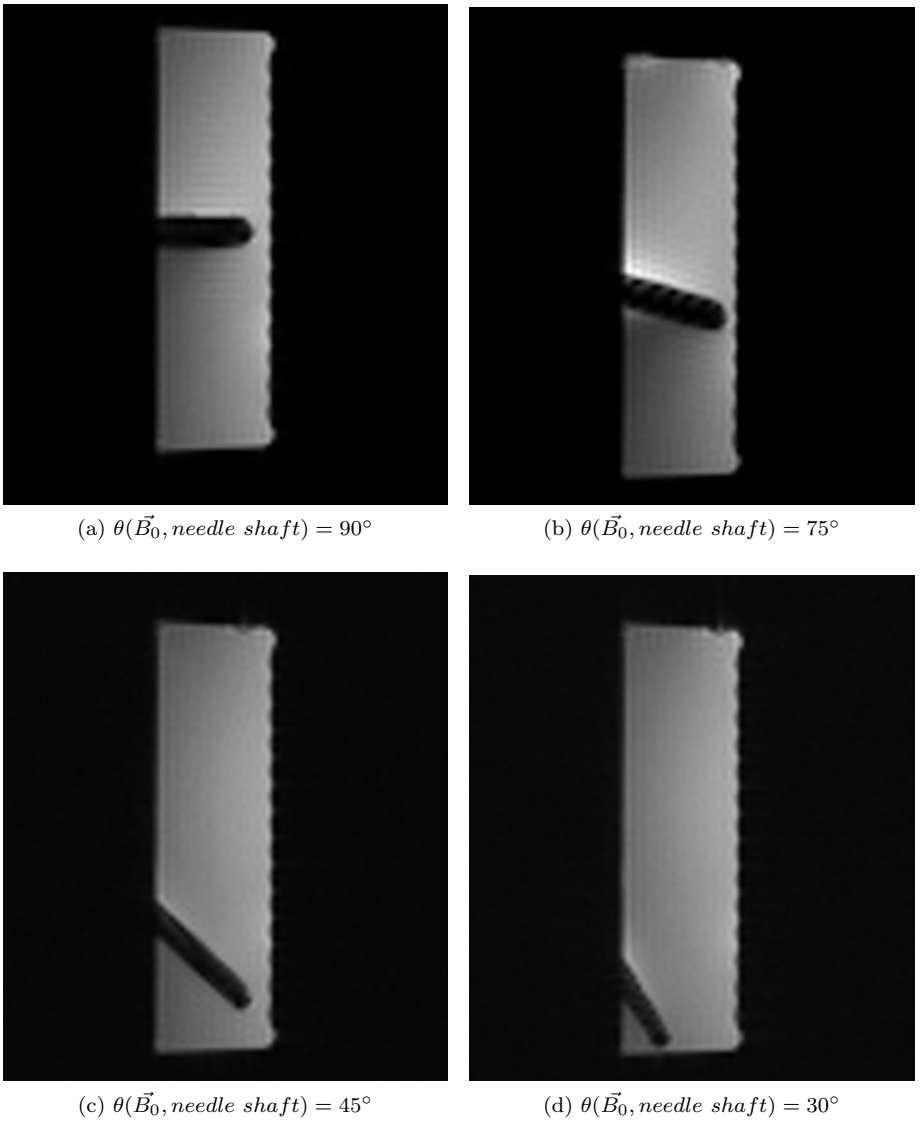

(a) $\theta(\vec{B_0}, needle\ shaft) = 90°$ (b) $\theta(\vec{B_0}, needle\ shaft) = 75°$

(c) $\theta(\vec{B_0}, needle\ shaft) = 45°$ (d) $\theta(\vec{B_0}, needle\ shaft) = 30°$

Fig. 5.4: MR images of a cryoneedle, 17Gauge, GALIL MEDICAL, Yokneam, Israel, acquired with needle shaft orientation w.r.t main magnetic field varying with a step of 15°. TE, 5.0 ms; TR, 51 ms; BW, 601 HzPxl$^{-1}$; Flip angle, 25°; Spacel resolution, 2.3x2.3x5mm. Images were acquired during an experiment session of this work at Siemens MR, Erlangen, Germany, with Eva Rothgang.

Using a larger bandwidth helps reducing the artifactual widening. As counter side effect, a larger bandwidth leads to a smaller Signal to Noise Ratio SNR [Sof11].

In Fig. 5.6 examples of acquisitions by means of trueFISP sequence with different bandwidths are shown. The images were taken using respectively a BW of 501 and 1002 HzPxl$^{-1}$.

The last acquisition performed aimed to allow a short comparison of the artifact appearance depending on needle shaft length and diameter (see Fig. 5.7a and Fig. 5.7b).

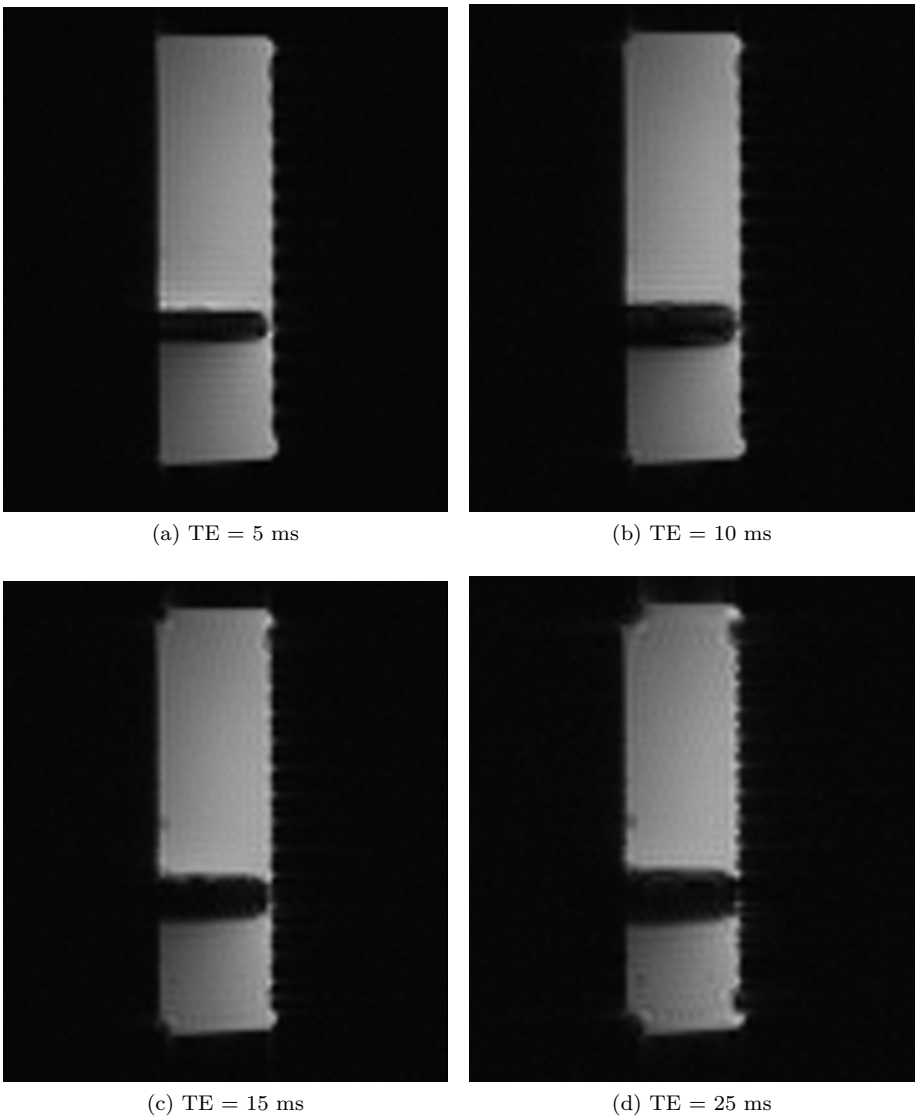

(a) TE = 5 ms (b) TE = 10 ms

(c) TE = 15 ms (d) TE = 25 ms

Fig. 5.5: MR images of a cryoneedle, 17Gauge, GALIL MEDICAL, Yokneam, Israel, acquired with needle shaft orientation orthogonal to the main magnetic field and TE respectively equals to TE, 5.0, 10.0, 15,0, 25.0 ms; The other parameters remained unchanged for all the series acquired. TR, 51 ms; BW, 601 $HzPxl^{-1}$; Flip angle, 25°; Spacel resolution, 2.3x2.3x5mm. Images were acquired during an experiment session of this work at Siemens MR, Erlangen, Germany, with Eva Rothgang.

In summary the major causes of artifacts are:

- ⋆ Magnetic field strength
- ⋆ Shaft orientation with respect to the static magnetic field $B_0$
- ⋆ Frequency encoding direction
- ⋆ Sequence used for the acquisition
- ⋆ Needle diameter

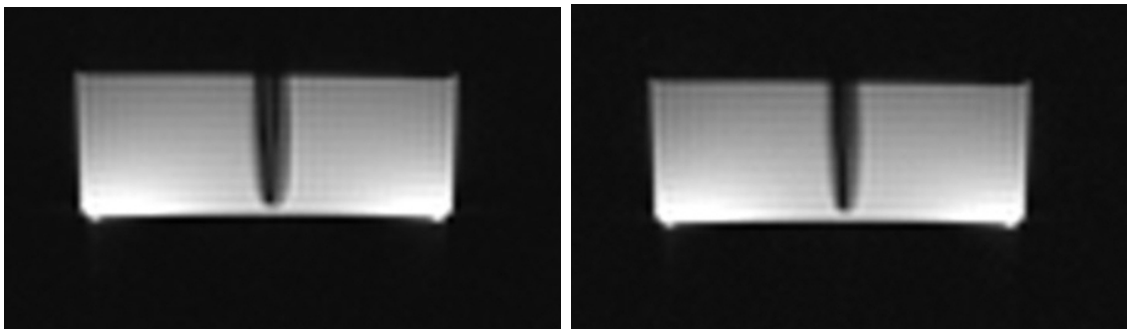

(a) BW: 500 HzPxl$^{-1}$ (b) BW: 1002 HzPxl$^{-1}$

Fig. 5.6: Transversal images acquired with trueFISP sequence. (a) The sequence parameters used were TE, 2.1 ms; TR, 545.5 ms; BW, 501 HzPxl$^{-1}$; Flip angle, 90°; Spacel resolution, 2.3x2.3x3.5mm. (b) TE, 1.6 ms; 417.4 ms, BW, 1002 ms; Flip angle, 90°; Spacel resolution, 2.3x2.3x3.5mm. Images were acquired during an experiment session of this work at Siemens MR, Erlangen, Germany, with Eva Rothgang.

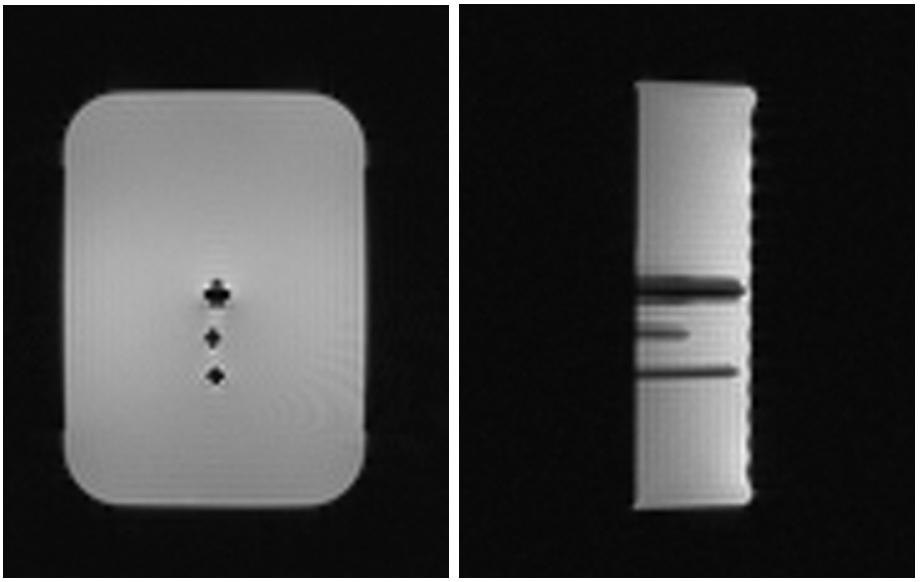

(a) (b)

Fig. 5.7: Images acquired with trueFisp sequence. The sequence parameters used were: TE, 1.52ms; TR, 398.24; BW, 1184$HzPxl^{-1}$; Flip angle 90°; Spacel resolution, 2.3x2.3x3.5mm. The needle imaged on the top was a cryoneedle 17Gauge, GALIL MEDICAL, Yokneam, Israel. The needles on the bottom were two biopsy needles respectively 20Gaugex10cm long and 22Gaugex20cm long, MReye$^{TM}$, DispChiba, COOKMedical, Bloomington (IN), USA. Images were acquired during an experiment session of this work at Siemens MR, Erlangen, Germany, with Eva Rothgang.

The choice of the sequence and its parameters is made depending on the specific target of the investigation. T1 weighted images provides the best anatomical definition, T2 weighted images and susceptibility weighted images are preferred when lesion detection needs to be performed. The capability to emphasize the visibility of the object under investigation represents mostly a term of power of the MR, but sometimes trying to keep all the parameters under control becomes a really challenging task.

Also when dealing with needle visualization a compromise needs to be made, depending on the specific case. It could be sometimes preferable to allow a wider artifact in order to gain SNR or to use a gradient echo sequence in order to make a thin needle visible MR images (see Fig. 5.8) as shown in [BPD+99]. In anycase, the aim is to make the needle depictable without eclipsing important structures in its proximity. A brief overview of methods developed in the literature dealing with needle visualization and localization problems is presented in the following section.

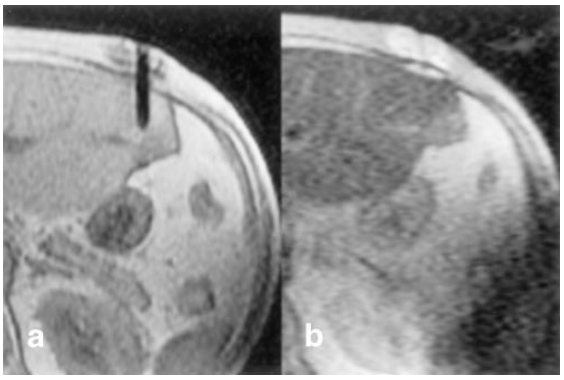


Fig. 5.8: a) Image of a liver acquired with GRE sequence. b) Same liver imaged with single-shot RARE. The figure aims to emphasize the subtle boundary of the needle visualization problem. The artifact needs to be reduced but still needs to be present in order to make the needle visible. The figure was published by Butts et al. in [BPD+99].

## 5.3 Techniques for Needle Localization

In the previous sections the relevance of selecting the best setup parameters in order to achieve a correct needle visualization was discussed. In order to improve the quality of the intervention it would be worth providing information about the instrument location or even about the needle tip position. This implies the necessity of developing methods able to detect the needle during the intervention and track its position over the time thus improving spatial accuracy of the positioning.

Felfoul et al. [FMBM07] pointed out that also in MRI, like in other imaging techniques, such as CT and Ultrasounds, tracking methods can be classified in three main groups: *passive*, *semi-active* and *active* tracking. What discriminates a class from the other is the amount of effort put in the use of further instrumentation, like guidewires and additional coils, in order to track the device. Several methods exploit marker systems [GPS+97] [SKD+03] [ZMG+06]. Projection techniques were also developed in order to increase the speed [SMO+98]. Some examples are described in the following.

Goede et al. [GPS+97] used a coaxial needle with receiver coils located at the needle tip and biplanar MR acquisitions in order to track the needle position during percutaneous cholecystostomy. Since the coils receive signal mainly from the

regions in their proximity, the position of the coils can be derived and further projected onto two orthogonal images used for device visualization. The tip position can be also superimposed on previously acquired images. Update of needle tip position can be performed every 120 milliseconds.

Additional microcoils were exploited also by Susil et al. [SKD+03]. A magnetic resonance guidance system for prostate interventions was investigated. In order to increase the accuracy of the needle insertion, a needle guide with three integrated microcoils is used. Localization of the coils can be performed every 60 milliseconds. From coils position, the residual translation and rotation required to reach the target structure can be calculated. Fast gradient echo imaging is used for visualization and image planes are updated in order to align with the needle direction. The overall time required for localization and scan direction update is between 0.7-2.0 frames per second.

Zimmermann et al. [ZMG+06] proposed a new variant of half Fourier acquisition single turbo spin echo sequence, HASTE. A robotic system is used to perform the needle insertion and receiver coils are added to act as active markers. Passive markers are also present at the needle holder. Passive and active markers allow to align the position in the gradient coordinate system with the robot coordinate system. The acquisition is limited around the region of the needle insertion and slice position is automatically updated with a time interval of 1 second, based on the position information derived from the needle detection. One slice is aligned parallel to the needle shaft and one is positioned orthogonal to the device, for a total of two slices used for fast guidance.

Schimizu et al. [SMO+98] exploited a projection reconstruction technique to track the tip needle position during biopsy procedures in an example of passive tracking of an MR compatible needle. The method allows update of the tip position with a time interval of 300 milliseconds. A radial fast spin echo sequence is exploited (rFSE). For the tracking, a high resolution reference image is acquired before the needle insertion starts. Further images are reconstructed using eight projections and are subtracted from the reference image. The difference is recognized as direct consequence of variations in the needle position. The tip was detected as the high intensity spot in the subtraction image and superimposed to the reference image in order to better visualize the needle position with respect to the surrounding tissues. Update of the reference image is required every 3.6 seconds to account for large movements that can occur.

Another example of passive tracking technique is provided by Kochavi et al. [KGA04]. The method is based on k-space analysis and parameters fitting. The needle is modeled as a rectangular object and five parameters are use for the characterization. The rectangle is represented as a 2D sinc in the frequency domain described by the same parameters. A high resolution image is acquired at the beginning of the procedure. For each successive acquisitions just 6 out of 128 k-lines are used. Image subtraction is applied with respect to the reference image and fitting of the 2D sinc function is performed. For each new image acquired,

the same set of central k-lines is acquired and the parameters calculated are used to describe the needle position. However, if the needle moves out of the planned plane, the reference image and the acquisition planes need to be updated.

Active tracking techniques require coordinate transformation in order to map the receiver coil position to the MR image space. Additional instrumentation is also required like microcoils installation, additional hardware and receiver channels for position calculation signal reception. Passive tracking techniques are based on simple image update, but fast imaging techniques need to be provided in order to guarantee a real time monitoring. Guidance performed by means of closed bore MR systems, like in [ZMG+06] and [SKD+03], benefits from a higher signal to noise ratio in comparison with methods based on an open configuration MR system.

# 6 Project Goal

As highlighted in Section 4 the effectiveness of the treatment by means of percutaneous minimally invasive procedures is highly dependent on the correct positioning of the device inside the region to be treated. Continuous monitoring by means of MRI is required in order to allow determination of the device position. Imaging slices could be automatically realigned and feedback about the current needle position could be give to the physician.

Following, the goal of this project is to develop algorithms for online needle detection to improve speed and accuracy of device positioning. The following sections explain how the detection could be integrated into the workflow of planning, targeting and treatment. Further, the chapter gives an overview of the framework used for this project (see Section 6.2).

## 6.1 Motivation for Real-time Needle Segmentation

The algorithms developed in this work aim to be integrated into the workflow for fully MRI-guided thermal ablations implemented in the interventional application Interactive Front End (IFE) [LKZ+05]. The proposed workflow is divided into the following steps (see Fig. 6.1):

**Planning** Definition of the needle insertion trajectory

**Targeting** Positioning of the device

**Treatment** Tumor ablation and temperature mapping

In the following, advantages of automatic needle detection integration are presented. Details about the Interactive Front End are provided in Section 6.2.

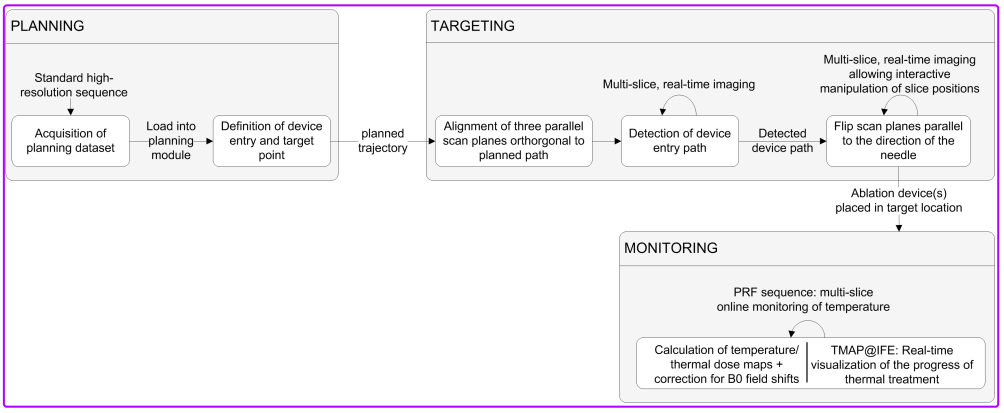


Fig. 6.1: Workflow of an ablation treatment as proposed in [RDW+11]. Figure used with permission [RDW+11]

### 6.1.1 Planning

During the planning step, the goal is to determine a safe insertion trajectory, that allows correct device positioning into the target volume with minimum risk of vessels and organs injury and highest rate of tissue and organ preservation.

A highly resolved dataset is usually acquired for planning of the device trajectory. The application Planning@IFE [RDW+11] allows the physician to define the entry and target points and provides multiple features for reviewing the planned path.

When the device insertion starts, the entry point position is updated by automatic detection of the cros sectional needle artifact [RDW+11] (see Fig. 6.9a). Target and update entry points are used as prior information for the needle segmentation, helping to reduce the area where the needle is most likely to be. If the entry and target points change, new inputs are provided to the needle detection application.

### 6.1.2 Targeting and Rational for Automatic Needle Detection

Once the trajectory is defined, the physician can proceed with the device insertion. Real time 2D images are continuously acquired and sent to the Interactive Front End. Orientation of the slice acquisition can be manipulated in real time from the Interactive Front End. The information concerning the new scan plane is sent to the MR scanner and slices along the new position are acquired. A schematic representation of the communication between IFE and the MR scanner is depicted in Fig. 6.2.

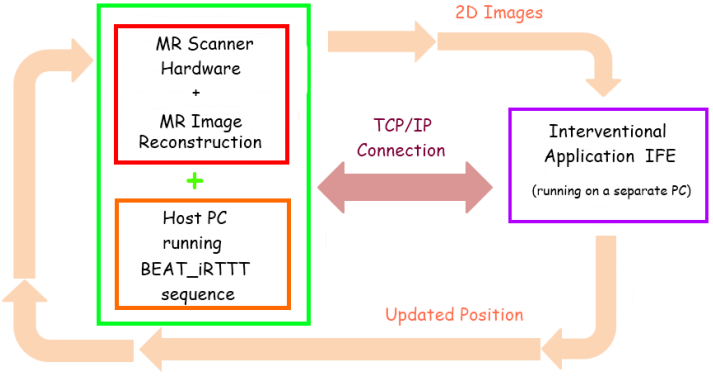


Fig. 6.2: Simplified schema of the communication network between the MR scanner and the IFE is depicted. The host PC and the computer running the IFE application are located in the console room beside the scanner room.

Real time slice manipulation offers great flexibility. During the insertion, slight movements of the device could impair its visibility in the current images. The position of the slice can be manually corrected, in order to restore the intersection between the scan plane and the device. However, manual positioning of the slices

can be challenging, meanwhile leaving the physician without visual inspection of the current needle location.

Previous considerations encouraged for further automation in the Targeting@IFE module [RDW+11]. After the skin penetration is performed, the needle is advanced deeper towards the mass to be treated. Once the entry path of the device is detected in scans aligned orthogonal to the planned path and parallel to each other (see Fig. 6.3a), the scans are flipped along to the needle direction (see Fig. 6.3b) [RDW+11] .

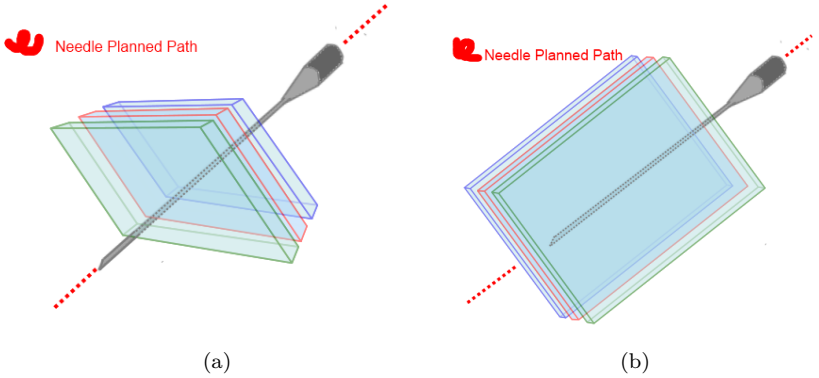


Fig. 6.3: (a): slice alignment orthogonal to the needle planned path. This represent the first step of the targeting module (see Fig. 6.1). (b): after the entry path of the device is detected, slices are flipped parallel to the planned path. Relative parallelism of the three slices in (b) and proportions between needle and slices dimension are merely for illustration purposes.

Images acquired during the targeting step define the second important input to the needle detection application. After the slices are flipped along the direction of the planned path, as a consequence of the image orientation, needle artifacts are expected to be visible in the images (see first image in Fig 6.9a). The goal of this work is the detection of a long and straight structure.

If the insertion direction deviates from the planned path, the needle could be not visible in one or more of the three slices acquired. An example is shown in Fig. 6.4. The needle results clearly visible in the axial slice but absent in the sagittal view. Detection of the device in the axial image could allow automatic realignment of the sagittal scan plane, reducing the *blind gap* during which no needle is visible. If the needle is visible in none of the images, the operator needs to have the full control on the slice positioning back.

To provide automatic slice realignment the distance of the detected centerline from the planned entry point and the angle deviation of the centerline from the planned path need to be provided. From the translation and orientation informations, the transformation matrix for the slice translation and rotation can be derived.

Further, the offset information could be displayed on the Interactive Front End to help the physician to follow the predefined trajectory. Provided with this information and supported by continuous imaging, the physician could adjust the

positioning of the needle. Further, it anticipates that the surgeon could operate more confident and fast, having a better notion of the direction he is moving. Moreover, automatic detection would help to identify the deviation from the desired path sooner: small deviation angles could be recognized from the physician just when the device is already deeply inserted. In such situation, it could be necessary to extract and insert again the device in order to position the needle correctly. A lot of time could also be saved if multiple insertions could be avoided, thus speeding up the positioning step. Distance and angle deviation need thus also to be returned as outputs of the needle detection application [Dis].

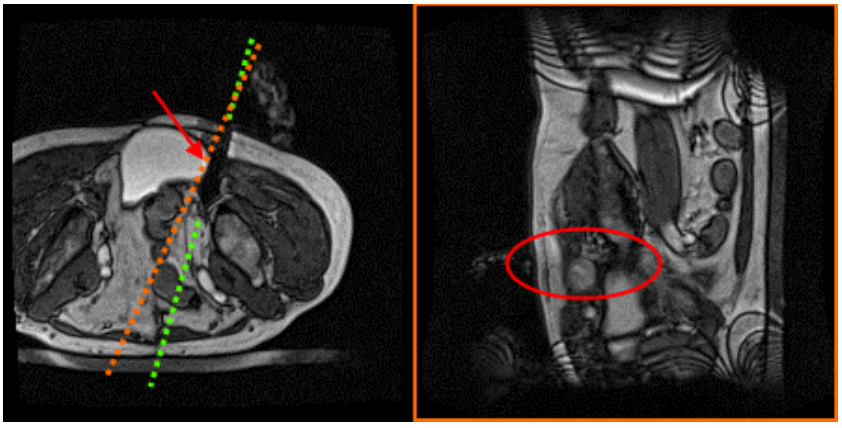

Fig. 6.4: Illustration of the slice realignment problem. The first image represents an axial acquisition where the needle is clearly visible. The red arrow indicates its position. The second image refers to the sagittal scan performed immediately after. The red ellipse indicates the area where the needle should be. Since the slice is off w.r.t the needle axis, the needle is not visible. The dotted orange line on the axial view indicates the relative scan direction of the sagittal image. The dotted green line shows the correct scan direction. The direction could be derived after the needle detection.

The algorithm should also be as much as possible independent from the needle diameter. This would make the application more flexible and could allow its usage independently from the type of needle employed during the procedure.

Moreover, the needle detection should be also independent from its orientation with respect to the the image coordinates system. Detection should be provided with good accuracy whether the needle is oriented parallel to one of the system coordinate axis or directed along an arbitrary direction through the image.

The entry and target points are provided in world coordinates, relative to the patient centered coordinate system in physical space. The points are therefore identified by 3D coordinates in space. Although slice acquisitions are supposed to take place as closest as possible to the planned path, it is likely to happen that the entry and target points do not lie on the plane of the 2D image in input. Before further processing could be performed, the algorithm should therefore be able to exploit the position information provided by 3D points in space, translating it in meaningful information in the plane of the current image.

In Fig. 6.5 the interaction of the needle detection application with the Treatment Workflow@IFE [RDW+11] is summarized.

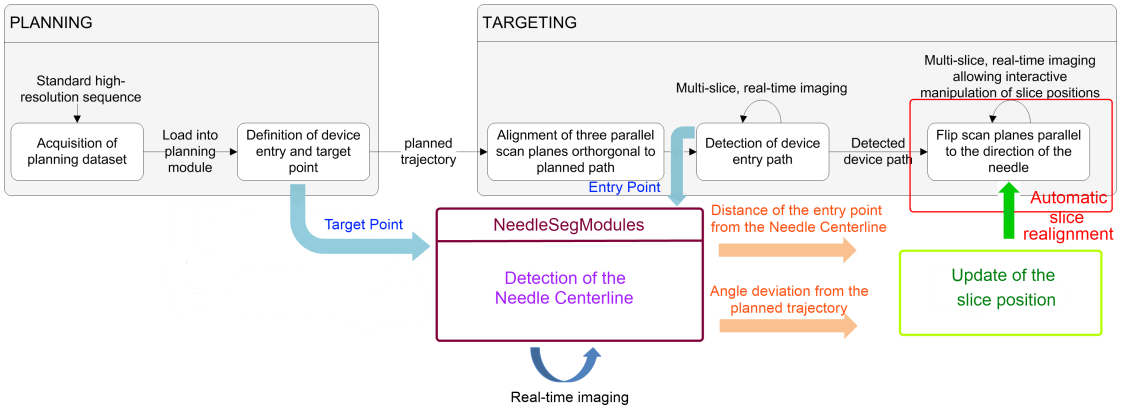


Fig. 6.5: Location of the needle segmentation application w.r.t the Treatment Workflow@IFE [RDW+11] is shown. The entry and target points are provided respectively by the Planning@IFE and Targeting@IFE modules. Real time images comes from the MR Image Reconstruction. Deviation information from the planned trajectory are provided to the Targeting@IFE module allowing the update of the scan planes. Figure adapted with courtesy of Eva Rothgang [RDW+11].

### 6.1.3 Treatment

Just when the device is properly positioned inside the target volume, treatment can take place. During this phase, temporal and spatial temperature mapping is performed, monitoring the development of the ablated region.

Visualization of the progress of the thermal treatment is carried out by means of a thermal guidance application TMAP@IFE [EDS+11][RELC10]. Temperature is measured using a multiplanar PRF gradient echo sequence.

Successful and precise targeting step is one of the first requirement for complete tumor treatment.

## 6.2 Project Framework

The Interactive Front End (IFE) [LKZ+05] is a user interface developed by Siemens Corporate Research, Baltimore (MD) USA, for guiding interventional procedures under MR imaging. It adds capabilities that the standard scanner user interface does not provide, like interactive and real-time control of scan planes and direct parameter manipulation such as acquisition schemes and phase encoding direction.

As mentioned in the previous sections, automatic needle detection would add further functionalities like the automatic slice realignment and the offset indication from the planned trajectory .

IFE runs on an independent PC connected to the standard scanner network via socket connection. The communication is established through an TCP/ICP protocol 6.2.

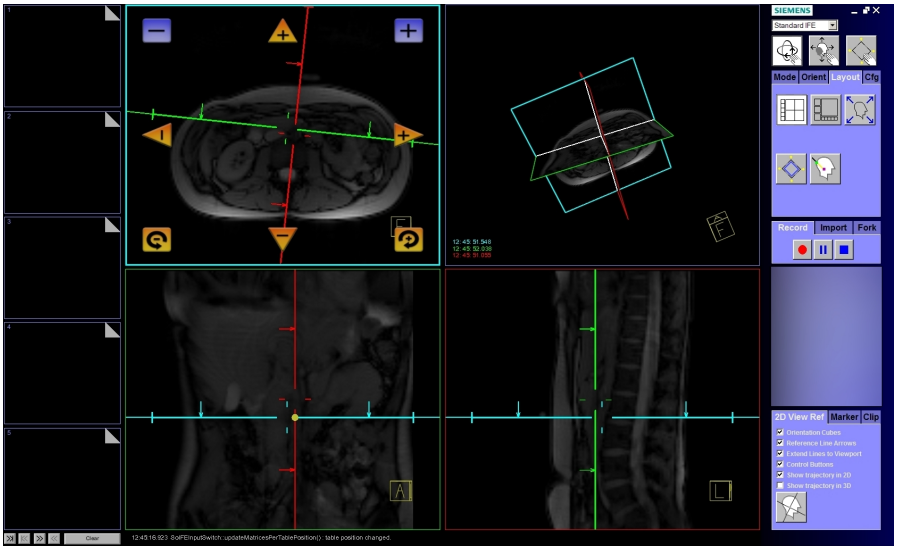


Fig. 6.6: Screenshot of the standard interactive front end. Figure used with permission by SCR, Baltimore (MD), USA

Visualization update in real-time allow a dynamic interaction between operators at the work station and the physician. Acquired images are displayed in real-time both on the IFE PC in the control room and on an in-room monitor. The physician is watching the real-time images on the screen while the operator adjust the slice position. To give maximum flexibility to the physician, the monitor is usually placed on a movable cart.

Fig.6.6 shows the IFE user interface. The main central view is dedicated to real-time image visualization. Several options for image rendering, such as indications of the relative slice orientations, as well as slice manipulation facilities are provided.

During Targeting@IFE [RDW+11], the BEAT Interactive Real Time Tip Tracking (BEAT_IRTTT, Siemens) sequence is used. BEAT_IRTTT was developed to run with IFE [RCB+09]. It allows to switch between a normal gradient echo (GRE) to a steady-state free precession sequence, the so called trueFISP or TRUFI sequence. The latter in particular benefits from speed and high SNR [RCB+09]. Details about the trueFISP sequence can be found in Section 6.4.

Images acquired with the BEAT_IRTTT are the 2D real time images in input to the needle detection application.

## 6.3 eXtensible Imaging Platform

The Interactive Front End is built on the top of the eXtensible Imaging Platform (XIP) [RDW+11]. XIP represents an open source framework, that includes a variety of tools for image processing and visualization.

XIP is wrapper for some libraries extensively used in clinical softwares like:

**ITK** Medical image processing

**VTK** Image visualization

**DCMTK** DICOM data manipulation

Its implementation is based on OpenInventor and OpenGL, with C++, Java and Javascript binding [LKZ+05]. OpenInventor and OpenGL contribute respectively to the scene graph construction and to the rendering mode (see Fig.6.7). Prototypes can be built using the modules available in the scene objects pool.

A module is classified as belonging to one of the following category:

**Nodes** A node allows visualization by rendering geometries, properties or their combinations.

**Engines** An engine performs an action. The connection of engines defines the processing pipeline.

Each module performs a specific action and is instantiated just dragging it into the scene graph window. Inputs, outputs and parameters of the single module can be accessed opening the *fields* window.

Favorite modules, recurrent scene graph patterns and scene graphs themselves can be saved in the corresponding category, available to a subsequent usage (see Fig 6.7).

Multiple modules can be connected together in order to perform a more complex task. Connections are established through the fields of different modules. The overall object aggregation is referred to as *scene graph*. The set of modules can be extended by custom nodes and engines implemented in C++ thus increasing the functionalities of the standard XIP.

The scene graph can be stored in a kxf file with file ending *.xip. The latter allows to store also informations about object disposition and field connections, speeding up follwing usage.

The processing pipeline can be fragmented exploiting a *separator* instance. This functionality is also inherited from OpenInventor. Separators form a group of nodes and separate their effects from the rest of the scene. Performing a rendering action on a separator induces the execution just of the scene graph constructed under it. In a hierarchical manner, an action performed on a parent separator activates the execution of all its children. An example of an XIP scene graph is provided in Fig.6.7.

The algorithms presented in this work were also implemented using XIP. New modules were developed and scenegraphs were built in order to allow fast needle

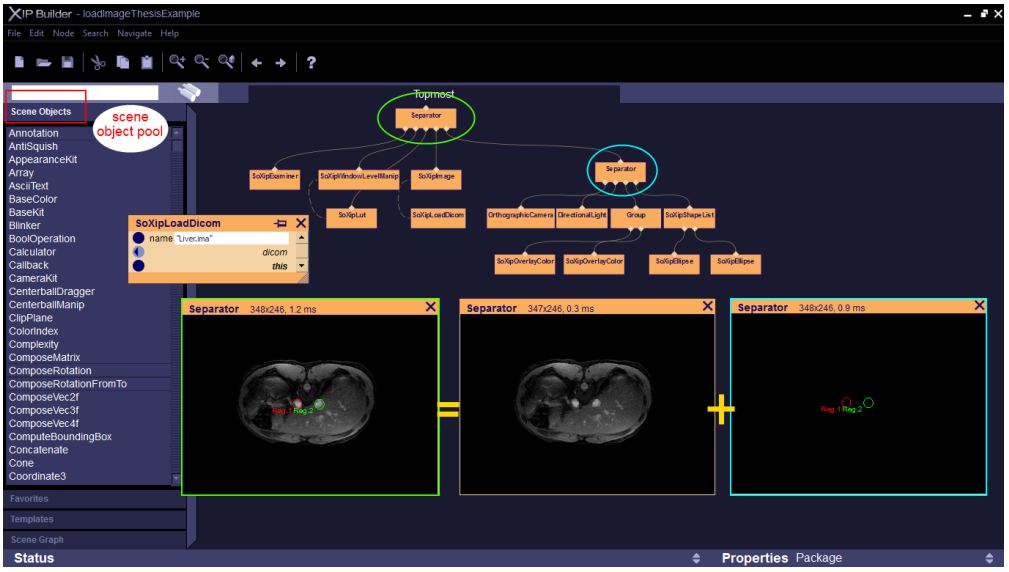


Fig. 6.7: Screenshot of the XIP interface. The scenegraph built in this example is composed by two groups of objects, gathered together by two separators. The first group loads a dicom image and sets the visualization properties. The second defines elliptical shapes at specific positions in space, each characterized by a specific color. A render action performed on the uppermost separator combines the actions of the two groups, overlaying the ellipses to the dicom image. The example is adapted from the overlay tutorial provided on the xipwiki website [(ED07].

detection, providing the *NeedleSegModules* library. The *NeedleSegModules* library contains 12 modules and a complete scene graph for the needle detection is made up of about 34 modules. The name of each module developed starts with the identifier *SoNSeg*, referring to the NeedleSegModules library. All the modules were implemented keeping in mind that the needle detection is supposed to be integrated in the IFE, receiving inputs from the planning and targeting steps of the treatment and running during the device insertion.

## 6.4 TrueFISP Sequence

As mentioned, trueFISP sequence belongs to the gradient echo family (GRE). GRE is usually employed when speed is one of the first requirement: small flip angles ($\alpha < 90°$) yield to a shorter TR and hence reduction of the scan time. However, since a flip angle smaller than 90° means an incomplete flipping of the longitudinal magnetization into the transverse plane, the decay of the signal occurs more rapidly. In order to have the time to apply the phase encoding gradient $G_{PE}$ and still maintain an adequate amount of signal to be recorded, a refocusing gradient is usually applied along the chosen read-out direction. This gradient is characterized by a negative lobe, that dephases the spins, followed by a positive lobe, lasting twice the time and with double area subtended (See Fig. 6.8a). At the mid point of this second lobe the signal is measured [MMG03].

Normally, a repetition time TR too small leads to a small transverse magnetization

during subsequent excitations, and hence less signal, affecting the achievable SNR. TrueFISP sequence allows a high SNR, while ensuring speed at the same time, recurring to balanced rewinding gradients in all three directions. Usage of balanced gradient ensures a null total gradient moment within each TR [CSB+01]. The timing diagram is depicted in Fig.6.8.

The overall effect is to report the spins to the phase value present before any excitation pulse was applied, maintaining a coherent transverse magnetization: in other words it maintains the steady-state. The signal recorded contains contributions from both the transverse magnetization and the FID induced by the RF pulse applied [MMG03]. A higher SNR can hence be achieved and the signal results less dependent from body motion. In addition the contrast depends upon the ratio of T2 and T1 [HWTM90].

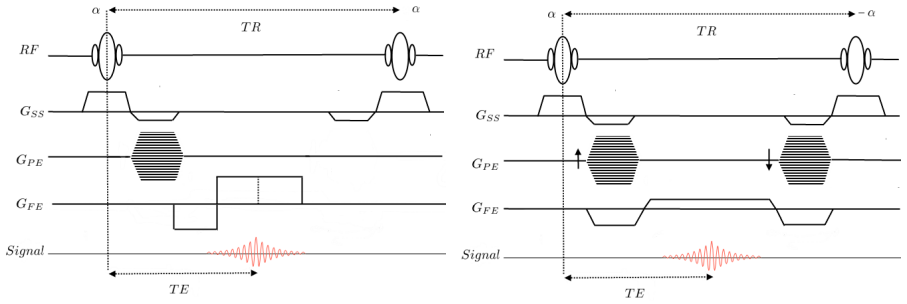


(a) (b)

Fig. 6.8: Timing diagram of a GRE sequence is depicted. A flip angle $\alpha < 90°$ is used and a bi-lobed gradient is applied along the read-out direction to recall the FID at time TE. (b) depicts the timing diagram of a TrueFISP sequence. Rewinding gradients along all axes maintain the steady-state of the magnetization. Figures adapted from [MMG03] Fig.12.28.

TrueFISP sequences are relative high sensitive to field inhomogeneities. If some spins are not perfectly resonant, some residual dephasing can still be present and oscillate between one excitation and the other, producing stripes running through the scanned sample (see Fig.6.9a). This characteristic artifact can be reduced using a very short TE and recurring to shimming [MMG03]. Consecutive RF pulse excitations with alternating polarity ($\alpha/-\alpha$) can also be used to reduce the influence of magnet inhomogeneities [CSB+01].

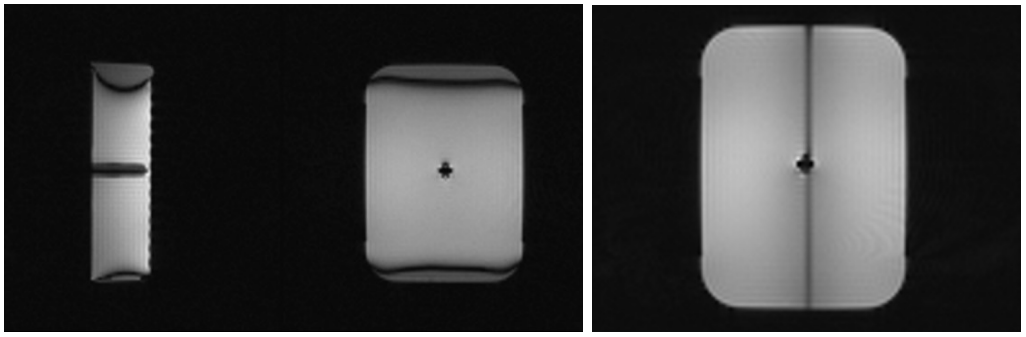

(a) (b)

Fig. 6.9: A cryoneedle (17G, GALIL MEDICAL), Yokneam, Israel inserted into a gelatin phantom was scanned. Fig.6.9a shows typical trueFISP artifacts. Respectively coronal and sagittal view. Sequence parameters: TR, 417.4ms, TE, 1.6ms, BW, 1002HzPxl$^{-1}$; FoV, 300x300; matrix size 128x128. (b) The signal void left after the first excitations is illustrated. Sequence parameters: TR, 398.24ms, TE, 1.52ms, BW, 1200HzPxl$^{-1}$; FoV, 300x300; matrix size 128x128. Images were acquired during an experiment session of this work at Siemens MR, Erlangen, Germany, with Eva Rothgang. The scanner used for the experiment was a MAGNETOM Avanto 1.5T.

# 7 Needle Detection Algorithm Implementation

Section 6 explained how automatic needle detection could improve the performance of interventional guidance. Based on the observations reported in Chapter 5 and the prior information available about the planned path provided by the planning module (see Section 6.1.1), the following assumptions were made:

**Hyp.I** :The needle is a rigid body, no deformation component is considered.

**Hyp.II** :The needle appears as one of the darkest features in the image.

**Hyp.III** :The planned insertion path is known.

**Hyp.IV** :The entry point is considered fixed in space and time.

## 7.1 Preprocessing

As discussed in Section 5, needle appearance in an MR image is determined by its susceptibility properties, which produce a signal void. However, MR images can be affected by noise. In order to satisfy Hyp.II, a preprocessing step is performed.

The MR image is considered as composed of two components: background and foreground. The needle is regarded as belonging to the background, whereas the foreground is defined as the whole patient anatomy. Normalized histograms of available data sets are calculated. Based on their appearance, global thresholding techniques were reviewed in order to identify an algorithm which could provide an optimal threshold $T$ used to separate the background from the foreground, thus producing a more homogeneous needle artifact. The threshold is therefore exploited to perform the following transformation $G(f(x,y))$:

$$g(x,y) = \begin{cases} 0, & \text{if } f(x,y) < T \\ f(x,y), & \text{otherwise} \end{cases}$$

where

$$\begin{aligned} f(x,y) &: \textit{pixel intensity at position (x,y),} \\ g(x,y) &: \textit{new pixel intensity at position (x,y),} \\ T &: \textit{calculated global threshold.} \end{aligned}$$

In Fig. 7.1 an example of a normalized histogram and optimal thresholds calculated recurring to different methods are depicted. Algorithms proposed respectively by Otsu [Ots75], Kittler [KI86] and Li [LL93] were considered.

The optimal $T$, obtained with the method of the minimum error proposed by Kittler, provided in general the best performance in terms of noise removal inside the needle and preservation of the surrounding foreground structures (see i.g Fig.

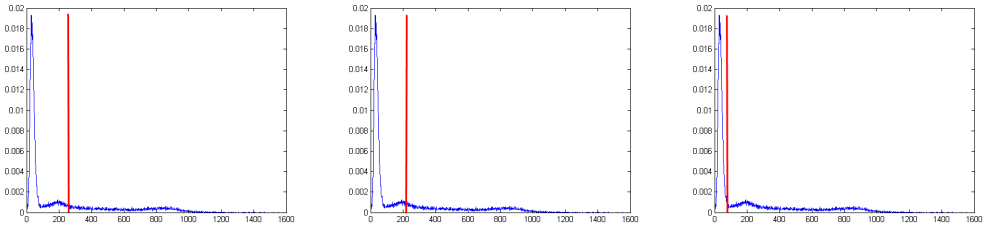

(a) T = 257 (b) T = 224 (c) T = 75

Fig. 7.1: Normalized histograms of the image depicted in Fig. 7.2a overlayed with the value of the optimal threshold $T$ calculated recurring respectively to Otsu [Ots75] (a), Kittler [KI86] (b) and Li [LL93] (c) algorithms.

7.2a and Fig. 7.2b). This algorithm was therefore adopted. However, application of the proposed preprocessing step is impaired when images in the data set are affected by striping artifact, as shown in Fig. 7.2c. The minimum error algorithm assumes the presence of two normally distributed components in the image, the mentioned foreground and background. The striping artifact mines this hypothesis since most of the gray levels are common also to the foreground. As a consequence, the calculated $T$ results too high. Performing $G(f(x, y))$ would set the greatest part of the image to zero, leading to the needle disappearance.

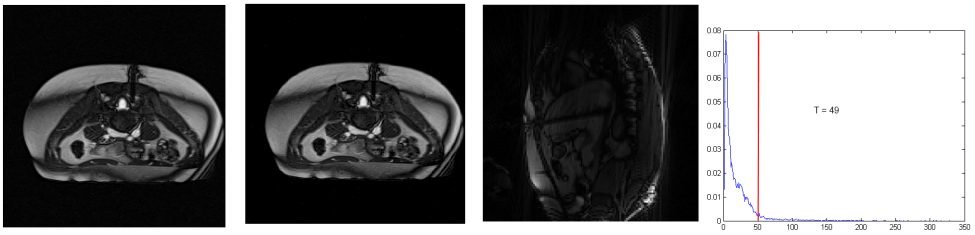


(a) (b) (c)

Fig. 7.2: In (a) and (b) original image and result of successful thresholding are shown. (c) The preprocessing step fails when the image is affected by striping artifact, since no distinct grey level separation occurs between background and foreground.

Preprocessing is performed by the **SoNSegThresholdMinError** engine. The input is a DICOM image wrapped in a SoXipSFDataImage object, after it was loaded into the scenegraph by a SoXipLoadDicom engine. The output is represented by the SoXipSFDataImage obtained applying $G(f(x, y))$.

## 7.2 Region Crop

The information provided by the planning step and incorporated in Hyp.III is used to restrict the image area to be processed. Due to the multiplanar imaging capabilities of MRI, the plane of the image received as input could be oriented along each direction in space. However, since the physician is supposed to follow

the planned path, acquisitions are likely to be performed in a limited region around the planned trajectory.

Following, the 3D coordinates of the entry and target points can be used to approximate the planned trajectory on the scanned image. In the **SoNSegCropConeEngineWrld** module, the 3D coordinates are orthogonally projected onto the plane of input image defining the points $E_{Prj} \in R^3$ and $T_{Prj} \in R^3$, still in world coordinates, and therefore a trajectory onto the image plane. The corresponding image indeces, $E_{Im}$ and $T_{Im}$, are calculated.

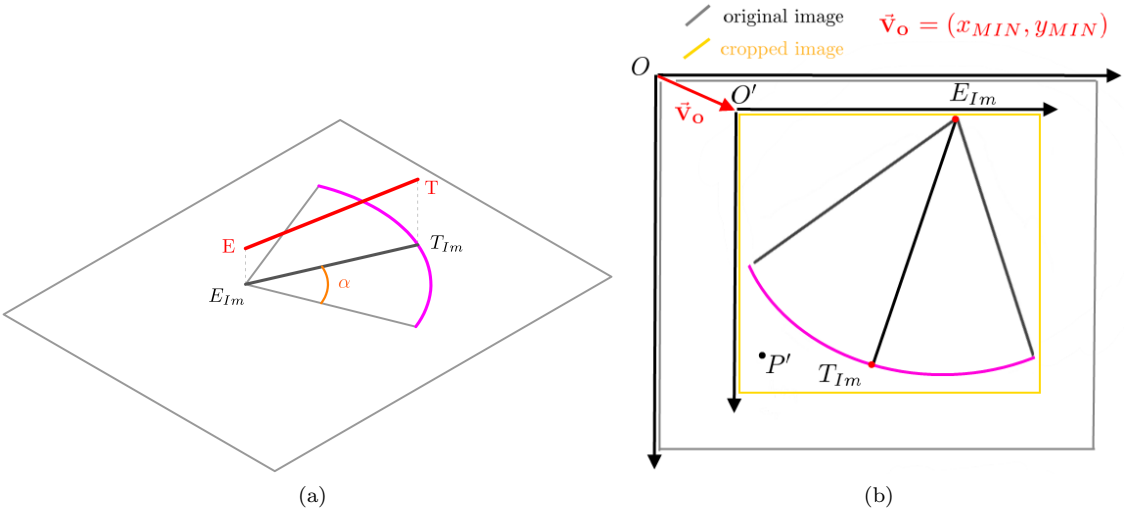


(a) (b)

Fig. 7.3: Projection of the entry point $E$ and target point $T$ onto the image plane is depicted in (a). The construction of the circular sector from the projected planned trajectory is also illustrated. (b) shows the minimum bounding enclosing the circular sector and the crop of the image. The indeces of a point in the cropped image are related to the indeces of the correspondent point in the original image through the translation vector $\vec{\mathbf{v}}_\mathbf{o}$.

Based on the projected trajectory, an angle $\alpha$, that represents half of the aperture of a circular sector having $E_{Im}$ as vertex and the distance $d(E_{Im}, T_{Im})$ as ray, is defined. The value $d$ corresponds to the length of the projection of the planned path in the image plane. Since the needle entry point is considered fixed (Hyp.IV), the needle can be considered as anchored to this point. Needle movements in a plane can be therefore described as rotation around an axis perpendicular to the plane and passing through the entry point. The default value assumed in this work for $\alpha$ is 45°. Defining $A$ and $B$ as the extreme points of the sector, the following point set can be defined:

$$S = \{(x, y) | (x - x_P)^2 + (y - y_P)^2 = R^2, x_B \leq x \leq x_A, y_A \leq y \leq y_B\} \cup \{E_{Im}\}$$

where

$$\begin{aligned} E_{Im} &= (x_P, y_P), \\ A &= (x_A, y_A), \\ B &= (x_B, y_B), \\ R &= d(E_{Im}, T_{Im}). \end{aligned}$$

Given $S$, the minimum bounding box including the circular sector can be calculated and used to crop the image. In Table 1, the input and output fields of the SoNSegCropEngineWrld module are reported. The new origin of the image is the pixel $O' = (x_{MIN}, y_{MIN})$ of the bounding box and its image indeces are important to be able to calculate a pixel position in the original image. The correspondent point $P$ in the original image of a point $P'$ in the cropped image can be obtained as follow:

$$P = P' + \vec{\mathbf{V}}_{\mathbf{O}} \tag{7.1}$$

where

$$\begin{aligned} P'(x', y') &: \textit{point in the cropped image,} \\ P(x, y) &: \textit{correspondent point in the original image,} \\ \vec{\mathbf{V}}_{\mathbf{O}} &: \textit{translation vector whose components equal the} \\ &\quad \textit{indeces of the new origin.} \end{aligned}$$

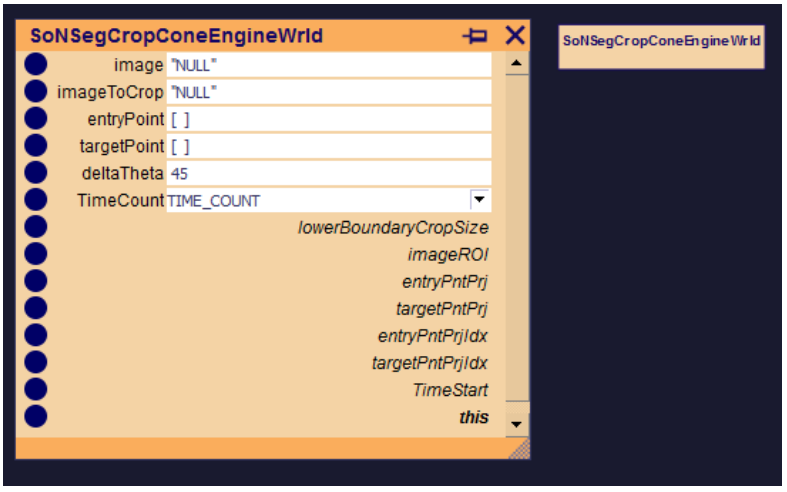


Fig. 7.4: Screenshot of the SoNSegCropConeEngineWrld module

Table 1: Input and Output Fields of the SoNSegCropEngineWrld (SoEngine)

| **SoNSegCropEngineWrld (SoEngine)** | | |
|---|---|---|
| **Input Field** | **Field Type** | **Description** |
| image | SoXipSFDataImage | Input image coming from a SoXipLoadDicom engine. The pixel type is supposed to be unsigned short |
| imageToCrop | SoItkSFDataImage | Input image converted to an ITK image object |
| entryPoint | SoMFVec3f | 3D coordinates of the needle entry point |
| targetPoint | SoMFVec3f | 3D coordinates of the needle target point |
| deltaTheta | SoSFFloat | Half of the aperture angle of the circular sector having as a vertex the projection of the entry point onto the image plane (45°) |
| **Output Name** | **Field Type** | **Description** |
| lowerBoundaryCropSize | SoMFInt32 | Image indeces of the new origin of the image |
| imageROI | SoItkSFDataImage | Cropped image, ITK object |
| entryPntPrj | SoMFVec3f | 3D coordinates of the needle entry point projected onto the image plane |
| targetPntPrj | SoMFVec3f | 3D coordinates of the needle target point projected onto the image plane |
| entryPntPrjIdx | SoMFInt32 | Image indeces of the needle target projection point in the original image |
| targetPntPrjIdx | SoMFInt32 | Image indeces of the needle target projection point in the original image |
| TimeCount | SoSFEnum | Drop-down menu that allows to decide if the startig time of the processing has to be registered (TIME_COUNT) |

## 7.3 Edge Detection

One of the first steps exploiting Hyp.I, is to run an edge detection algorithm. It was decided to employ the Canny algorithm [Can87], considered the better performance usually achievable in comparison with the algorithms exploiting the Roberts [Rob63], Sobel [SF68] and Prewitt [Pre70] operators. The **SoNSegCannyITK** module was implemented trying to make the algorithm as independent as possible from any user based decision of the parameters.

As described in the paper, the algorithm includes mainly two steps: the detection of the edges and their tracking. The first one results from the composition of a Gaussian smoothing and a derivative operation.

$$G(\cdot) \circ \nabla(\cdot)$$

where

$$G = e^{-\frac{x^2+y^2}{2\sigma}},$$
$$\nabla = (\frac{\partial(\cdot)}{\partial x}, \frac{\partial(\cdot)}{\partial y}).$$

The magnitude of the gradient applied to an image convolved with a Gaussian kernel is used to approximate the *edge strength* of a point. In absence of noise, the derivatives should reach a maximum value along the direction normal to the edge, that is $\vec{n}$. The Gaussian reduces the influence of the noise. A symmetric Gaussian kernel is normally used. Directional kernel were proved to provide better performances, but require good knowledge of the direction to be investigated [Can87].

The second step in the Canny algorithm involves the identification of the points, having the highest probability to belong to an edge, and the tracking of the edge. The identification is done by hysteresis thresholding, implying the use of two thresholds. Points above the highest threshold are marked as truly belonging to a contour: starting from them, all the points higher than the lowest threshold and forming a connected component are also regarded as belonging to a contour. The rest of the points is disregarded [Can87].

The SoNSegCannyITK is build on top of the *cvCanny* function available in the open library OpenCV. Some modifications were made, with the goal to make it as independent as possible from user parameter selection. Gaussian smoothing needed also to be added, since it is not included in the *cvCanny* implementation.

In order to apply the Gaussian smoothing, information about the standard deviation $\sigma$ of the noise present in the image needs to be provided. The standard deviation represents the only parameter required as input by the SoNSegCannyITK module. An estimation of $\sigma$ can be provided calculating the standard deviation of a background region.

As concerning the hysteresis step, the SoNSegCannyITK provides the two necessary thresholds, recurring to the histogram of the values in output from the Gaussian-derivative step. In [Can87], it was pointed out how percentiles lower then 80 % could be regarded mainly as noise contributions. Adopting the 80% percentile as highest threshold $T_H$ and $0.4T_H$ as the lowest threshold $T_L$ was seen to provide good performance.

A screenshot of the SoNSegCannyITK module is shown in Fig. 7.5. The output and input fields of the module are reported in Table 2.

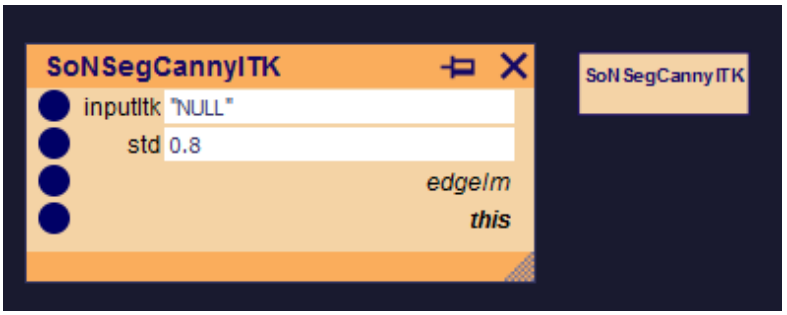


Fig. 7.5: Screenshot of the SoNSegCannyITK module

Table 2: Input and Output Fields of the SoNSegCannyITK (SoEngine)

| **SoNSegCannyITK (SoEngine)** | | |
|---|---|---|
| **Input Field** | **Field Type** | **Description** |
| inputItk | SoItkSFDataImage | Input image converted to an ITK image object. The pixel type is supposed to be unsigned short |
| std | SoSFFloat | Standard deviation of the Gaussian smoothing used to perform the Canny edge detection (0.8) |
| **Output Name** | **Field Type** | **Description** |
| edgeIm | SoItkSFDataImage | Edge image in output. The image is an ITK object |

## 7.4 Identification of Needle Contours

Once the edge image is available, the task is to identify the edges belonging to the needle contour. In this work, two algorithms are proposed for needle contour detection and are presented in the following sections. The needle centerline is the output of both the proposed algorithms.

### 7.4.1 Hough Transform

The first algorithm implemented in order to identify the needle contours is based on the Hough transform, that is widely employed in literature thanks to its capabilities to extract lines from images [KSG98]. Hough transform was also recently applied in a real-time biopsy needle segmentation [DF03] exploiting the concept of Look Up Table, LUT, to improve speed. The same approach was used in this work to implement an algorithm for needle contours detection.

Kamat et al. [KSG98] recurred to the Hough transform formulation proposed by Duda et Hart [DH72]. The latter assumes a polar line parametrization:

$$\rho = x\cos\theta + y\sin\theta \tag{7.2}$$

where

$\rho$ : *distance of the line from the image origin*,
$\theta$ : *angle formed by the normal to the line with the* $x$ *axis.*

The ranges of values usually assumed for $\theta$ and $\rho$ are respectively $[0, \pi]$ and $[-d, d]$ where $d$ is the diagonal of the image under investigation. In the image space, a line is identified by the indeces, $(x_1, y_1)$ and $(x_2, y_2)$, of a couple of points. In the *parameter space*, a line is instead identified by the couple $(\rho, \theta)$. Since the indeces of the points belonging to some contours present in the image are known, they can be used to derive the parameters $\rho$ and $\theta$. Using the polar formulation, an *accumulator array* in the parameter space is calculated from the available image. The ranges $[0, \pi]$ and $[-d, d]$ are discretized and for each contour point in the image Eq. 7.2 is calculated for all the angle values available: a *vote* is assigned to the corresponding location $(\overline{\theta}, \overline{\rho})$. Collinear points contribute mainly to increment the number of votes at the position $(\theta_L, \rho_L)$ of the line they belong to. Maxima are then searched to identify the lines present [DH72] in the image.

The formulation assumed by Kalmat et al. [KSG98] is the following:

$$\begin{aligned} \rho' &= x\cos\theta + y\sin\theta + \rho_{MAX} \\ &= x\cos\theta + y\sin\theta + \sqrt{M^2 + N^2} \end{aligned} \tag{7.3}$$

where

$$M, N : \textit{image dimension.}$$

The term $\sqrt{M^2 + N^2}$ was added in order to consider also negative values of $\rho$. Its value can be stored in memory as well as LUTs for $\cos\theta$ and $\sin\theta$ [DF03]. In this way, cosine and sine operations are performed just once for each value of $\theta$ in the range. LUTs were in this work calculated using an angle resolution of $\Delta\theta$ equal to 1°.

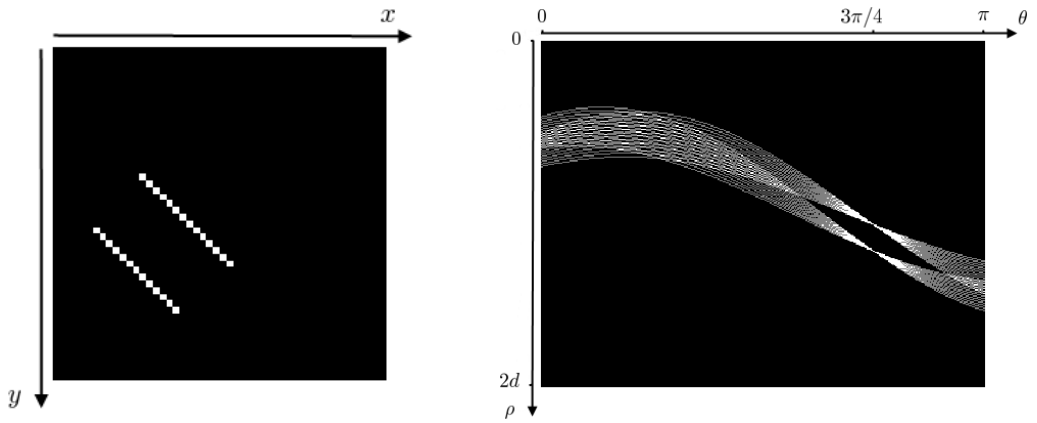


Fig. 7.6: Image of the accumulator array resulting after applying the Hough transform to an image containing two parallel lines at $\theta = 3\pi/4$ is shown in (b). The original image is depicted in (a).

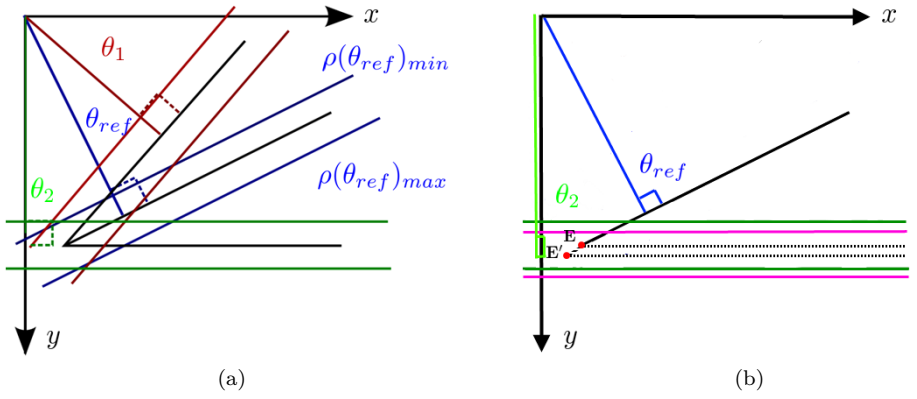


Fig. 7.7: (a) illustrates how the ranges for $\theta$ and $\rho$ change when a line rotates about a fixed axis orthogonal to the image plane. In (b) the effect of the displacement of the entry point along the direction defined by the planned trajectory is depicted.

The contours of the needle result in a couple of parallel lines after the edge detection step. In Fig. 7.6b, the accumulator array resulting from the application of Hough transform to a binary image containing two parallel lines is shown. The two peaks correspond to the values of $\rho$ and $\theta$ characterizing them. It can be also noticed that the space between the two peaks results in an absence of votes in the accumulator

array. These observations were exploited also by Jung et al. [JKYK06] in the attempt to develop an assisted parking system.

Using the same principle exploited for the region crop, based on Hyp.IV and given the planned trajectory, it is possible to assume that the needle rotation will be limited in a range $[\theta_{ref} - \theta_P, \theta_{ref} + \theta_P]$, where $\theta_{ref}$ is the angle described by the normal to the projected planned trajectory on the image plane (see Section 7.2) and $\theta_P$ a predefined value. In this work a value $\theta_P$ equal to 30° was considered as reasonable. Computation of Eq. 7.3 can therefore be restricted to this range and limited to the points that lie inside a circular sector constructed as described in Section 7.2 with an aperture angle of $\theta_P$. To discriminate whether a point lies inside the sector or not, the determinant $D$ of the following matrix can be exploited:

$$D = det \begin{bmatrix} x_A & y_A & 1 \\ x_B & y_B & 1 \\ x_P & y_P & 1 \end{bmatrix} \tag{7.4}$$

where

$$\begin{aligned} x_A, y_A, x_B, y_B &: \textit{indeces of two points defining a segment } \overline{AB}, \\ x_P, y_P &: \textit{indeces of the point, for which the relative position,} \\ &\quad \textit{w.r.t the segment } \overline{AB} \textit{ has to be investigated.} \end{aligned}$$

The determinant is positive if $P$ lies on one side of $\overline{AB}$, negative if it lies on the other side (see Fig. 7.8a). Normally, a convention needs to be established in order to discriminate which side is associated with a positive value.

In this work, two determinants, $D_S$, and $D_E$ are calculated as reference using the following combinations of points:

$$\begin{aligned} D_S : &\quad A = E_{Im}, B = T_{SIm}, &&\quad P = T_{Im}, \\ D_E : &\quad A = E_{Im}, B = T_{EIm}, &&\quad P = T_{Im}. \end{aligned} \tag{7.5}$$

where

$$T_{SIm}, T_{EIm} : \textit{extreme points of the circular sector}$$

For each edge point $P_E$, the above described determinant can be calculated, substituting its coordinates to $T_{Im}$:

$$\begin{aligned} D_{SP} : &\quad A = E_{Im}, B = T_{SIm}, &&\quad P = P_E, \\ D_{EP} : &\quad A = E_{Im}, B = T_{EIm}, &&\quad P = P_E. \end{aligned} \tag{7.6}$$

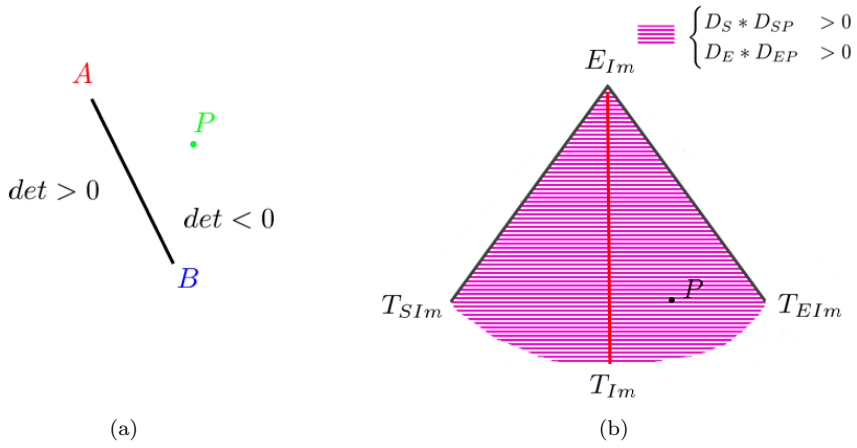


Fig. 7.8: (a) illustrates the relative position of a point w.r.t a line. The sign of the determinant calculated trough Eq. 7.4 reflects the side on which the point lies. Figure adapted from [SS05]. The dashed purple area depicted in (b) represents the region inside the circular sector. All points $P$ laying in this region give the same sign for the determinants as the reference point $T_{Im}$.

If the point lies inside the circular sector (see Fig. 7.8b), the determinants have respectively the same sign, therefore:

$$\begin{aligned} D_S * D_{SP} > 0, \\ D_E * D_{EP} > 0 \end{aligned} \tag{7.7}$$

This property of the determinant was used by Saxena et al. [SS05] to evaluate the proximity of a point to a line.

The needle contours move parallel to the centerline in a similar manner. Since the radius of the needle artifact is not expected to change, constraints can be added also when looking for peaks in the parameter space. A candidate pair of peaks is searched for through each column of the accumulator array, but the investigation is restricted to the range $[\rho(\theta^*)_{ref} - L, \rho(\theta^*)_{ref} + L]$, where $\theta^*$ is the angle value of the column under investigation, $\rho(\theta^*)_{ref}$ is the value that would correspond to the needle centerline if it would be oriented at $\theta^*$ and $L$ is equal to $\frac{\rho(\theta_{ref})_{max} - \rho(\theta_{ref})_{min}}{2}$. The value $2L$ expresses the maximum distance expected between the couple of needle contours. $\rho(\theta^*)_{ref}$ can be calculated from Eq.7.3, using the coordinates of the projected entry point.

If the lesion is located in a region affected by the respiratory movement, like the liver, the slight displacement induced on the entry point position can be approximated as occurring along the direction of the planned trajectory. The shift can be accounted for assuming a higher value for $L$ without loss of generality of Hyp.IV as illustrated in Fig. 7.7b.

The value of $L$ needs to be adapted depending on the image scan resolution and

the size of the needle artifact expected. In this work, $L$ was set equal to 7, since considered sufficient to cover the distance betweeen the needle contours in the images used for the evaluation.

For each $\theta^*$ two peaks are identified and the following cost function is evaluated:

$$J = q(H_1) + q(H_2) - \frac{\sum_{i=0}^{n} q_i}{q(H_1) + q(H_2)} \tag{7.8}$$

where

$$\begin{aligned} q(H_1) &: \textit{value of the accumulator array at the first peak } H_1, \\ q(H_2) &: \textit{value of the accumulator array at the second peak } H_2, \\ q_i &: \textit{value of the accumulator array of the } i^{th} \textit{ point located} \\ &\quad \textit{between the two peaks.} \end{aligned}$$

The two couples of parameters $(\theta^*, \rho_1)$ and $(\theta^*, \rho_2)$ for which J assumes its maximum are regarded as the candidate needle contours. The formulation of $J$ represents a variation of the one proposed by Jung et al. [JKYK06].

The needle centerline is identified by the the parameters $\theta^*$ and $\rho_C$ where $\rho_C$ is obtained as the mean value of $\rho_1$ and $\rho_2$. At this point, substituting either the $x$ or $y$ coordinates of the projections of the entry and target points in Eq. 7.6, the estimated centerline can be reported in the image space.

Since the edge detection and the Hough transform are performed on a cropped image, before calculating the world coordinates of the needle centerline, the following transformation needs to be performed, following Eq. 7.1

$$\begin{aligned} x &= x_C + x'_O, \\ y &= y_C + y'_O, \end{aligned}$$

where

$$\begin{aligned} x_C, y_C &: \textit{indeces of a point of the needle} \\ &\quad \textit{centerline in the crop image,} \\ x'_O, y'_O &: \textit{indeces of the new image origin} \\ &\quad \textit{in the original image ,} \\ x, y &: \textit{indeces of a point of the needle} \\ &\quad \textit{centerline in the original image.} \end{aligned}$$

The detection of the needle centerline by means of the Hough transform is implemented in the **SoNSegHoughCone** module whose input and output fields are reported respectively in Table 3. In Fig. 7.10 a screenshot of the implemented scenegraph is provided.

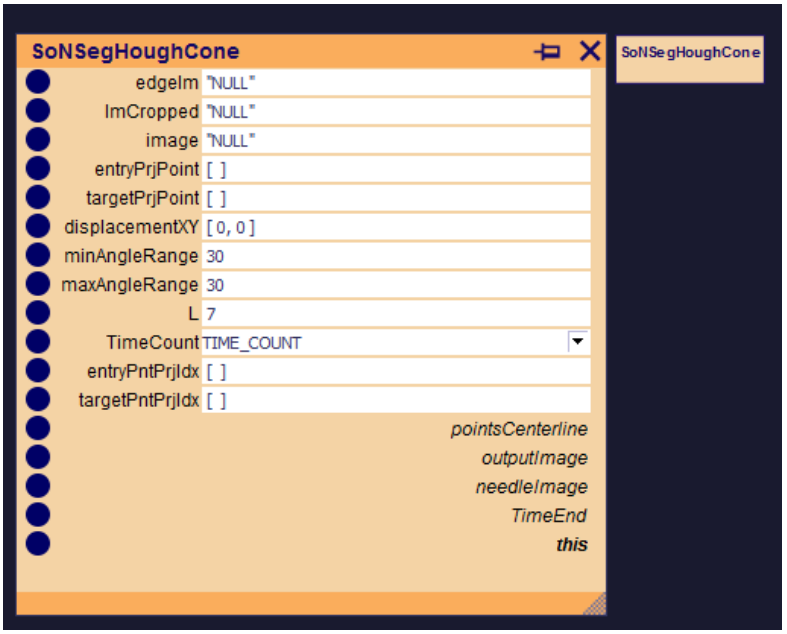


Fig. 7.9: Screenshot of the SoNSegHoughCone module

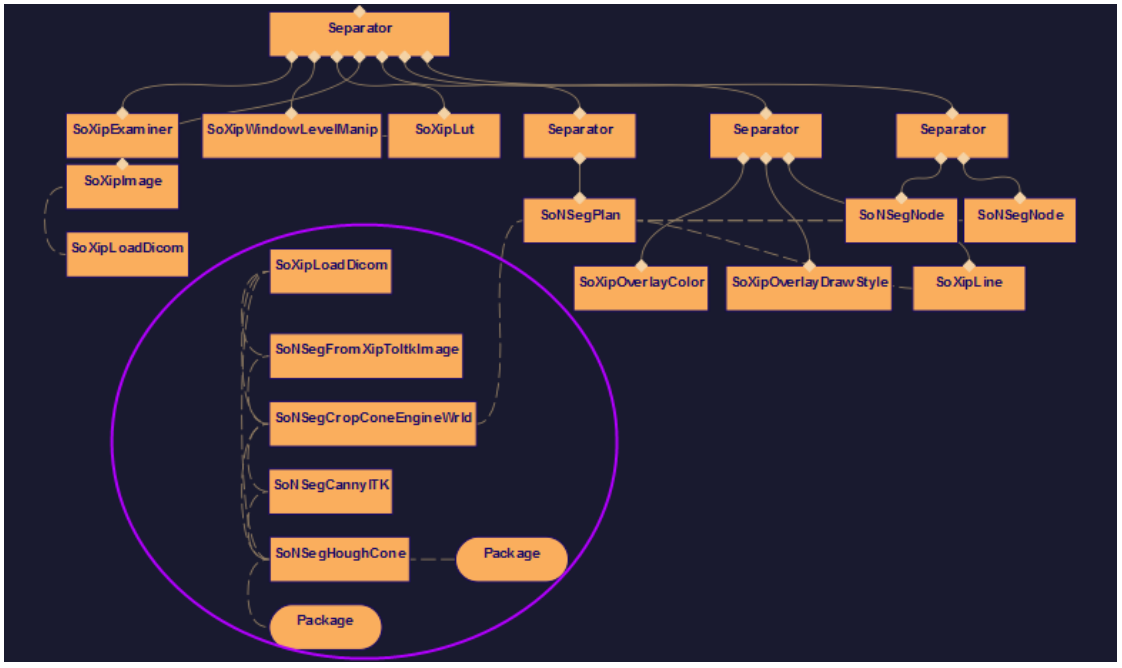


Fig. 7.10: Scenegraph of the needle detection algorithm by means of Hough transform and highlighted by the purple circle. The rest of the scene graph refers to a simulation of the planning step, in order to provide entry and target point.

Table 3: Input and Output Fields of the SoNSegHoughCone (SoEngine)

| **SoNSegHoughCone (SoEngine)** | | |
|---|---|---|
| **Input Field** | **Field Type** | **Description** |
| edgeIm | SoItkSFDataImage | Input image coming from a SoNSegCannyITK engine |
| image | SoXipSFDataImage | Original dicom image coming from a SoXipLoadDicom engine |
| ImCropped | SoItkSFDataImage | ITK image coming from the SoNSegCropConeEngineWrld |
| entryPrjPoint | SoMFVec3f | 3D coordinates of the needle entry point projected onto the image plane |
| targetPrjPoint | SoMFVec3f | 3D coordinates of the needle target point projected onto the image plane |
| targetPntPrjIdx | SoMFVec3f | Image indeces of the needle entry projection point |
| entryPntPrjIdx | SoMFInt32 | Image indeces of the needle target projection point |
| displacementXY | SoMFInt32 | Image indeces of the new origin of the image after the cropping process |
| minAngleRange | SoSFFloat | First half of the aperture angle, developing from the projected planned trajectory (30°) |
| maxAngleRange | SoSFFloat | Second half of the aperture angle, developing from the projected planned trajectory (30°) |
| L | SoSFFloat | Half of the range for $\rho$ used in the needle centerline detection (7) |
| TimeCount | SoSFEnum | Drop-down menu that allows to decide if the ending time of the processing has to be registered (TIME_COUNT) |
| **Output Field** | **Field Type** | **Description** |
| pointsCenterline | SoMFVec3f | 3D coordinates of the needle centerline |
| outputImage | SoItkSFDataImage | Accumulator array resulting from the Hough transform |
| needleImage | SoItkSFDataImage | Cropped image in input with superimposition of identified needle centerline |

### 7.4.2 Small Eigenvalue Algorithm

Identification of needle contours by means of Hough Transform can be affected when several structures are present in the image. Their contours are likely to be detected as edges during the edge detection step. As such, they contribute to the computation of the accumulator array. The greater the number of lines, the higher the number of peaks in the accumulator array. In addition, each contour increase the number of spreaded shapes, like the one depicted in Fig. 7.6b. In this situation, the identification of the needle contours can be affected.

Guru et al. [GSN04] proposed a method to emphasize straight lines in an binary image. The method relies on the property of the covariance matrix that can be calculated from the image coordinates of the points of objects. A mask $M$ of dimension $k$x$k$ is moved through the image. At each step the mask is centered at one of the edge pixels detected during the edge detection step till all the edge pixels are visited(see Fig. 7.11). Each pixel is visited just once. Once the mask is in place, the 8-th connected component $CC$ of the central pixel is calculated and the corresponding covariance matrix $C$ is computed. The set of edge pixels laying inside the mask $M$ and belonging to $CC$ is referred as $S$:

$$S = \{(x_i, y_i) \in M | f(x_i, y_i) = 1 \wedge f(x_i, y_i) \in CC(x_c, y_c)\}$$

$$C = \begin{pmatrix} c_{11} & c_{12} \\ c_{21} & c_{22} \end{pmatrix} \tag{7.9}$$

where

$$\begin{aligned} c_x &= \frac{1}{m} \sum_{i=1,..,m} x_i, & c_y &= \frac{1}{m} \sum_{i=1,..,m} y_i \\ c_{11} &= \frac{1}{m} \sum_{i=1,..,m} x_i^2 - c_x^2, & c_{22} &= \frac{1}{m} \sum_{i=1,..,m} y_i^2 - c_y^2 \\ c_{12} &= \frac{1}{m} \sum_{i=1,..,m} x_i y_i - c_x c_y, & c_{21} &= c_{12} \\ m &= |S| \end{aligned}$$

From the covariance matrix the minimum eigenvalue is obtained:

$$\lambda = \frac{1}{2}[c_{11} + c_{22} - \sqrt{(c_{11} - c_{22})^2 + 4c_{12}^2}] \tag{7.10}$$

The value $\lambda$ is assigned to all the pixels belonging to $S$. Since the mask is moving, the same pixel $P_i$, if not isolated, is assigned with several small eigenvalues, forming

a set $F_i$ associate to it. When all the edge pixels are visited, the minimum small eigenvalue of each $F_i$ is considered. If the minimum is lower than a threshold $t$, the associated pixel $P_i$ is regarded as belonging to a straight line. If the cardinality of $F_i$ is equal to one, the pixel is considered as noisy and disregarded.

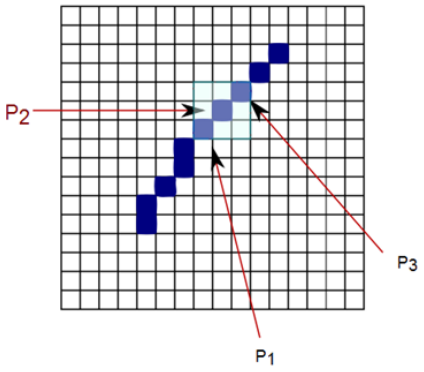


Fig. 7.11: A 3x3 mask is centered on the point $P2$. This point together with the connected $P1$ and $P3$ form the family set $F$ associated to $P2$.

When the mask $M$ is centered at an edge pixel, a portion of the contour to which the pixel belongs is investigated. If the eigenvectors of the associated covariance matrix were calculated, the greatest eigenvalue would be associated to the eigenvector, along whose direction the highest variance is found, in other words, the main direction along which the contours develops.

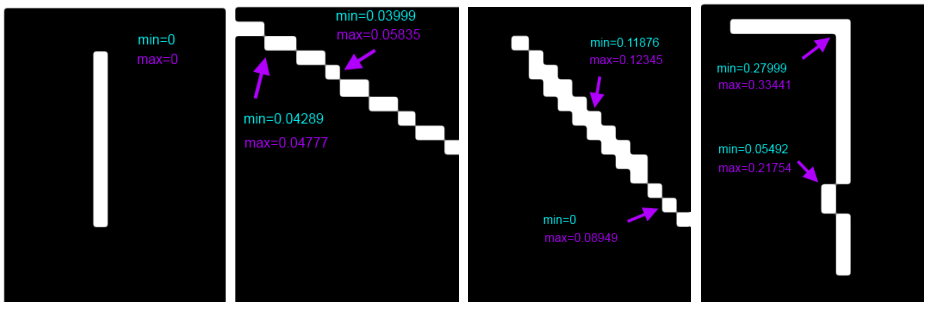


Fig. 7.12: Some examples of small eigenvalue calculation are shown. In each image, a 5x5 mask was used. The minimum and maximum small eigenvalue associated to salient pixels after the processing are reported. As expected, the values increase with the irregularity of the shape.

On the other hand, the smallest eigenvalue can be regarded as a measure of the deviation, orthogonally to the main direction, encountered inside the current window. Moving the mask, different areas of the image are subsequently considered. If the same pixel happens to be part of the connected component set more than once, it means that it belongs to an aggregate of pixels, in this case a contour. If the contour is not straight, for example it bends at a certain point, the pixels right at the bend can not be unambiguously regarded as belonging to one side

of the contour or to the other. Keeping the smallest among the set of small $\lambda$ is like assigning it to the one where it best fits. High values for the small eigenvalue indicate that the pixel does not belong to a shape strongly developing along a main direction, like a straight line. The larger the mask size $M$, the higher the ratio of pixels that assumes a large small eigenvalue. However, using a bigger mask size implies an increment of processing time. In this work, a 5x5 mask was used. Examples illustrating the variability of the small eigenvalue are shown in Fig. 7.12.

### 7.4.3 Edge Linking

Once the edge image, processed with the small eigenvalue algorithm is available, it is necessary to identify the straight segments that belong to the needle contour. The first step is to identify the candidate needle direction that can be used as a term of comparison to discriminate the segments. A circular sector having as vertex the image coordinate of the entry point projection $E_{Im}$, the distance $d(E_{Im}, T_{Im})$ as ray and a half aperture angle of 30° is defined. With reference to Hyp.II, the darkest straight path, having $E_{Im}$ as starting point and located inside the circular sector is searched.

$$d = \int |f(s)|^2 \, \mathrm{d}s = min \tag{7.11}$$

where

$$s : \textit{investigated direction},$$
$$f(s) : \textit{intensity level along the path}$$

During the search, the direction $s$ is varied inside the circular sector with a step of 1°. Once the direction along which the squared sum of intensities reaches its minimum is known, a normalized vector $\vec{\mathbf{V}}_{\mathbf{Trj}}$ is used to store the direction information. Since the artifact produced by the needle is expected to be one of the darkest features in the image, the path identified can be regarded as an approximation of the direction along which the needle is more likely to be.

An edge linking algorithm is then applied with the aim to link fragments of the needle contour, produced either by the Canny algorithm or as a consequence of the small eigen value algorithm. Broken edges detected by the Canny algorithm often occur when the needle crosses regions whose intensities in the MR images are similar to the ones characterizing the needle artifact, as depicted in Fig. 7.13. The edge linking is adapted from the algorithm proposed by Vasudevan et al. [VCBC88] for road detection application.

A list of all the edge segments present in the image is made during the edge linking

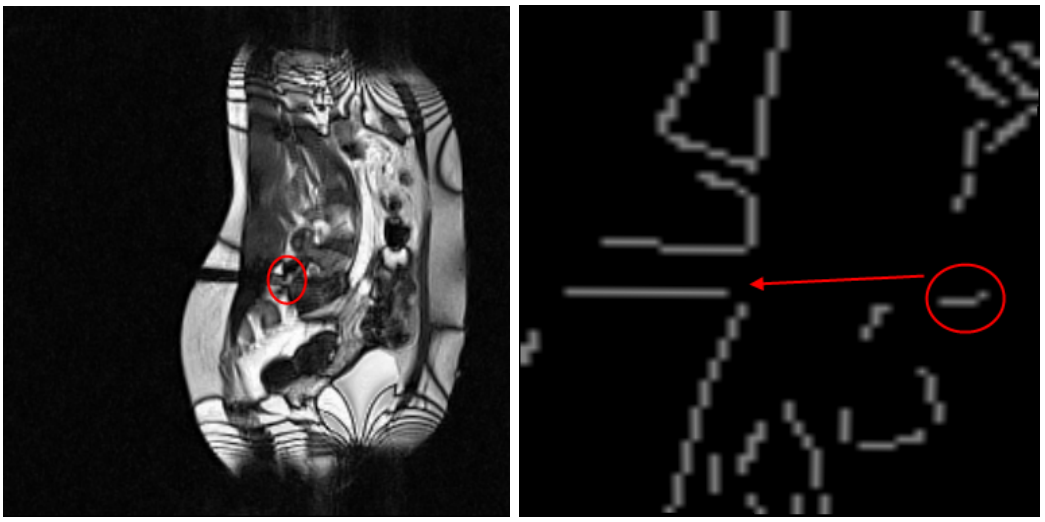

(a) (b)

Fig. 7.13: In (a), an example of a needle artifact that crosses an area of similar intensities is shown. Just the first part of the needle and the needle tip are clearly visible. In between, no clear distinction among the intensity levels can be appreciated. The result of the cropping, edge detection and small eigenvalue algorithm is shown in (b). The red ellipse highlights the edge fragment belonging to the needle tip, whereas the red arrow points to the needle contour, to which the fragment should be linked.

step. For each segment the following parameters are stored:

$$\begin{aligned} Idx_{Start} &: \textit{starting point of the segment}, \\ Idx_{End} &: \textit{ending point of the segment}, \\ \theta &: \textit{segment orientation angle}, \\ PxlList &: \textit{list of pixels belonging to the segment}. \end{aligned}$$

The edge pixels are stored in order, so that $Idx_{Start}$ and $Idx_{End}$ identify the extreme points of the contour. The distinction between starting and ending is based just on the order they were encountered when tracking the segment. The angle $\theta$ is calculated after performing a linear interpolation of the pixels coordinates. If the orientation difference with respect to the darkest path identified is greater than 45°, the segment is erased from the list and therefore disregarded for the following processing.

The success of the edge linking step is strongly dependent from the outcome of the small eigenvalue algorithm. A threshold too low could cause the cancellation of important fragments belonging to the needle contour, mining from the very beginning a correct detection. On the other hand, a threshold too high induces a higher ratio of edge pixel surviving to the small eigen value thresholding. In this situation, the mere needle contours can result still connected with edges belonging to other structure present in the surroundings.

This surviving connection manifest in particular in the proximity of the needle entry, close to the body surface. As a consequence of the layer of fat tissue, the first stretch of the needle can not be distinguished and the inner contour of the

fat layer result connected with the detected edges of the needle (see Fig. 7.14b). In this work, it was therefore decided to adopt a relative high threshold for the small eigenvalue filter, T = 0.1, and to try to solve the problem of the residual connection in a second step.

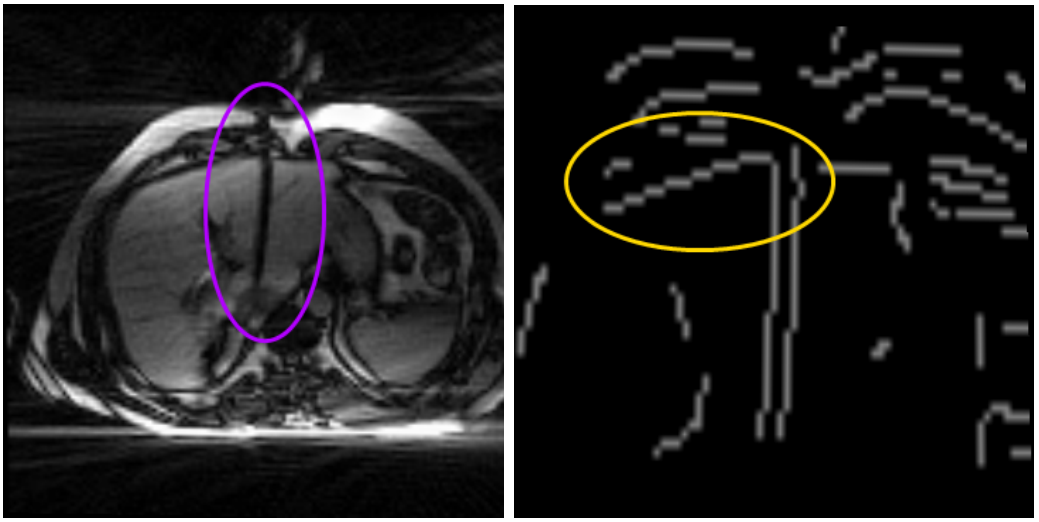

(a) (b)

Fig. 7.14: Original image (a) and the image resulting after cropping, edge detection and small eigenvalue filtering (b). The residual connection between one needle contour and the layer close to the body surface is highlighted by the yellow ellipse.

Before performing the linear interpolation described above, the segments undergo a position test based on the same determinant comparison described in Section 7.4.1. If one of the extreme points of the segment is not inside the circular sector, the segment is walked backward and the points located outside the sector are sequentially removed from the PxlList. The removal contributes to make the direction defined by the points belonging to the needle contour predominant after the interpolation. In addition, also IdxStart and IdxEnd better approximate the extreme points of the needle edges. The removal proves to improve the accuracy of the detection. An example is provided in Fig. 9.5 in Section 8.

Before segments can be linked together to form a common path, candidate neighbors for each of them need to be found. A neighbor is defined as follows:

**Ch.1** the *candidate* segment has to lie inside a cylinder projection that has the reference segment as axis and a ray $r$ equal to 5 pixels.

**Ch.2** the orientation difference between the reference and candidate segments needs to be not greater than 10°.

**Ch.3** reference and candidate need not to be *overlapping*

The ray of the cylinder establishes a first distance discrimination term. A second distance requirement is presented later in this section. In Fig. 7.15 it is shown what is meant by overlapping segments. Fragments belonging to one of the two sides of the needle contours should ideally be disposed as depicted in Fig. 7.15a: one segment follows the other and there is no overlap between one segment and the projections of the extreme points of the other onto its direction. If an overlap occurs, the two segments are very likely belonging to two distinct contours. In particular, they could be segments deriving from the two different sides of the needle. As such, they should not be identified as neighbors, because they should not be linked to each other.

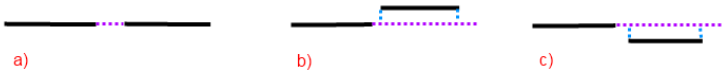


(a) Not overlapping segments

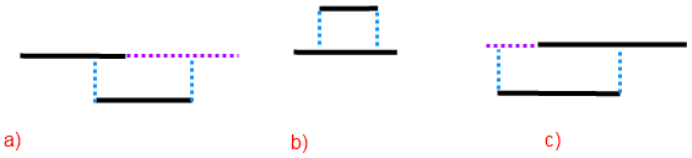


(b) Overlapping segments

Fig. 7.15: In (a) not overlapping segments are depicted. In (b) overlapping segments are shown.

In order to avoid overlapping segments to be regarded as neighbors, the following analysis is performed. The ending points of the reference and candidate segments are considered. From them, the four vectors connecting them are calculated (see Fig. 7.16).

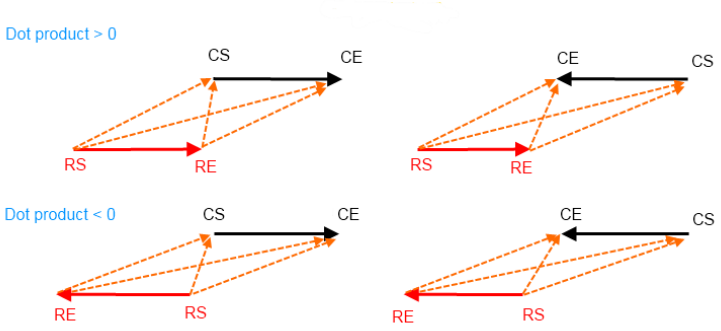


Fig. 7.16: The four possible combinations of not overlapping vectors arrangement are shown. The connecting vectors are depicted in orange, the reference vector in red and the candidate vector in black. In the first row the dot products result greater then zero. In the cases depicted in the second row the dot products result all smaller than zero.

In Fig. 7.16 reference and candidate segments are depicted respectively in black and red. The ending points are referred respectively as RS, RE, CS, CE. The heads of the depicted arrows indicate the possible ways in which pixels could be stored

when tracking the edge, influencing how the ending points are named. It is worth remembering that definition of starting and ending point has no absolute meaning. The dot product between each of the connecting vectors and the reference segment are calculated. The reference segment is now considered as a vector, heading from RS to RE. If the two segments are not overlapping, the four dot products established result all either positive or negative.

If the candidate is not overlapping, the orientation of the two segments is compared. Since edges are often irregulars, calculation of $\theta$ is affected by the number of pixels of the segment. If an edge is broken into several fragments, the short segments are more likely to manifest after the interpolation step a larger angle deviation from the visible direction they belong to. A value of 10° for the orientation difference was considered suitable to account for such irregularity.

It is also necessary to know through which endings the connection should be established, in order to perform the edge linking. Euclidean distances between the segment endings are therefore calculated. The couple of endings assigned to the smallest distance is chosen. The distance from the ending belonging to the candidate and the line on which the reference segment lies is also calculated. If this value is greater than a threshold $th$ the segment is disregarded, otherwise it is classified as neighbor. The following property can now be added to the definition of neighbor reported above:

**Ch.4** the distance from the candidate ending to the direction of the reference segment should not be greater than $th$.

Fragments belonging to the same contour should lie very close to each other. A value of 1.5 has therefore be used for $th$. This is also the reason why in Fig. 7.15 the not overlapping segments are depicted so close in comparison with the overlapping segments.

The neighboring relation is reflexive: if the candidate is identified as neighbor of the reference, the reference is also classified as neighbor of the candidate. Therefore, a couple of segments is tested for the neighboring relation just once.

After the neighboring selection described above, each segment has a list of start-neighbors and end-neighbors. Using the clustering algorithm described in [VCBC88], a path object *SoNSegPathObj* is built storing all the segments which belong to it. Once the path is available, the information stored concerning the ending points is used to fill the gap between the segments: a line is traced from the two endings and the image coordinates of the pixels forming the new line are stored into the SoNSegPathObj.

For each path available, linear interpolation is performed over the coordinates of all the pixels building the path. For each path, the absolute value of the dot product between the normalized darkest path trajectory, $\vec{\mathbf{V}}_{\mathbf{Trj}}$ and the normalized vector approximating the path direction after the interpolation, $\vec{\mathbf{V}}_{\mathbf{Path}}$, is obtained. Given the starting and ending point of the path, respectively $S_{Path}$ and $E_{Path}$, their

distances from the darkest path line are also calculated and summed together giving $d_{Path}$:

$$d_{Path} = d(S_{Path}, \vec{\mathbf{V}}_{\mathbf{Trj}}) + d(E_{Path}, \vec{\mathbf{V}}_{\mathbf{Trj}}) \tag{7.12}$$

where

$$d(S_{Path}, \vec{\mathbf{V}}_{\mathbf{Trj}}) : \textit{distance of the starting point of } \vec{\mathbf{V}}_{\mathbf{Path}} \textit{ from } \vec{\mathbf{V}}_{\mathbf{Trj}}$$
$$d(E_{Path}, \vec{\mathbf{V}}_{\mathbf{Trj}}) : \textit{distance of the ending point of } \vec{\mathbf{V}}_{\mathbf{Path}} \textit{ from } \vec{\mathbf{V}}_{\mathbf{Trj}}$$

The following cost term is then evaluated:

$$J = \frac{d_{Path}}{d_{MAX}} + \frac{1}{|cos(\vec{\mathbf{V}}_{\mathbf{Trj}}, \vec{\mathbf{V}}_{\mathbf{Path}})|} \tag{7.13}$$

where

$$d_{MAX} : \textit{maximum } d_{Path} \textit{ value encountered.}$$

The first term assumes a minimum value equal to zero if the two ending points of the path lie on the line of the darkest path. The second term assumes a maximum value equal to 1 if $\vec{\mathbf{V}}_{\mathbf{Path}}$ and $\vec{\mathbf{V}}_{\mathbf{Trj}}$ are parallel or anti parallel. The cost term J assumes therefore values in the range $[0, \infty]$. The two paths returning the two smallest values of the cost term, $J_1$ and $J_2$, are identified as the needle contours.

From the two identified contours, the approximated needle centerline is obtained. The projected entry point $E_{Im}$ is now projected onto the two needle sides. From the projection the average entry point $P_{EM}$ is calculated.

$$P_{EM} = \frac{E_{Im,Prj1} + E_{Im,Prj2}}{2} \tag{7.14}$$

where

$$E_{Im,Prj1} : \textit{projection of } E_{Im} \textit{ onto } \vec{\mathbf{V}}_{\mathbf{Path1}}$$
$$E_{Im,Prj2} : \textit{projection of } E_{Im} \textit{ onto } \vec{\mathbf{V}}_{\mathbf{Path2}}$$

If the dot product between $\vec{\mathbf{V}}_{\mathbf{Path1}}$ e $\vec{\mathbf{V}}_{\mathbf{Path2}}$, expressing the direction of the two needle sides is positive, an approximated centerline $\vec{\mathbf{V}}_{\mathbf{C}}$ is calculated through vector addition, otherwise by means of vector subtraction.

$$\vec{\mathbf{V}}_{\mathbf{C}} = P_{EM} + \vec{\mathbf{V}}_{\mathbf{M}}, \tag{7.15}$$

where

$$\vec{\mathbf{V}}_{\mathbf{M}} = \begin{cases} \vec{\mathbf{V}}_{\mathbf{Path1}} + \vec{\mathbf{V}}_{\mathbf{Path2}}, & \text{if} \quad \vec{\mathbf{V}}_{\mathbf{Path1}} \cdot \vec{\mathbf{V}}_{\mathbf{Path2}} > 0 \\ \vec{\mathbf{V}}_{\mathbf{Path1}} - \vec{\mathbf{V}}_{\mathbf{Path2}}, & \text{if} \quad \vec{\mathbf{V}}_{\mathbf{Path1}} \cdot \vec{\mathbf{V}}_{\mathbf{Path2}} < 0 \end{cases}$$

Since the edge detection, the small eigenvalue filtering and the edge linking are performed on a cropped image, before calculating the world coordinates of the needle centerline, the corresponding pixel indeces in the original image of the pixels belonging to the detected centerline need to be calculated as described in Section 7.4.1.

The detection of the needle centerline by means of the edge linking is implemented in the **SoNSegEdgeList** module whose input and output fields reflect the fields of the SoNSegHoughCone. Just the *entryPrjPoint*, *targetPrjPoint* and $L$ fields are not present. In Fig. 7.18 a screenshot of the implemented scenegraph is provided. The output and input fields of the **SoNSegEdgeList** module are reported in Table 4.

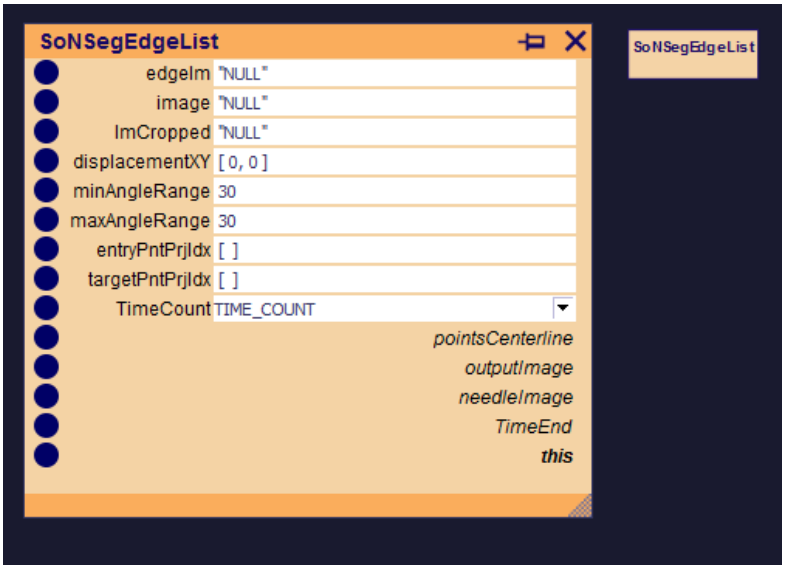


Fig. 7.17: Screenshot of the SoNSegEdgeList module

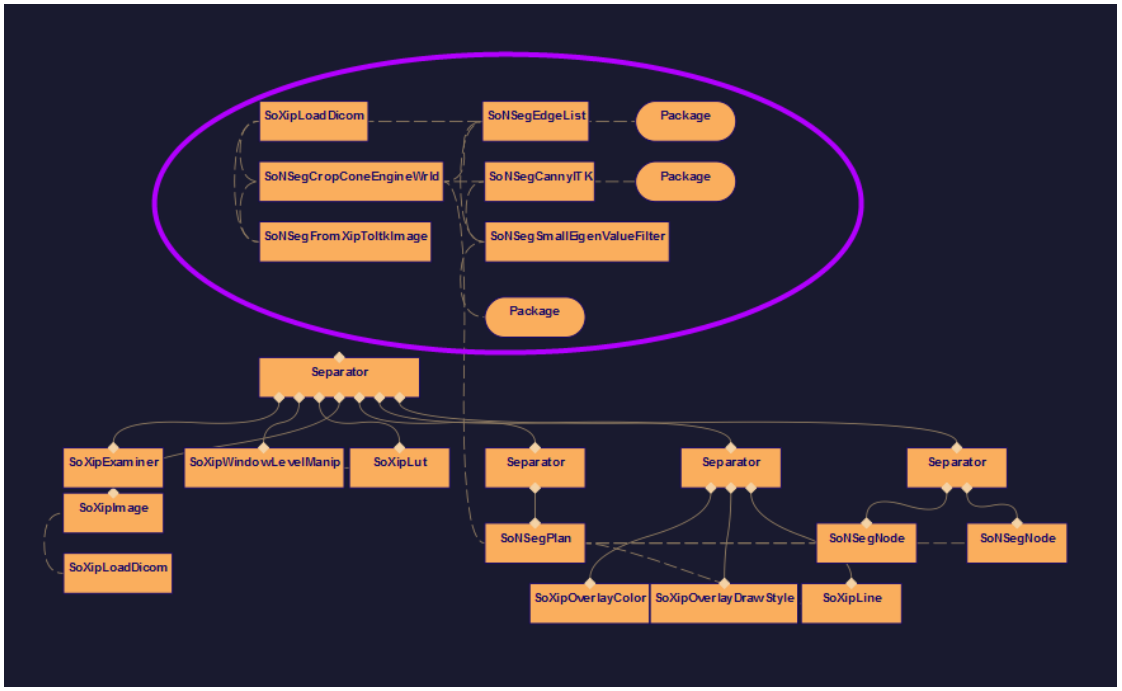


Fig. 7.18: The Scenegraph of the needle detection algorithm by means of the small eigenvalue algorithm and edge linking is highlighted by the purple circle. The rest of the scene graph refers, as in Fig. 7.10 to a simulation of the planning step, in order to provide the entry and target point.

Table 4: Input and Output Fields of the SoNSegEdgeList (SoEngine)

| **SoNSegEdgeList (SoEngine)** | | |
|---|---|---|
| **Input Field** | **Field Type** | **Description** |
| edgeIm | SoItkSFDataImage | Input image coming from a SoNSegCannyITK engine |
| image | SoXipSFDataImage | Original dicom image coming from a SoXipLoadDicom engine |
| ImCropped | SoItkSFDataImage | ITK image coming from the SoNSegCropConeEngineWrld |
| targetPntPrjIdx | SoMFVec3f | Image indeces of the needle entry projection point |
| entryPntPrjIdx | SoMFInt32 | Image indeces of the needle target projection point |
| displacementXY | SoMFInt32 | Image indeces of the new origin of the image after the cropping process |
| minAngleRange | SoSFFloat | First half of the aperture angle, developing from the projected planned trajectory (30°) |
| maxAngleRange | SoSFFloat | Second half of the aperture angle, developing from the projected planned trajectory (30°) |
| TimeCount | SoSFEnum | Drop-down menu that allows to decide if the ending time of the processing has to be registered (TIME_COUNT) |
| **Output Field** | **Field Type** | **Description** |
| pointsCenterline | SoMFVec3f | 3D coordinates of the needle centerline |
| outputImage | SoItkSFDataImage | Accumulator array resulting from the Hough transform |
| needleImage | SoItkSFDataImage | Cropped image in input with superimposition of identified needle centerline |

# 8 Evaluation

For the evaluation 10 patient data sets were used. The total number of images was 452. The images were acquired during needle insertion for subsequent thermal ablation. In all the interventions one needle was used. The datasets were named with the letter P and a progressive number from 1 to 10. Dataset 1 to 6 and dataset 8 were acquired during radio frequency ablation procedures, whereas dataset 7, 9 and 10 were acquired during cryoablation procedures. Acquisition parameters of the radiofrequency ablation datasets are reported in Table 5, whereas acquisition parameters of cryoablation datasets can be found in Table 6. All datasets were acquired with a Siemens MAGNETOM Espree 1.5T Scanner. The body coil was used for reception. From the data sets, images where no needle was visible were disregarded. When available, images in the same dataset were divided in groups according to their scan direction (i.g sagittal versus coronal), in order to test also the robustness of the algorithm as concerning the needle orientation with respect to the axes of the image. Since 7 out of the 10 datasets were strongly affected by striping artifacts, it was decided not to perform the preprocessing in order to allow a better comparison.

Table 5: Acquisition Parameters for Patient Dataset 1 to 6 and 8

| | TE(ms) | TR(ms) | BW($HzPxl^{-1}$) | Spacel Resolution(mm) | Flip Angle(°) |
|---|---|---|---|---|---|
| P1 | 2.16 | 4.32 | 560 | 2.9x2.9x5 | 70 |
| P2 | 1.8 | 482.63 | 1030 | 2.3x2.3x2 | 50 |
| P3 | 1.66 | 794.51 | 930 | 3.1x3.1x10 | 90 |
| P4 to P6 and P8 | 2.16 | 4.32 | 560 | 2.9x2.9x5 | 70 |

Table 6: Acquisition Parameters for Patient Dataset 7 and 9 to 10

| | TE(ms) | TR(ms) | BW($HzPxl^{-1}$) | Spacel Resolution(mm) | Flip Angle(°) |
|---|---|---|---|---|---|
| P7 | 3.81 | 387.32 | 200 | 1.7x1.6x4 | 70 |
| P9 | 2.18 | 812.6 | 302 | 1.6x1.6x4 | 50 |
| P10 | 2.12 | 792.7 | 302 | 1.8x1.8x4 | 50 |

The algorithm based on Hough transform and the algorithm exploiting the small eigenvalue and edge linking were both evaluated. Beside the scenegraphs strictly related to their implementation, an additional network was built in order to simulate the planning step. The network is depicted in Fig. 8.2. The most important module in the network is the **SoNSegPlan** module (see Fig. 8.1). Input and output fields can be found in Table 7. It allows to select, by means of a mouse press, alternatively the two extreme points of the needle, choosing ENTRY or TARGET from the drop-down field *IDPoint*. The 3D coordinates of the entry and target point selected become therefore available and can be used as inputs to the SoNSegCropConeEngineWrld module. An instance of the latter is present in both the needle detection networks.

For each data set available, an entry and a target points were defined. When present, the original target point signed in the images were used. If not present, two images were chosen randomly and used to define the target point from the center of lesion visible. A mean target point $T_M$ was calculated from the two points selected. For each data set a mean entry point $E_M$ was also defined.

$$E_M = (\frac{x_{E1} + x_{E2}}{2}, \frac{y_{E1} + y_{E2}}{2}, \frac{z_{E1} + z_{E2}}{2}), \tag{8.1}$$
$$T_M = (\frac{x_{T1} + x_{T2}}{2}, \frac{y_{T1} + y_{T2}}{2}, \frac{z_{T1} + z_{T2}}{2}),$$

where

$$(x_{E1}, y_{E1}, z_{E1}), (x_{E2}, y_{E2}, z_{E2}) : \textit{3D coordinates of the entry points selected in two images from the data set}$$
$$(x_{T1}, y_{T1}, z_{T1}), (x_{T2}, y_{T2}, z_{T2}) : \textit{3D coordinates of the target points selected in two images from the data set}$$

The entry and target points provided were connected to the *entryPoint* and *targetPoint* fields of the SoNSegCropEngineWrld engine. The same entry and target points were used as inputs for both the needle detection networks. The values defined remained fixed during all the evaluation.

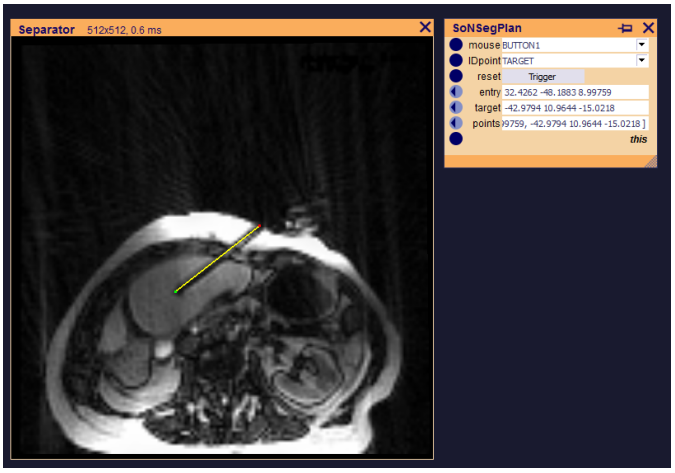


Fig. 8.1: Screenshot showing the outcome of the manual segmentation (yellow) and overlayed needle centerline (red). The field window of the SoNSegPlan module is also depicted.

Table 7: Input Fields of the SoNSegPlan (SoNode)

| **SoNSegPlan (SoNode)** | | |
|---|---|---|
| **Input Field** | **Field Type** | **Description** |
| mouse | SoSFEnum | Button of the mouse to use to select the point on the image |
| IDPoint | SoSFEnum | Selection of the identifier of the point to be stored: ENTRY/TARGET/ NO_POINT |
| reset | SoSFTrigger | Trigger used to reset the entry, target and points fields |
| entry | SoMFVec3f | Segmented entry needle point |
| target | SoMFVec3f | Segmented target needle point |
| points | SoMFVec3f | Both the segmented entry and target points |

Table 8: Input and Otput Fields of the SoNSegEvaluate (SoEngine)

| **SoNSegEvaluate (SoEngine)** | | |
|---|---|---|
| **Input Field** | **Field Type** | **Description** |
| SegEntryPoint | SoMFVec3f | 3D coordinates of the manually segmented entry needle point |
| SegTargetPoint | SoMFVec3f | 3D coordinates of the manually segmented target needle point |
| NeedleCenterline | SoMFVec3f | 3D coordinates of the points belonging to the detected needle centerline |
| reset | SoSFTrigger | Reset the the above described fields |
| TimeCount | SoSFEnum | If TIME_COUNT the time of the processing is calculated, otherwise NO_TIME_COUNT |
| TimeStart | SoSFFloat | Clocks at the start of the processing |
| TimeEnd | SoSFFloat | Clocks at the end of the processing |
| **Output Name** | **Field Type** | **Description** |
| dist | SoSFFloat | Euclidean distance between the segmented entry point and the start point of the centerline |
| angle | SoSFFloat | Deviation angle of the centerline from the detected needle (°) |
| cos | SoSFFloat | Cosine of deviation angle |
| distLine | SoSFFloat | Distance of the segmented entry point from the detected needle centerline (mm) |
| RunTime | SoSFFloat | Runtime (ms) |

Manual segmentation of the needle was perfomed on each image, in order to compare the real needle position with the detected one (see Fig. 8.1). The same scenegraph used to simulate the planning was used for the manual segmentation. The detected needle centerline was also overlayed in red color to the image in order to allow visual comparison with the actual needle position.

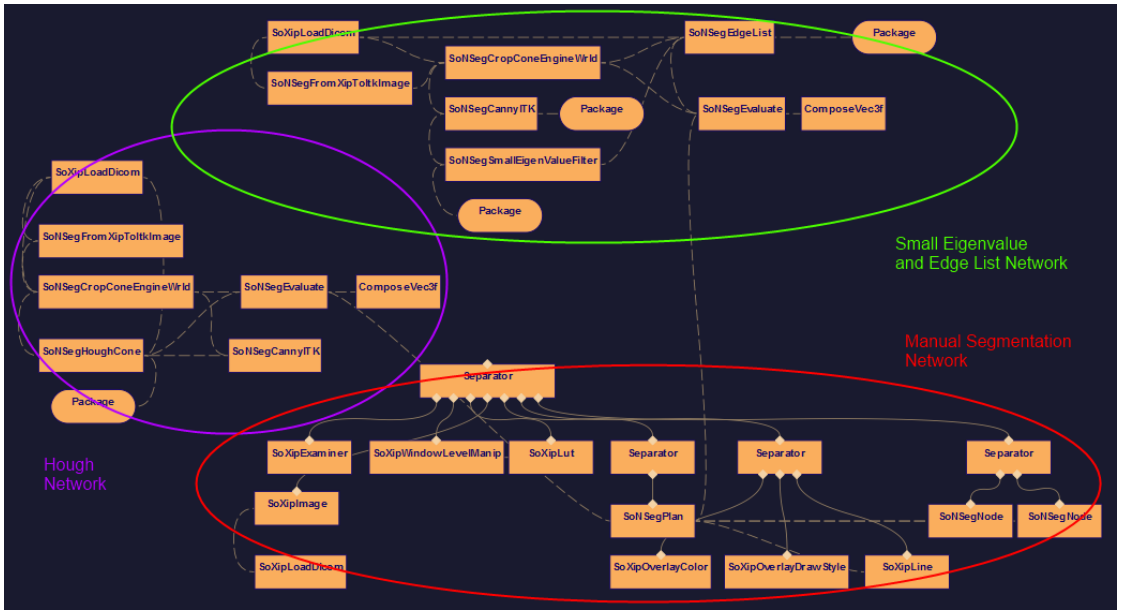


Fig. 8.2: Screenshot of the network used for the evaluation. Each subnetwork is highlighted by an ellipse of a different colour

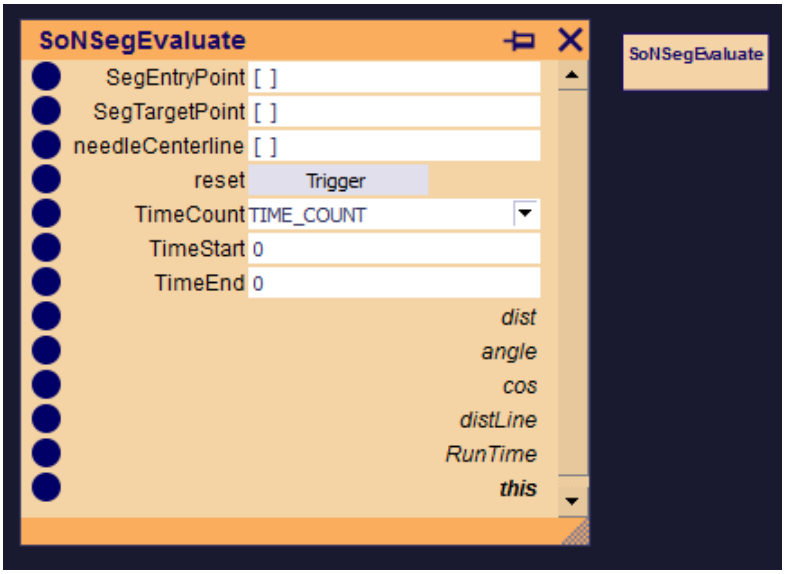


Fig. 8.3: Screenshot of the SoNSegEvaluate module

The *pointsCenterline* fields of the *SoNSegHoughCone* and of the *SoNSegEdgeList* modules are connected to the *needleCenterline* fields of two separate instances of the **SoNSegEvaluate** module (see Fig. 8.3). Output and input fields of the SoNSegEvaluate module are reported in Table 8. Linear interpolation of the points in world coordinates was performed. The absolute deviation angle $\theta$ from the segmented needle direction was calculated. The distance from the segmented entry point and the detected needle centerline $d$ was also computed in order to determine the shift from the visible needle position. The results are summarized in Tables 9, 10 and 11. Mean $\mu_T$ and standard deviation $\sigma_T$ over all images both for $\theta$ and $d$ were also calculated.

The runtime of both algorithms was also measured. To this purpose, 6 images were picked out randomly from each dataset. If the number of images in a dataset was smaller than the predefined value, all the images in the data set were used. In order to measure the time, the field *TimeCount* was set to TIME_COUNT in the SoNSegCropConeEngineWrld, SoNSegHoughCone and SoNSegEdgeList modules. The starting and ending timepoints of the processing for each image could therefore be registered. The difference between the timestamps provided the desired runtime. The results are summarized in Table 14. Mean $\mu_{RT}$ and standard deviation $\sigma_{RT}$ over all datasets were further calculated.

### Detection Accuracy

Table 9: Detection Accuracy for Patient Dataset 1 to 3

| | **P1** | | | | **P2** | | **P3** | |
|---|---|---|---|---|---|---|---|---|
| | **#Im: 66** | | **#Im: 2** | | **#Im: 4** | | **#Im: 2** | |
| | $\sigma_C = 0.7$ | | $\sigma_C = 0.7$ | | $\sigma_C = 1$ | | $\sigma_C = 0.8$ | |
| | $\theta(^\circ)$ | $d(mm)$ | $\theta(^\circ)$ | $d(mm)$ | $\theta(^\circ)$ | $d(mm)$ | $\theta(^\circ)$ | $d(mm)$ |
| | **Algorithm exploiting the small eigenvalue and edge linking** | | | | | | | |
| | $T_E = 0.1$ | | | | | | | |
| $\mu$ | 10.73 | 8.61 | 8.05 | 8.95 | 24.47 | 19.28 | 16.37 | 47.61 |
| $\sigma$ | 8.41 | 5.74 | 1.79 | 3.06 | 7.70 | 12.10 | 7.37 | 17.00 |
| | **Algorithm exploiting Hough transform** | | | | | | | |
| $\mu$ | 6.43 | 5.48 | 2.99 | 2.88 | 12.18 | 6.96 | 25.76 | 6.38 |
| $\sigma$ | 9.74 | 1.92 | 0 | 0 | 12.46 | 3.20 | 3.87 | 1.78 |

Table 10: Detection Accuracy for Patient Dataset 4 to 5

| | **P4** | | **P5** | | | | | |
|---|---|---|---|---|---|---|---|---|
| | **#Im: 37** | | **#Im: 21** | | **#Im: 58** | | **#Im: 8** | |
| | $\sigma_C = 1$ | | $\sigma_C = 1$ | | | | | |
| | $\theta(^\circ)$ | $d(mm)$ | $\theta(^\circ)$ | $d(mm)$ | $\theta(^\circ)$ | $d(mm)$ | $\theta(^\circ)$ | $d(mm)$ |
| | **Algorithm exploiting the small eigenvalue and edge linking $T_E$ = 0.1** | | | | | | | |
| | $T_E = 0.1$ | | $T_E = 0.0963$ | | $T_E = 0.1$ | | | |
| $\mu$ | 21.10 | 4.72 | 3.05 | 7.31 | 5.03 | 11.25 | 6.90 | 17.89 |
| $\sigma$ | 4.21 | 2.37 | 3.03 | 7.25 | 5.86 | 12.41 | 7.72 | 19.48 |
| | **Algorithm exploting Hough transform** | | | | | | | |
| $\mu$ | 2.03 | 3.60 | 1.18 | 4.27 | 2.86 | 3.26 | 1.13 | 3.98 |
| $\sigma$ | 2.15 | 1.27 | 0.95 | 2.11 | 4.01 | 0.99 | 0.87 | 0.97 |

Table 11: Detection Accuracy for Patient Dataset 6 and 8

| | **P6** | | | | **P8** | | | |
|---|---|---|---|---|---|---|---|---|
| | **#Im: 2** | | **#Im: 2** | | **#Im: 40** | | **#Im: 24** | |
| | $\sigma_C = 0.4$ | | | | $\sigma_C = 0.7$ | | | |
| | $\theta(^\circ)$ | $d(mm)$ | $\theta(^\circ)$ | $d(mm)$ | $\theta(^\circ)$ | $d(mm)$ | $\theta(^\circ)$ | $d(mm)$ |
| | **Algorithm exploting small eigen value and edge linking** | | | | | | | |
| | $T_E = 0.1$ | | | | | | | |
| $\mu$ | 4.37 | 7.44 | 9.80 | 18.27 | missing | missing | missing | missing |
| $\sigma$ | 1.46 | 0.17 | 9.88 | 21.30 | missing | missing | missing | missing |
| | **Algorithm exploting Hough transform** | | | | | | | |
| $\mu$ | 2.47 | 7.89 | 1.37 | 5.81 | 11.23 | 4.64 | 14.43 | 6.55 |
| $\sigma$ | 2.56 | 1.66 | 0.94 | 0.39 | 12.80 | 1.84 | 9.40 | 1.98 |

Table 12: Detection Accuracy for Patient Dataset 7 and 9 to 10

| | **P7** | | | | **P9** | | | | **P10** | | | |
|---|---|---|---|---|---|---|---|---|---|---|---|---|
| | **#Im: 32** | | **#Im: 37** | | **#Im: 44** | | **#Im: 22** | | **#Im: 23** | | **#Im: 28** | |
| | $\sigma_C = 0.8$ | | | | $\sigma_C = 0.8$ | | | | $\sigma_C = 0.8$ | | | |
| | $\theta(^\circ)$ | $d(mm)$ | $\theta(^\circ)$ | $d(mm)$ | $\theta(^\circ)$ | $d(mm)$ | $\theta(^\circ)$ | $d(mm)$ | $\theta(^\circ)$ | $d(mm)$ | $\theta(^\circ)$ | $d(mm)$ |
| | **Algorithm exploiting the small eigenvalue and edge linking** | | | | | | | | | | | |
| | $T_E = 0.1$ | | | | | | | | | | | |
| $\mu$ | 7.11 | 6.45 | 10.66 | 8.68 | 4.88 | 6.97 | 4.81 | 7.71 | 2.71 | 6.78 | 6.53 | 6.63 |
| $\sigma$ | 5.69 | 5.39 | 10.53 | 9.58 | 5.56 | 4.48 | 3.63 | 3.30 | 2.27 | 4.86 | 4.16 | 4.30 |
| | **Algorithm exploting Hough transform** | | | | | | | | | | | |
| $\mu$ | 2.62 | 5.52 | 4.55 | 3.40 | 1.93 | 2.94 | 4.91 | 4.67 | 2.96 | 3.88 | 1.61 | 4.67 |
| $\sigma$ | 4.06 | 2.39 | 3.98 | 1.15 | 2.46 | 1.21 | 8.08 | 0.53 | 4.04 | 1.17 | 1.30 | 1.86 |

Table 13: Detection Accuracy Over All Datasets

| | **Small Eigenvalue and Edge Linking*** | | **Hough Transform** | |
|---|---|---|---|---|
| | **#Im: 388** | | **#Im: 452** | |
| | $\theta(^\circ)$ | $d(mm)$ | $\theta(^\circ)$ | $d(mm)$ |
| $\mu_T$ | 8.37 | 8.42 | 4.79 | 4.37 |
| $\sigma_T$ | 8.16 | 8.50 | 7.63 | 1.92 |

*For the calculation of $\mu_T$ and $\sigma_T$ concerning the algorithm based on the small eigenvalue and edge linking, the dataset P8 was excluded.

## Runtime

Table 14: Running Time for Patient Dataset 1 to 10

| | P1 | P2 | P3 | P4 | P5 | P6 | P7 | P8 | P9 | P10 |
|---|---|---|---|---|---|---|---|---|---|---|
| | **Algorithm exploting small eigen value and edge linking** | | | | | | | | | |
| $\mu$ (ms) | 76.50 | 78.67 | 68.50 | 107.00 | 140.83 | 81.75 | 78.67 | 32.00 | 155.17 | 365.83 |
| $\sigma$ (ms) | 9.35 | 11.24 | 7.78 | 7.35 | 8.38 | 11.12 | 3.33 | 2.90 | 7.36 | 70.56 |
| | **Algorithm Exploiting Hough transform** | | | | | | | | | |
| $\mu$ (ms) | 40.83 | 25.67 | 51.00 | 56.00 | 57.50 | 38.00 | 37.67 | 46.67 | 64.17 | 125.67 |
| $\sigma$ (ms) | 1.33 | 1.86 | 1.41 | 6.03 | 1.52 | 4.83 | 6.98 | 4.80 | 2.23 | 7.55 |

Table 15: Running Time Over All Datasets

| | **Small eigen value and edge linking** | **Hough transform** |
|---|---|---|
| $\mu_{RT}$ (ms) | 123.56 | 55.06 |
| $\sigma_{RT}$ (ms) | 96.13 | 27.97 |

# 9 Discussion and Conclusions

In this work two algorithms for automatic needle detection were developed. The first algorithm is based on the Hough transform. For the implementation, the characteristic appearance of a couple of parallel lines in the parameter space are exploited. Informations concerning the entry and target points coming from the planning and targeting step were also integrated reducing the investigated area both in the image and in the parameter space. The second algorithm presents a more heuristic approach, funding the search of the needle contours on proximity and orientation consideration. The prior information provided by the entry and target points together with the knowledge about the low intensity levels characterizing the needle artifact appearance are employed.

The algorithm based on the Hough transform provided in general better accuracy with an average angle deviation of $4.79° \pm 7.63°$ and an average distance of $4.37mm \pm 1.92mm$ in comparison with the results provided by the algorithm exploiting the small eigenvalue and edge linking with an angle deviation of $8.37° \pm 8.16°$ and a distance of $8.42mm \pm 8.50mm$. No remarkable differences in the results were noticed as concerning the slice orientation. Examples of detection with the algorithm based on the Hough transform are shown in Fig. 9.1. Moreover, the algorithm exploiting Hough transform proved to be insensitive to slight movements of the entry point (see Fig. 9.4) which are due to the respiratory motion.

The algorithm based on the small eigenvalue and edge linking proved to be less feasible and prone to errors. Causes of errors were found in all the steps of the detection and are summarized in this section. The latter failed the determination of the needle centerline for data set $P8$. The target region is located close to the surface. As a consequence, the images resulting from the cropping process is small. In addition, the data set is very noisy. The Canny algorithm runs therefore on a small area and the determination of the thresholds for the hysteresis step result too high. Mostly in this data set, the edges of the needle are reduced to just one line and sometimes they are even not detected (see Fig. 9.2). The edge list algorithm tries to find a couple of contours: if just one edge for the needle is present, the second contour candidate could also be a fragment of the fat layer contour that lie inside the circular sector and has an orientation deviation not higher than 45° as described in Section 7.4.3. The resulting needle centerline is rather off from the needle position. If no edge for the needle is present the centerline is completely off.

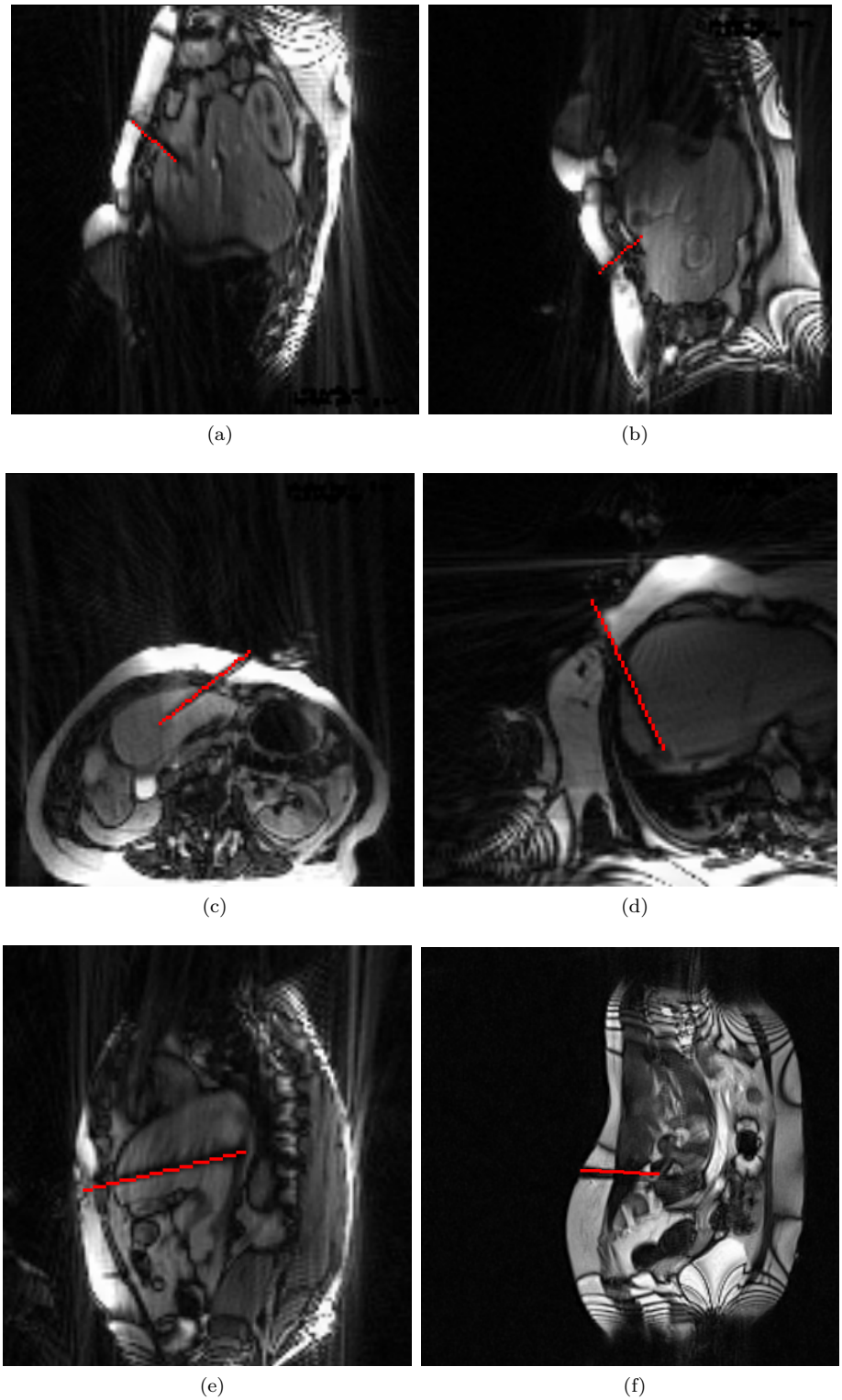

Fig. 9.1: Illustration of successful needle detections performed applying the algorithm based on the Hough transform. (a), (b), (c), (d), (e) and (f) refer respectively to $P8$ first and second groups, $P1$, $P4$, $P5$ first group, $P7$ second group.

On the contrary, the algorithm exploiting the Hough transform could detect the needle when at least fragments of the needle contours were present. The results suggest the robustness of the algorithm. However, when no needle contour survive, the maximum detected in the accumulator array belong to a lines other than the needle edges. This situation refers to 7 out of the 40 images of the first group and 5 out of 24 of the second group. Better results could be achieved trying to reduce the noise in the image and increasing the dimension of the cropped region when the length of the planned trajectory would induce a too small area after the cropping.

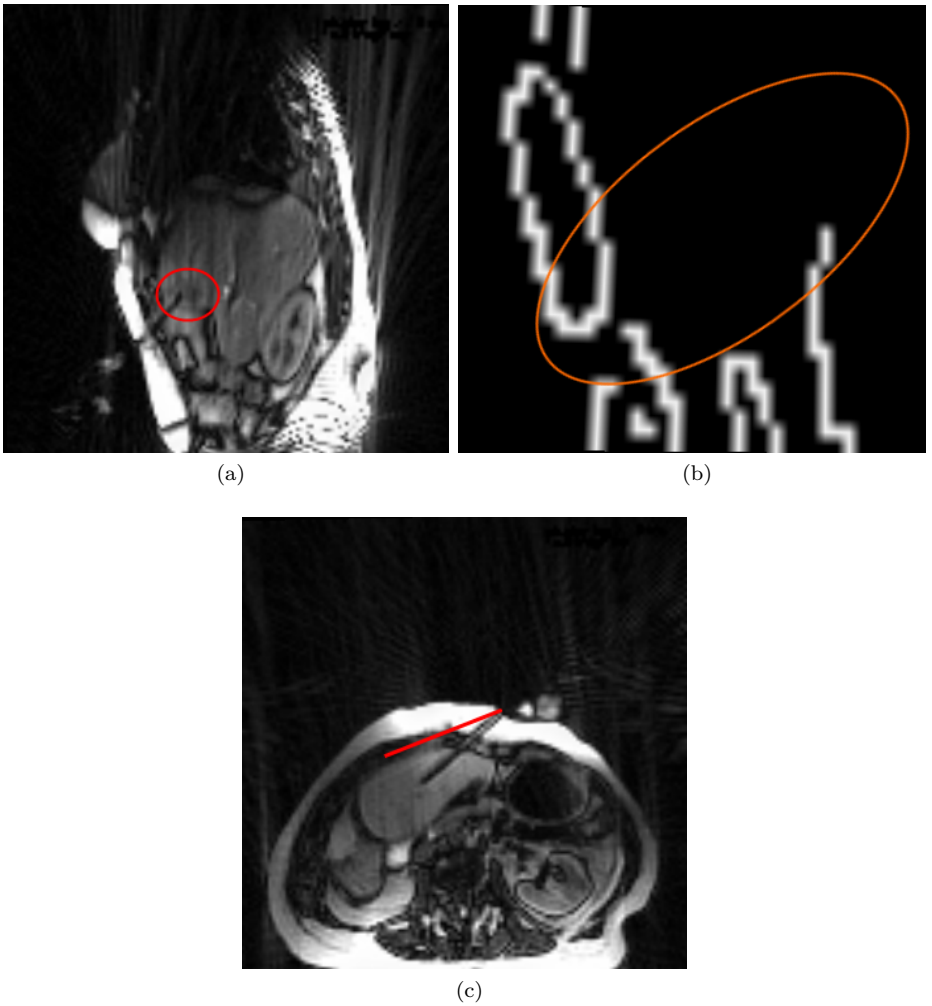

(a) (b)

(c)

Fig. 9.2: An Image of data set $P8$ is shown. The red ellipse highlights the target region. The corresponding edge image resulting from the Canny algorithm is shown in (b). The orange ellipse mark the area where the needle is located in the cropped image. No edges for the needle are detected. (c) Wrong determination of the darkest path used as reference direction for orientation comparison in data set $P1$.

The survival of just some fragments of the needle contours after the processing with the small eigenvalue filter, in addition to the discretization effect, is responsible for other minor deviations.

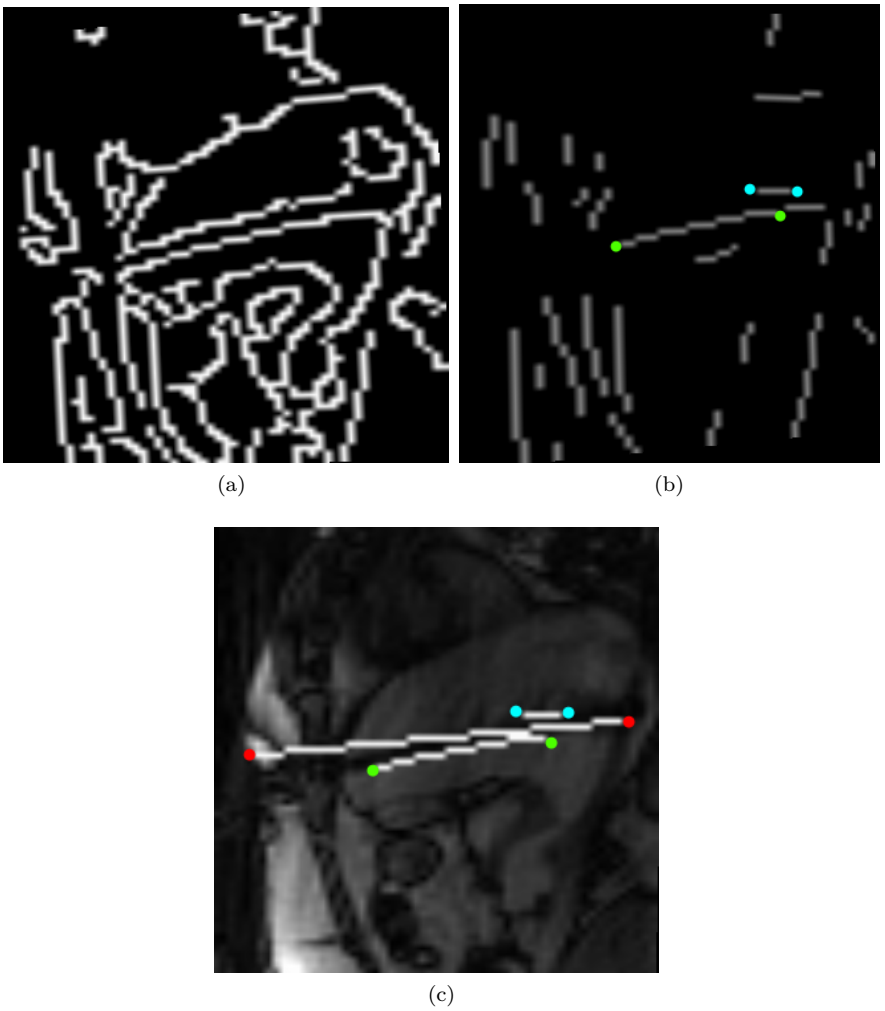

Fig. 9.3: (a) Result of the Canny algorithm. (b) Result after the application of the small eigenvalue filtering. (c) Angle deviation due to the survival of just some fragments after the application of the small eigenvalue filtering is depicted. Dots of the same colors mark the extreme point of the edges identified as the couple of needle contours. The red dots refer to the needle centerline.

In Fig. 9.3b the contours resulting after the filtering and identified as needle contours candidate are shown. The needle contours are identified correctly, but one is represented just from the horizontal segment survived after the small eigenvalue thresholding. No other fragments of the upper needle contour was available to the edge linking step. The segment is responsible for the deviation from the real needle direction (see Fig. 9.3c).

Despite the high threshold set for the small eigenvalue filter ($T_E = 0.1$), slice orientation and therefore the needle orientation with respect to the axes of the image influence the outcome of the needle detection. A noisy needle contour parallel to one of the image axes demonstrated a higher survival rate to the small eigenvalue thresholding, than a noisy contour with a different orientation. Moreover, even when both the needle contours were available for the edge linking step, a spurious edge closer than one the contour to the darkest path, could be identified as needle contour candidate, causing a high angle deviation.

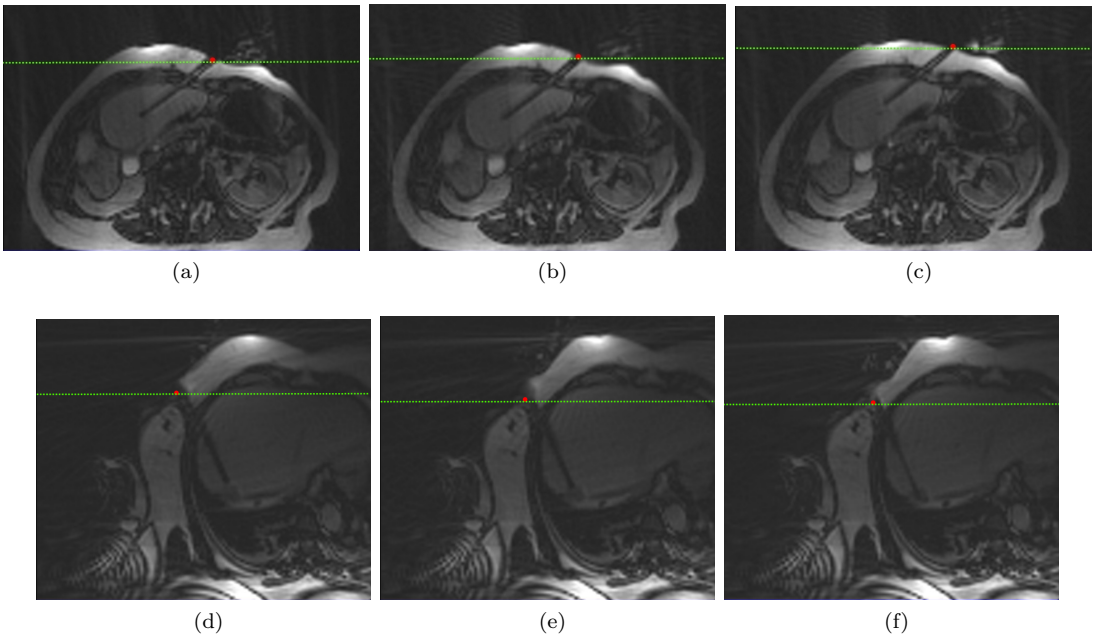


Fig. 9.4: Examples of the entry point movement due to the respiratory motion are illustrated. (a), (b) and (c) refer to the first group of the $P4$ data set. (d), (e) and (f) refer to the first group of the $P8$ data set.

In the data set $P1$, $P2$ and $P3$ the main cause of a wrong needle centerline detection through the algorithm based on edge linking is the incorrect determination of the darkest path direction at the very beginning of the edge linking step. As shown in Fig. 9.3, when the needle is located very close to a second broad dark structure with comparable intensities, the direction along which the sum of squares of the intensity levels is the lowest results inside the adjacent structure. At least one of the contours of the structure are in this situation identified as the candidate needle contours. This wrong identification happens in 14 images out of 66 for the first group of $P1$ and in all the 4 images in $P2$.

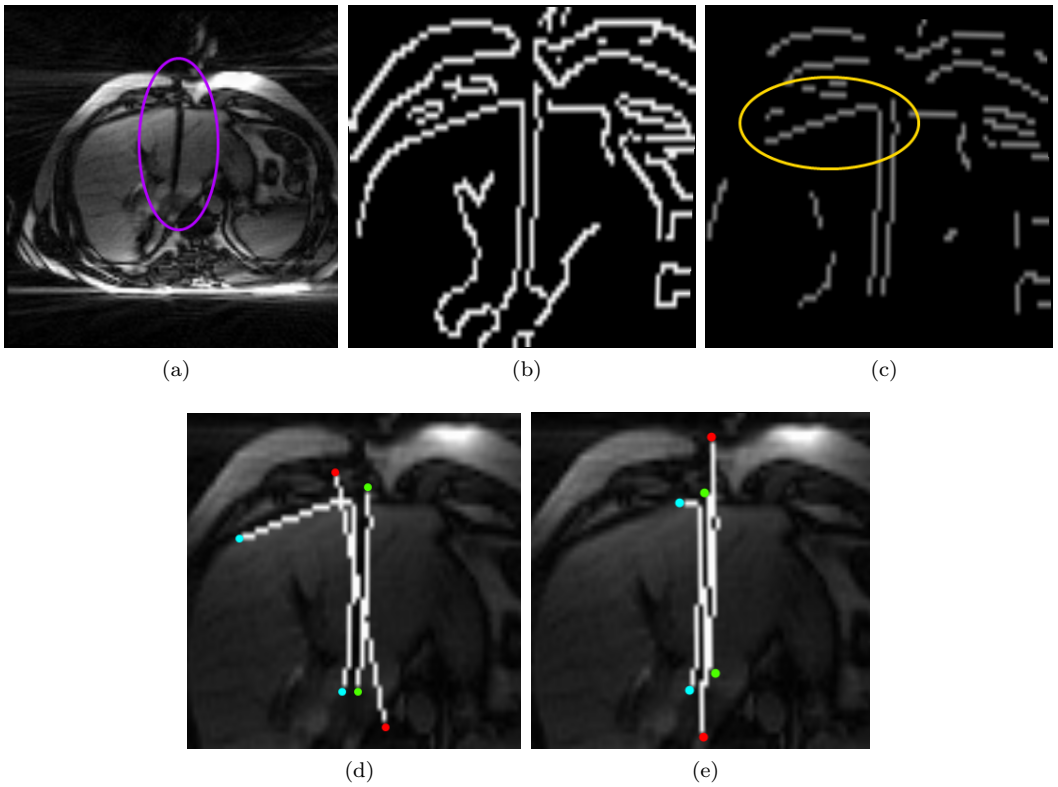

Fig. 9.5: Some steps of the needle centerline detection exploiting edge linking are illustrated. The original image is shown on the top and the needle is highlighted by the purple ellipse. (b) The result of the Canny algorithm applied to one of the images available is depicted. The outcome of the small eigenvalue filter (T = 0.1) performed on the edge image is shown in (c). The yellow ellipse highlights the residual connection existing between one of the needle contour and the survival fat contour. In (d) and (e) the results of needle detection without pixels removal and with pixels removal are shown. The blue and green spots mark the extreme points of the contours. The red spots mark the detected needle centerline.

The segment truncation described in Section 7.4.3 demonstrated to improve the accuracy of the detection. In Fig. 9.5d and Fig. 9.5e, the results of needle detection respectively without recurring to pixel points removal and with pixel points removal is reported.

Device positioning during a percutaneous minimally invasive procedure could benefit from automatic needle detection. Computation of the angle deviation of the detected needle centerline from the planned path and calculation of the distance of the entry point from the the centerline could allow real-time update of the scan planes along the needle direction. Feedback about the offset from the planned trajectory could also be provided to the physician. Both automatic slice realignment and offset indication are expected to improve the speed and the accuracy of the device insertion. Correct needle positioning would contribute to improve the effectiveness of the procedure.

The accuracy obtained with the algorithm based on the Hough transform proved to be comparable with the spatial resolution of the images (see Tables 5 and 6). The mean angle deviation of the individual datasets resulted more stable in the

cryoablation dataset, with values always smaller than 5°. 3 out of 7 radiofrequency ablation datasets showed instead values greater than 10°. Similar observations can be made as concerning the distance $d$. Values of standard deviation greater than 9° for the angle deviation could be found in the radio frequency dataset. No appreciable difference between the standard deviations concerning the distance $d$ in the two datasets was noticed.

The algorithm exploiting the small eigenvalue and edge linking showed in general a worse performance. Also in the cryoablation dataset, the angle deviation remained in general above 6° with a standard deviation oscillating between 3° and 10°. Worth remembering is also the failure of the algorithm in detecting the needle centerline in dataset P8.

The algorithm based on the Hough transform showed better performance also concerning the measured runtime with a mean value of $55.06ms \pm 27.97ms$ compared to the runtime value $123.56ms \pm 96.13ms$ achieved with the algorithm based on the small eigenvalue and edge linking.

The higher mean accuracy and smaller standard deviation obtained for the cyoablation daset suggest that better performance could be in general achieved exploiting the same acquisition parameters used for this dataset.

Further improvements are required before the algorithm based on the small eigenvalue and edge linking could be exploited for procedure guidance. More focus could be put in trying to integrate information about the intesity that could be expected for the needle artifact. Acquisition of a reference image along the planned trajectory and comparison with the successive dynamic images acquired, for example by image subtraction, could improve the result of the detection. Update of the reference image should be guaranteed before the realignment of the scan plane is performed.

The good accuracy and the stability achieved with the algorithm based on the Hough transform showed promising results. Although algorithm optimization is still required in order to allow faster processing, the method presented feasible needle artifact detection. Accurate translation and orientation feedback are expected to be provided and to contribute to a more precised device positioning.

# List of Figures

# List of Tables

# Nomenclature

$BW$ Band Width

$FID$ Free Induction Decay

$FSE$ Fast Spin Echo

$I$ Spin Angular Momentum

$M_t$ Transverse Magnetization Vector

$MR$ Magnetic Resonance

$MRI$ Magnetic Resonance Imaging

$NMR$ Nuclear Magnetic Resonance

$NMV$ Net Magnetization Vector

$TE$ Time to Echo

BEAT_IRTTT BEAT Interactive Real Time Tip Tracking

BMI Body Mass Index

DICOM Digital Imaging and COmmunications in Medicine

FOV Field of View

FT Fourier Transform

GRE Gradient Echo Sequence

IFE Interactive Front End

LUT Look Up Table

MPR Multi Planar Reconstructed

RF Radio Frequency

RFA Radiofrequency Ablation

SNR Signal to Noise Ratio

TR Repetition Time

XIP eXtensible Imaging Platform

# References

[AMB+86] A.M. Aisen, W. Martel, E.M. Braunstein, K.I. McMillin, W.A. Phillips, and TF Kling, *MRI and CT evaluation of primary bone and soft-tissue tumors*, American Journal of Roentgenology **146** (1986), no. 4, 749.

[Bed02] C.W.M. Bedrossian, *Clinical cytopathology and aspiration biopsy*, Diagnostic Cytopathology **26** (2002), no. 1, 67.

[BH+05] D.W. Bratzler, P.M. Houck, et al., *Antimicrobial prophylaxis for surgery: an advisory statement from the National Surgical Infection Prevention Project*, The American Journal of Surgery **189** (2005), no. 4, 395–404.

[BPD+99] K. Butts, J.M. Pauly, B.L. Daniel, S. Kee, and A.M. Norbash, *Management of biopsy needle artifacts: techniques for RF-refocused MRI*, Journal of Magnetic Resonance Imaging **9** (1999), no. 4, 586–595.

[BS03] M.A. Brown and R.C. Semelka, *MRI: basic principles and applications*, John Wiley & Sons, 2003.

[CAC+97] L.H. Cohn, D.H. Adams, G.S. Couper, D.P. Bichell, D.M. Rosborough, S.P. Sears, and S.F. Aranki, *Minimally invasive cardiac valve surgery improves patient satisfaction while reducing costs of cardiac valve replacement and repair*, Annals of surgery **226** (1997), no. 4, 421.

[Can87] J. Canny, *Computational approach to edge detection*, Readings in computer vision: issues, problems, principles, and paradigms **184** (1987), 679–698.

[CHT+99] S.A. Chen, M.H. Hsieh, C.T. Tai, C.F. Tsai, VS Prakash, W.C. Yu, T.L. Hsu, Y.A. Ding, and M.S. Chang, *Initiation of atrial fibrillation by ectopic beats originating from the pulmonary veins: electrophysiological characteristics, pharmacological responses, and effects of radiofrequency ablation*, Circulation **100** (1999), no. 18, 1879.

[CMD+87] A.E. Chang, Y.L. Matory, A.J. Dwyer, S.C. Hill, M.E. Girton, S.M. Steinberg, R.H. Knop, J.A. Frank, D. Hyams, J.L. Doppman, et al., *Magnetic resonance imaging versus computed tomography in the evaluation of soft tissue tumors of the extremities*, Annals of surgery **205** (1987), no. 4, 340.

[CSB+01] J.C. Carr, O. Simonetti, J. Bundy, D. Li, S. Pereles, and J.P. Finn, *Cine MR Angiography of the Heart with Segmented True Fast Imaging with Steady-State Precession*, Radiology **219** (2001), no. 3, 828.

[Cur01] S.A. Curley, *Radiofrequency ablation of malignant liver tumors*, The Oncologist **6** (2001), no. 1, 14.

[DF03] M. Ding and A. Fenster, *A real-time biopsy needle segmentation technique using Hough Transform*, Medical Physics **30** (2003), 2222.

[DH72] R.O. Duda and P.E. Hart, *Use of the Hough transformation to detect lines and curves in pictures*, Communications of the ACM **15** (1972), no. 1, 11–15.

[Dis] *Discussion with Eva Rothgang.*

[DSJ09] A.M. Davies, M. Sundaram, and SLJ James, *Imaging of bone tumors and tumor-like lesions: Techniques and applications*, Springer Verlag, 2009.

[DZA+00] D.E. Dupuy, R.J. Zagoria, W. Akerley, W.W. Mayo-Smith, P.V. Kavanagh, and H. Safran, *Percutaneous radiofrequency ablation of malignancies in the lung*, American Journal of Roentgenology **174** (2000), no. 1, 57.

[(ED07] Siemens Corporate Research Inc. 13 August 2008 (EDT), *Overlay graphics tutorial*, https://collab01a.scr.siemens.com/xipwiki/, November 2007.

[EDS+11] Rothgang E., Gilson W. D., Valdeig S., Roland J. Pan L., Flammang H., Lorenz C.H., Wacker F., and Frericks B., *Enhanced Intra-Operative Control During Cryoablation by Using the PRF Method: In Vivo Imaging and Histopathologic Correlation*, to be published in Proceedings of International Society for Magnetic Resonance in Medicine (ISMRM) (Joint Annual Meeting ISMRM - ESMRMB Montreal, Canada 7.-13. May 2011). (2011).

[FMBM07] O. Felfoul, J.B. Mathieu, G. Beaudoin, and S. Martel, *In Vivo MR-Tracking Based on Magnetic Signature Selective Excitation*, Medical Imaging, IEEE Transactions on **27** (2007), no. 1, 28–35.

[GCC+04] M.P. Goetz, M.R. Callstrom, J.W. Charboneau, M.A. Farrell, T.P. Maus, T.J. Welch, G.Y. Wong, J.A. Sloan, P.J. Novotny, I.A. Petersen, et al., *Percutaneous image-guided radiofrequency ablation of painful metastases involving bone: a multicenter study*, Journal of Clinical Oncology **22** (2004), no. 2, 300.

[GCC+05] E.W. Gregg, Y.J. Cheng, B.L. Cadwell, G. Imperatore, D.E. Williams, K.M. Flegal, KM Narayan, and D.F. Williamson, *Secular trends in cardiovascular disease risk factors according to body mass index in us adults*, Jama **293** (2005), no. 15, 1868.

[GGSL00] G.S. Gazelle, S.N. Goldberg, L. Solbiati, and T. Livraghi, *Tumor*

*ablation with radio-frequency energy*, Radiology **217** (2000), no. 3, 633.

[GH11] Johns Hopkins Gastroenterology and Hepatology, *Johns hopkins gastroenterology and hepatology*, http://www.hopkins-gi.org/, February 2011.

[GPS+97] S.C. Goehde, T. Pfammatter, P. Steiner, P. Erhart, B.J. Romanowski, and J.F. Debatin, *MR-guided cholecystostomy: Assessment of biplanar, real-time needle tracking in three pigs*, Cardiovascular and interventional radiology **20** (1997), no. 4, 295–299.

[GSN04] DS Guru, BH Shekar, and P. Nagabhushan, *A simple and robust line detection algorithm based on small eigenvalue analysis*, Pattern Recognition Letters **25** (2004), no. 1, 1–13.

[Haa04] E.M. Haacke, *Susceptibility weighted imaging*, Magnetic Resonance in Medicine **52** (2004), 612–618.

[HB02] N.E. Hoffmann and J.C. Bischof, *The cryobiology of cryosurgical injury*, Urology **60** (2002), no. 2, 40–49.

[HBL04] R.H. Hashemi, W.G. Bradley, and C.J. Lisanti, *MRI: the basics*, Lippincott Williams & Wilkins, 2004.

[Hoa09] Denis Hoa, *Magnetic susceptibility and metal*, http://www.imaios.com/en/e-Courses/e-MRI/Image-quality-and-artifacts/magnetic-susceptibility, 2009.

[HWTM90] E.M. Haacke, P.A. Wielopolski, J.A. Tkach, and MT Modic, *Steady-state free precession imaging in the presence of motion: application for improved visualization of the cerebrospinal fluid*, Radiology **175** (1990), no. 2, 545.

[ICW+95] Y. Ishihara, A. Calderon, H. Watanabe, K. Okamoto, Y. Suzuki, K. Kuroda, and Y. Suzuki, *A precise and fast temperature mapping using water proton chemical shift*, Magnetic Resonance in Medicine **34** (1995), no. 6, 814–823.

[JKYK06] H.G. Jung, D.S. Kim, P.J. Yoon, and J. Kim, *Parking slot markings recognition for automatic parking assist system*, Intelligent Vehicles Symposium, 2006 IEEE, IEEE, 2006, pp. 106–113.

[KGA04] E. Kochavi, D. Goldsher, and H. Azhari, *Method for rapid MRI needle tracking*, Magnetic Resonance in medicine **51** (2004), no. 5, 1083–1087.

[KI86] J. Kittler and J. Illingworth, *Minimum error thresholding*, Pattern recognition **19** (1986), no. 1, 41–47.

[KSG98] V. Kamat-Sadekar and S. Ganesan, *Complete description of multiple line segments using the Hough transform*, Image and Vision Computing **16** (1998), no. 9-10, 597–613.

[LBDL89] D. Le Bihan, J. Delannoy, and R.L. Levin, *Temperature mapping with MR imaging of molecular diffusion: application to hyperthermia*, Radiology **171** (1989), no. 3, 853.

[LDJ+96] JS Lewin, JL Duerk, VR Jain, CA Petersilge, CP Chao, and JR Haaga, *Needle localization in MR-guided biopsy and aspiration: effects of field strength, sequence design, and magnetic field orientation*, American Journal of Roentgenology **166** (1996), no. 6, 1337.

[LED+96] M.E. Ladd, P. Erhart, J.F. Debatin, B.J. Romanowski, P. Boesiger, and G.C. McKinnon, *Biopsy needle susceptibility artifacts*, Magnetic Resonance in Medicine **36** (1996), no. 4, 646–651.

[Lip08] M.L. Lipton, *Totally accessible MRI: a user's guide to principles, technology, and applications*, Springer Verlag, 2008.

[LKZ+05] C.H. Lorenz, K.J. Kirchberg, S. Zuehlsdorff, P. Speier, M. Caylus, W. Borys, and MA Guttman, *Interactive Frontend (IFE): a platform for graphical MR scanner control and scan automation*, Proc Intl Soc Mag Reson Med, vol. 13, 2005, p. 2170.

[LL93] C.H. Li and CK Lee, *Minimum cross entropy thresholding*, Pattern Recognition **26** (1993), no. 4, 617–625.

[MB00] C.T.W. Moonen and P.A. Bandettini, *Functional MRI*, Springer Verlag, 2000.

[MBGL+04] B. Mueller-Bierl, H. Graf, U. Lauer, G. Steidle, and F. Schick, *Numerical modeling of needle tip artifacts in MR gradient echo imaging*, Medical Physics **31** (2004), 579.

[McL97] C.H. McLeskey, *Geriatric anesthesiology*, Lippincott Williams and Wilkins, 1997.

[Med10] Cook Medical, *MRI Compatibility*, http://www.cookmedical.com/mri.do, 2010.

[MMG03] D.W. McRobbie, E.A. Moore, and M.J. Graves, *MRI from Picture to Proton*, Cambridge Univ Pr, 2003.

[MMTZ08] M.A. Mauro, K. Murphy, K. Thomson, and C.L. Zollikofer, *Image-guided interventions*, Saunders, 2008.

[MNV05] P. Mazzoldi, M. Nigro, and C. Voci, *Elementi di fisica-elettromagnetismo*, 2005.

[Ots75] N. Otsu, *A threshold selection method from gray-level histograms*, Automatica **11** (1975), 285–296.

[Pre70] J.M.S. Prewitt, *Object enhancement and extraction*, Picture processing and Psychopictorics (1970), 75–149.

[PRO+00] C. Pappone, S. Rosanio, G. Oreto, M. Tocchi, F. Gugliotta, G. Vicedomini, A. Salvati, C. Dicandia, P. Mazzone, V. Santinelli, et al., *Circumferential radiofrequency ablation of pulmonary vein ostia: a new anatomic approach for curing atrial fibrillation*, Circulation **102** (2000), no. 21, 2619.

[Pro11] The Open XIP Project, *Ultrasound - technology information portal*, http://www.us-tip.com/, 2011.

[RCB+09] H. Rempp, S. Clasen, A. Boss, J. Roland, A. Kickhefel, C. Schraml, C.D. Claussen, F. Schick, and P.L. Pereira, *Prediction of cell necrosis with sequential temperature mapping after radiofrequency ablation*, Journal of Magnetic Resonance Imaging **30** (2009), no. 3, 631–639.

[RDW+11] E. Rothgang, Gilson W. D., Strehl W., Pan L., Roland J., Lorenz C. H., and Hornegger J., *Interventional MR -Imaging for Thermal Ablation Therapy*, IEEE International Symposium on Biomedical Imaging (ISBI)(Chicago (IL), USA 30. March - 2. April 2011 (2011), 762522.

[RELC10] Hornegger J. Rothgang E., Gilson W. D., Lorenz, and Lorenz C.H., *A system for advanced real-time visualization and monitoring of mr-guided thermal ablations*, Medical Imaging 2010: Visualization, Image-Guided Procedures, and Modeling (SPIE Medical Imaging San Diego (CA), USA 13.-18. 02.2010) (2010), no. 3, 762522.

[RFB+08] T.K. Rosengart, T. Feldman, M.A. Borger, T.A. Vassiliades Jr, A.M. Gillinov, K.J. Hoercher, A. Vahanian, R.O. Bonow, and W. O'Neill, *Percutaneous and minimally invasive valve procedures: A scientific statement from the american heart association council on cardiovascular surgery and anesthesia, council on clinical cardiology, functional genomics and translational biology interdisciplinary working group, and quality of care and outcomes research interdisciplinary working group*, Circulation **117** (2008), no. 13, 1750.

[Rob63] L.G. Roberts, *Machine perception of three-dimensional solids*, Tech. report, MASSACHUSETTS INST OF TECH LEXINGTON LINCOLN LAB, 1963.

[RP06] P. Reimer and P.M. Parizel, *Clinical MR imaging: a practical approach*, Springer Verlag, 2006.

[SF68] I. Sobel and G. Feldman, *A 3x3 isotropic gradient operator for image processing*, Presentation for Stanford Artificial Project (1968).

[SKD+03] R.C. Susil, A. Krieger, J.A. Derbyshire, A. Tanacs, L.L. Whitcomb, G. Fichtinger, and E. Atalar, *System for MR Image–guided Prostate Interventions: Canine Study1*, Radiology **228** (2003), no. 3, 886.

[SMO+98] K. Shimizu, R.V. Mulkern, K. Oshio, L.P. Panych, S.S. Yoo, F.A. Jolesz, and R. Kikinis, *Rapid tip tracking with MRI by a limited projection reconstruction technique*, Journal of Magnetic Resonance Imaging **8** (1998), no. 1, 262–264.

[Sof11] SoftWays, *Magnetic resonance - technology information portal*, http://www.mr-tip.com/, 2011.

[Son05] Allen W. Song, *Principles of MRI: Image Formation. Brain Imaging and Analysis Center. Duke University*, http://www.biac.duke.edu/education/courses/fall05/fmri/handouts/2005 Week3ImageFormation.ppt, 2005.

[SS05] A. Saxena and B. Sahay, *Computer aided engineering design*, Kluwer Academic Pub, 2005.

[VCBC88] S. Vasudevan, R.L. Cannon, J.C. Bezdek, and W.L. Cameron, *Heuristics for intermediate level road finding algorithms*, Computer vision, graphics, and image processing **44** (1988), no. 2, 175–190.

[ZMG+06] H. Zimmermann, S. Mueller, B. Gutmann, H. Bardenheuer, A. Melzer, R. Umathum, W. Nitz, W. Semmler, and M. Bock, *Targeted-HASTE imaging with automated device tracking for MR-guided needle interventions in closed-bore MR systems*, Magnetic resonance in medicine **56** (2006), no. 3, 481–488.

# Acknowledgements

I would really like to thank Eva Rothgang for the possibility to explore the amazing field of interventional MRI. Her supervision and help were of great importance for me. I was completely fascinated from the long sessions at the scanner, during which I could learn so much also thanks to her patience in answering the flood of questions I had.

Many thanks to Prof. Joachim Hornegger for hosting me at the Pattern Recognition Lab during my master thesis and to Prof. Alfredo Ruggeri for supporting me in writing my thesis at the Lab.

My greatest thanks go to my family that supports me in every moment, no matter what. I could never be grateful enough for the unconditional love that my parents gave me during all my life and for the joy to have such a smart, funny and patient brother.

Many thanks also to all the precious friends I had the possibility to meet in Erlangen during these months.